

**SAND2002-8616**

**Nanoindentation Methods in Interfacial Fracture Testing**

A. A. Volinsky  
Motorola Corporation, Mesa, AZ 85202  
alex.volinsky@motorola.com

D. F. Bahr  
Washington State University, Pullman, WA 99164  
bahr@mme.wsu.edu

M. D. Kriese,  
Osmic, Auburn Hills, MI 48326  
michael.kriese@osmic.com

N. R. Moody  
Sandia National Laboratories, Livermore, CA 94550  
nrmoody@sandia.gov

W. W. Gerberich  
University of Minnesota, Minneapolis, MN 55455  
wgerb@umn.edu

This manuscript is prepared as a chapter in  
Volume 8: Interfacial and Nanoscale Failure  
(W. W. Gerberich and W. Yang, editors)  
Comprehensive Structural Integrity  
(I. Milne, R. O. Ritchie, B. Karim, Editors-in-Chief)  
Due for publication early 2003  
<http://www.elsevier.com/locate/cosi>

## Nanoindentation Methods in Interfacial Fracture Testing

8.13.1 INTRODUCTION	2
8.13.2 ADHESION	4
8.13.2.1 <i>Thermodynamic Work of Adhesion</i>	5
8.13.2.1 <i>Practical Work of Adhesion</i>	6
8.13.3 INTERFACIAL FRACTURE TEST TECHNIQUES	8
8.13.3.1 <i>Sandwich specimen tests</i>	8
8.13.3.2 <i>Bulge and blister tests</i>	10
8.13.3.3 <i>Superlayer test</i>	12
8.13.3.4 <i>Indentation tests</i>	14
8.13.3.5 <i>Superlayer indentation test</i>	17
8.13.3.6 <i>Scratch tests</i>	18
8.13.4 NANOINDENTATION-MECHANICAL PROPERTIES	20
8.13.4.1 <i>Elastic Properties</i>	20
8.13.4.1.1 <i>Load-vs-displacement curves</i>	20
8.13.4.1.2 <i>Continuous stiffness</i>	21
8.13.4.1.3 <i>Thin film-substrate effects</i>	22
8.13.4.2 <i>Plastic Properties</i>	22
8.13.4.2.1 <i>Yield strength</i>	23
8.13.4.2.2 <i>Bulk materials</i>	24
8.13.4.2.3 <i>Indentation size effects</i>	25
8.13.4.2.4 <i>Thin films</i>	27
8.13.5 THIN FILM FRACTURE	28
8.13.5.1 <i>Ceramic and Refractory Metal Films</i>	28
8.13.5.1.1 <i>Tantalum nitride</i>	28
8.13.5.1.2 <i>Silicon nitride</i>	30
8.13.5.1.2 <i>Tungsten</i>	31
8.13.5.2 <i>Ductile Metal Films</i>	32
8.13.5.2.1 <i>Copper films</i>	32
8.13.5.2.1.1 <i>Annealing effects</i>	33
8.13.5.2.1.2 <i>Interlayer effects</i>	34
8.13.5.2.1.3 <i>Film thickness effects</i>	34
8.13.5.2.1.4 <i>Temperature effects</i>	35
8.13.5.2.2 <i>Gold films</i>	35
8.13.5.2.2.1 <i>Gold-chromium bilayer films</i>	36
8.13.5.2.2.2 <i>Gold-copper bilayer films</i>	38
8.13.5.2.3 <i>Aluminum films</i>	38
8.13.6 SUMMARY	39
ACKNOWLEDGMENTS	41
REFERENCES	41
TABLES	54
NOMENCLATURE	56
LIST OF FIGURES	58
FIGURES	62

### 8.13.1 INTRODUCTION

Thin films are used in many applications where properties such as resistance to abrasion, corrosion, permeation and oxidation, or special magnetic and dielectric properties, are needed to meet specialized functional requirements (Mittal, 1976). They are becoming very important in optimizing performance of small volume systems inherent in micro and nanoelectromechanical systems (MEMS and NEMS) (Volinsky et al., 2002; Maboudian and Howe, 1997). They have also seen a dramatic increase in use with the emergence of copper as the next generation interconnect metallization material for ultra-large-scale integration (USLI) fabrication for semiconductor applications (Kriese et al., 1998a). In all of these applications, performance, reliability, and durability are tied directly to interface structure and composition (Mittal, 1976; Evans and Ruhle, 1990; Trumble and Ruhle, 1990).

These interfaces are created by deposition of dissimilar materials. This dissimilar nature creates significant challenges concerning thermomechanical integrity and reliability especially when one of the constituents is brittle (Evans and Hutchinson, 1995). The challenges arise from changes in differences in residual stress, structure, and composition. Mismatch in thermal coefficients and high energy deposition can create films with high residual stress levels capable of driving fracture along well-bonded film interfaces. Differences in structure and composition can markedly alter interface adhesion and strength. In brittle films, friction along contacting crack faces can increase performance while in ductile films, plastic deformation can markedly increase fracture energy (Evans and Hutchinson, 1995; Evans, et al., 1999). Fracture processes can also have a strong effect on device performance. In brittle film systems, debonding can occur by rupture of bonds along the interface plane at relatively low fracture energies (Evans and Hutchinson, 1995; Cannon et al., 1991). When brittle interphases or reaction products form, fracture can occur also within these phases and products at relatively low fracture energies. In contrast, hole nucleation, growth, and coalescence can markedly increase fracture energies in ductile film systems (Evans and Hutchinson, 1995; Evans and Dalgliesh, 1992.)

Qualitative tests such as the scotch tape test or the pull-off test are often used to monitor adhesion, since they are quick and easy to perform (Steinmann, 1989; Ohring, 1992). While still useful for routine quality control, these tests do not measure the interface fracture toughness, since the strain energy release rate usually cannot be deconvoluted from the work of the external load (Evans and Hutchinson, 1995; Hutchinson and Suo, 1992; Wei and Hutchinson, 1997). Difficulties are further complicated by the variety of film systems (metal-metal, metal-ceramic, polymer-metal, polymer-ceramic, etc.) found in even a single industry such as microelectronics. Thus a number of researchers have utilized linear elastic fracture mechanics to develop test and analysis methods that are truly quantitative, allowing direct assessment of the critical energies of interfacial adhesion (Cao and Evans, 1989; Charalambides et al., 1989; Suo and Hutchinson, 1989, 1990; Hutchinson and Suo, 1992; Rice, 1988; Evans et al., 1988; Evans et al., 1990).

When interfaces can be made by bonding procedures at relatively high homologous temperatures (such as diffusion bonding or brazing), many different configurations are available for testing, based on those developed for homogeneous

systems (Evans and Dalgleish, 1992; He et al., 1995; Turner et al., 1995). Studies have shown that the physics and mechanics of bimaterial interface adhesion are comparable to that for cohesion in homogeneous, isotropic solids (Rice, 1988; Evans and Dalgleish, 1992 or 1993; He et al., 1995; Hutchinson and Suo, 1992; Jensen and Thouless, 1993; Wei and Hutchinson, 1997). This enables established results to be applied to interfaces (Tvergaard and Hutchinson, 1992; Evans et al., 1999; Suo et al., 1993). As a result, the values defining fracture energy can be directly related to energy-dissipative mechanisms both at the interface and within near-interface regions of the film and substrate. However, bonding processes at relatively high temperatures often create films with structures and properties vastly different than those created by evaporation or sputter deposition at relatively low homologous temperatures.

In recent years, a number of thin-film adhesion assessment methods have been developed to measure fracture properties in the as-processed condition. While many require difficult sample preparation methods, as exemplified by the blister (Allen and Senturia, 1988, 1989; Jensen, 1991; Jensen and Thouless, 1993; Jensen et al., 1990) and edge-delamination tests (Wan and Mai, 1995; Akisanya and Fleck, 1994), some methods such those using micromechanical probes require limited, if any, preparation to induce and quantify interfacial failure (Marshall and Evans, 1984; Hutchinson and Suo, 1992). Microprobe techniques commonly utilize indentation or scratching with a diamond indenter, in conjunction with apparatus that continuously measure forces and displacements (Wu, 1991; Venkataraman et al., 1993; deBoer and Gerberich, 1996a,b, Kriesse et al., 1998b; Moody et al., 1998). In these methods, the indenter both initiates and propagates a delamination. Analysis of the load-displacement curves and fractographic measurement of the delaminations yield the parameters for use in models giving fracture energy. Indentation methods are generally preferred because delamination is typically more stable with a regular geometry indenter, allowing more rigorous mechanics of the strain energies which drive interfacial failure (Marshall and Evans, 1984; Chiang et al., 1981; Rosenfeld et al., 1990; Bahr and Gerberich, 1996a; Bahr et al., 1997; Moody et al., 1998). However, such tests are often impractical for ductile or strongly adhering films, due to the difficulty of initiating a delamination. Ductile and strongly adhering films tend to simply deform plastically prior to the development of sufficient elastic strain energy for delamination (Turner and Evans, 1996; Kriesse et al., 1998a). In order to reduce this limitation, previous researchers have used superlayers deposited over the film of interest (Bagchi et al., 1994; Bagchi and Evans, 1996). The superlayer, typically a refractory metal vapor-deposited at a low temperature that does not significantly alter the underlying film, is often deposited with a high residual stress which provides additional driving force for delamination. The combination of indentation and highly stressed superlayers provides a test approach that has been used successfully to study interfacial fracture in well-adhered ceramic films and highly deformable ductile metal films.

In this chapter, we review nanoindentation methods used to study interfacial fracture and determine interfacial fracture energies of technologically significant thin films. The focus is on as-deposited ceramic and metallic film systems, emphasizing ductile metal films used throughout the microelectronics community. It complements reviews by Nix (1989) on thin film properties, Doerner and Nix (1988) on development of residual stresses in thin films, Evans, Hutchinson and Wei (1999) on the role of plasticity and segregation on film adhesion, and the works of Evans and Hutchinson

(1995) and Hutchinson and Evans (2000) on mechanisms of damage and fracture processes in thin films and multilayers. The models employed were originally developed and discussed in detail in the works by Marshall and Evans (1984), Evans and Hutchinson (1984), and Hutchinson and Suo (1992).

The review begins with a brief discussion of the true and practical works of adhesion. This is followed by a brief discussion of linear elastic fracture mechanics techniques used to measure interfacial fracture energies and an in-depth presentation of nanoindentation and stressed overlayer (superlayer) test techniques. The techniques employed to measure thin film mechanical properties are presented as these properties are required for model inputs. They also form the basis for comparing results. The major portion of the chapter is then devoted to presentation and discussion of how these test techniques have been used to experimentally characterize thin film fracture for a number of technologically relevant applications and their results. Although the emphasis is predominantly on as-deposited films, data from thermally treated and diffusion bonded samples are included for comparison.

### 8.13.2 Adhesion

Adhesion can be quantitatively understood in terms of two energy terms, the thermodynamic work of adhesion between the materials of an interface, and the inelastic contributions occurring at and near the interface during the separation process (Evans et al., 1990; Evans and Dalgleish, 1992,1993; Hong et al., 1995; Hutchinson and Suo, 1992). The thermodynamic work of adhesion is a function of the surface energies of the materials and the interface, the nonequilibrium state of the interface, and the concentration of impurity segregants at or near the interface. The inelastic contributions include such terms as ligament bridging, plasticity within a process zone near the delamination boundary, and frictional dissipation of nonplanar surfaces behind the delamination boundary. These terms have been empirically shown to have functional dependence on the state of stress at the delamination boundary, i.e. the mixity of shear and opening stresses. Moreover, the total contribution of such inelastic mechanisms has been shown to scale with the thermodynamic work of adhesion, such that the total energy required to produce delamination,  $\Gamma$ , can be simply expressed as,

$$\Gamma = W_{ad} + W_p(W_{ad}) \quad (1)$$

where  $W_{ad}$  is the thermodynamic work of adhesion and  $W_p$  is the sum of the contributions from inelastic dissipation mechanisms. The primary effects of both annealing and interlayers can be easily rationalized in terms of their impact on equation (1), in particular on the  $W_{ad}$  term. Annealing influences the diffusion of segregants and changes the nonequilibrium nature of the interface from the as-deposited state; to a lesser extent it would affect the degree of plasticity in a process zone by changing the yield properties of the film. Interlayers introduce new interfaces, with different values of  $W_{ad}$ . In addition, the work of Russell et. al. (1995) has shown that in the case of Cr and Ti interposed between Cu/SiO<sub>2</sub> interfaces, internal oxidation and intermetallic interphase formation are empirical characteristics of enhanced adhesion.

### 8.13.2.1 Thermodynamic Work of Adhesion

From a thermodynamic standpoint, the *true work of adhesion* of the interface is the amount of energy required to create free surfaces from the bonded materials,

$$W_A = \gamma_f + \gamma_s - \gamma_{fs} \quad (2)$$

where  $\gamma_f$  and  $\gamma_s$  are the specific surface energies of the film and the substrate respectively, and  $\gamma_{fs}$  is the energy of the interface (Figure 1). The true work of adhesion is an intrinsic dependent property of the film/substrate pair; it depends on the type of bonding between the film and the substrate and the level of initial surface contamination.

The true work of adhesion can be measured by the contact angle technique (Lipkin et al., 1998; Furuya et al., 1995). If the tested material particle is in thermal equilibrium on a substrate, then,

$$\gamma_{fs} = \gamma_s - \gamma_f \cos \theta \quad (3)$$

where  $\theta$  is the contact angle between the particle free surface and the substrate (Figure 1). The work of adhesion now can be expressed with the Young-Dupré equation (1805):

$$W_A = \gamma_f + \gamma_s - \gamma_{fs} = \gamma_f (1 + \cos \theta) \quad (4)$$

Particles in thermodynamic equilibrium can be obtained by the sessile drop method (Lee and Lin, 1994) or by annealing (Lipkin et al., 1998; Furuya et al., 1995). In case of the easily oxidized particles such as Cu, annealing must be performed in vacuum. When the surface energy of the film  $\gamma_f$  is known at a given temperature  $T_0$ , at any temperature  $T$  it would be,

$$\gamma_f(T) = \gamma_f(T_0) + (T - T_0) \left. \frac{\partial \gamma_f}{\partial T} \right|_{T=T_0} \quad (5)$$

Solving equations (4) and (5) for the elevated temperature gives the value of the *true (thermodynamic) adhesive energy* (Furuya et al., 1995). If crystallographic faceting occurs upon cooling, a different technique is used to assess the work of adhesion, based on the aspect ratio measurements of the equilibrated crystals (Pilliar and Nutting, 1967). Usually both results from contact angle and aspect ratio measurements agree well for metallic films (Lipkin et al., 1998). Contact angle distribution can be obtained from SEM or AFM image analysis (Lipkin et al., 1998).

Lipkin and others (1998) measured a value for the thermodynamic work of adhesion of gold on sapphire of 0.9 J/m<sup>2</sup>. Furuya and coworkers (1995) calculated adhesive energies of Cu/SiO<sub>2</sub>, Cu/TiN and Cu/TiW interfaces using the contact angle technique with the two latter values being more than double the Cu/SiO<sub>2</sub> value of 0.8 J/m<sup>2</sup>. The true work of adhesion is a constant for a given film/substrate pair, and for metals on ceramic is typically on the order of 1-2 J/m<sup>2</sup>.

For the idealized case of Griffith fracture (Griffith, 1920) the fracture resistance,  $\Gamma_i$ , is assumed to be equal to the thermodynamic work of adhesion,  $W_A$ :  $\Gamma_i = W_A$ . In practice, even brittle fracture is accompanied by some sort of energy dissipation, either through plastic deformation at the crack tip or friction. In this regard, relatively thin films on the order of 100 nm thick can exhibit plasticity during interfacial fracture resulting in an elevated work of fracture.

### 8.13.2.1 Practical Work of Adhesion

Most test methods measure adhesion by delaminating thin films from the substrate. While debonding from the substrate, the film and/or the substrate usually experiences plastic deformation making it difficult to extract the true adhesive energy from the total energy measured. What is measured is the *practical work of adhesion*, or interfacial toughness,

$$W_{A,P} = W_A + U_f + U_s + U_{\text{fric}} \quad (6)$$

where  $U_f$  and  $U_s$  are the energies spent in plastic deformation of the film and the substrate respectively, and  $U_{\text{fric}}$  are the energy losses due to friction. Although the last three terms appear to be simply additive, it should be noted that both  $U_f(W_A)$  and  $U_s(W_A)$  are functions of the true work of adhesion (Jokl et al., 1980) and in many cases  $U_{\text{fric}}(W_A)$  will be as well. Fracture mechanics uses the strain energy release rate,  $G$ , or the crack driving force, as a measure of the practical work of adhesion,

$$G \geq R \quad (7)$$

where  $R$  is the resistance to crack propagation. We will discuss tests for measuring  $G$ , and later consider various resistance terms and several possible ways to interpret that resistance, e.g. phase angle, friction and plastic energy dissipation.

The amount of energy dissipation depends on the mode mixity (phase angle), a relative measure of the amount of shear and normal stress components at the crack tip ( $\Psi = \tan^{-1}(\sigma/\tau) = \tan^{-1}(K_{II}/K_I)$ ). The effect of mode mixity on fracture energy is presented in Figure 2, where amount of energy dissipation is much higher in the pure shear compared to the pure opening fracture mode. Both experimental and theoretical results show this behavior (Hutchinson and Suo, 1992; Liechti and Chai, 1992; Cao and Evans, 1989; Wang and Suo, 1990; Jensen and Thouless, 1993). The most realistic phenomenological descriptions of the functional dependence of the interfacial toughness on the mode mixity are given by Hutchinson and Suo (1992),

$$\Gamma(\Psi) = \Gamma_o \left( \frac{1}{\cos \Psi} \right) + \tan^2 \left\{ \Psi \left( 1 - \frac{1}{\cos \Psi} \right) \right\} \Gamma_o \quad (8)$$

$$\Gamma(\Psi) = \Gamma_o \left( \frac{1}{\cos \Psi} \right) + (1 - \frac{1}{\cos \Psi}) \tan^2 \Psi \Gamma_o \quad (9)$$

where  $K_0$  is the mode I interfacial toughness for  $\phi=0$ , and  $\phi$  is an adjustable material parameter (Figure 3). Note that there is no mode mixity dependence for the ideally brittle material ( $\phi=0$ ), and both solutions reduce to one for  $\phi=0$  and  $\phi=1$ . Strictly speaking, there is always a mode mixity effect in the case of a crack propagating along the interface between two dissimilar materials just due to a mismatch in their elastic properties (Dundurs, 1969). Interfacial fracture mechanics is used to describe crack growth along an interface between two dissimilar isotropic materials. The complex stress intensity factor for bimetals is then expressed as (Hutchinson and Suo, 1992),

$$K = (K_1 + iK_2) = \frac{P}{\sqrt{h}} \left[ \frac{iM}{h^{3/2}} \frac{p}{\sqrt{2}} h^{ie} e^{i\phi} \right] \quad (10)$$

where  $h$  is the film thickness,  $M$  is the bending moment due to load  $P$ ,  $\phi$  is a real angular function,  $p = \sqrt{(1-\nu_1)/(1-\nu_2)}$ , and  $\nu$  is a bimaterial real constant,

$$\nu = (1/2\nu) \ln[(1-\nu_1)/(1+\nu_2)] \quad (11)$$

The Dundurs parameters  $\alpha$  and  $\beta$  for plane strain are,

$$\alpha = \frac{(\nu_1/\nu_2)(1-\nu_1)\nu(1-\nu_2)}{(\nu_1/\nu_2)(1-\nu_2) + (1-\nu_1)} \quad (12)$$

$$\beta = \frac{1(\nu_1/\nu_2)(1-\nu_2)\nu(1-\nu_1)}{2(\nu_1/\nu_2)(1-\nu_1) + (1-\nu_2)}$$

For bimetals the phase angle  $\phi$  is:

$$\phi = \tan^{-1} \frac{Ph \sin \phi + 2\sqrt{3}M \cos \phi}{Ph \cos \phi + 2\sqrt{3}M \sin \phi} \quad (13)$$

In the case of a weakly bonded film on the substrate the interface will be the most likely crack path, although there are cases when the crack can kink either into the substrate or into the film itself (Hutchinson and Suo, 1992). The crack path depends on the phase angle, residual stress and the modulus mismatch between the film and the substrate. When testing thin film adhesion, knowledge of the fracture interface and the phase angle is necessary in order to interpret the results correctly.

There is also a link between the thermodynamic work of adhesion ( $W_A$ ) and the interfacial toughness ( $K_I$ ). For example, when the thin film yield stress is low and  $W_A$  is high, ductile fracture is the most likely mechanism. Conversely, brittle fracture occurs when the film yield stress is high and the true adhesion is low (Lipkin et al., 1998; Lipkin et al., 1996). In the case of a metal film on a brittle substrate, one may improve the interfacial toughness by decreasing the film yield stress (annealing), or by the use of



underlayers that increase the adhesion. We now discuss different techniques for measuring the interfacial fracture toughness of thin films.

### **8.13.3 INTERFACIAL FRACTURE TEST TECHNIQUES**

There are more than one hundred different methods for measuring thin film adhesion that employ different sample geometries. Some tests use continuous films, some require patterning, but all tests use some driving force or stored energy to achieve thin film delamination. The energy may come from the external mechanical force imposed on the film, or it can be stored in the film itself (through the internal film stress). These tests generally measure critical values of applied stress intensity,  $K_i$ , or strain energy release rate,  $G_i$  where  $i$  can be mode I, II or III or of mixed mode character.

Unfortunately, measurement techniques that can quantify the energy of adhesion for films in the as-deposited or as-processed state are limited. While such techniques exist, a combination of difficult specimen preparation and testing techniques along with the complexity of deconvolution have historically led to a reliance on simpler and quicker semi-quantitative and qualitative techniques such as tape and scratch testing. Returning again to the work of Russell et al. (1995) as exemplary, a combination of tape testing and scratch testing is used. The tape test is qualitative and often an all-or-nothing test, useful only for testing weakly adhering films. It precludes observation of incremental improvements from processing optimization. The scratch test is semi-quantitative, in that the normal load at which a predefined failure event or morphology occurs is defined as a measure of adhesion. Similar work by LaFontaine et al. (1990) uses a measure of the depth-dependent nanoindentation hardness as a measure of the adhesion in Cu/Cr, and Ti/SiO<sub>2</sub> film structures. While these semi-quantitative tests are simple and informative, they are incapable of incorporating all the relevant parameters. With regard to the scratch test, the authors rely on the fact that all films are of approximately the same thickness, hardness and residual stress, the substrates are of nearly identical thickness, and the same scratch stylus is used for all tests. Nevertheless, a more quantitative testing procedure is needed.

#### ***8.13.3.1 Sandwich specimen tests***

For the sandwich type of test, a macroscopic fracture mechanics sample is made with a thin film incorporated into the test structure. This is typically done through diffusion bonding, which can alter both the film microstructure and the interfacial adhesion, since the bonding can take several hours and occurs at high temperatures close to the melting point. Usually it acts as an annealing step during the sample preparation, which may not happen in the actual film processing. So, typically these types of measurements do not apply to the films in the as-deposited state. These tests are modifications of classical fracture mechanics tests, for which mechanics has been developed. For an isotropic material, the crack tends to grow in the opening mode I, but in the case of an interface, the crack tends to grow along the interface. For this reason it is important to quantify interfacial fracture toughness as a function of mode mixity.

Many sample geometries are possible, so only the most common ones will be considered. The simplest example is the modified K<sub>IC</sub> specimen (Suo and Hutchinson,

1989; Menningen and Weiss, 1995), where a thin film is bonded between the two pieces of a compact tension sample (ASTM Standard E399-90) (Figure 4). Another version of this test is the double cantilever test, where a thin film is bonded between two rigid elastic plates. For the  $K_{IC}$  test the interfacial fracture toughness can be expressed in the form:

$$K = \frac{P_Q}{B\sqrt{W}} f(a/W) \quad (14)$$

where  $P_Q$  is the load determined from the load-displacement curve,  $B$  is the specimen thickness,  $W$  is the specimen width as defined in Figure 4a,  $f(a/W)$  is a function of  $a$  and  $W$  which is defined in the standard for the homogeneous material (ASTM Standard E399-90). McNaney et al (1995, 1997) provide the elastic compliance solution for the modified compact tension as well as the four-point bend specimens.

In the case of the double cantilever test, the strain energy release rate can be expressed as in Cao and Evans (1989) and Kanninen (1973),

$$G = \frac{12P^2 a_0}{EB^2 H^3} + \frac{AH}{a_0} + B \frac{H^2}{a_0^2} \quad (15)$$

where  $P$  is the fracture load,  $a_0$  is the precrack length, and  $H$  is half the specimen height (Figure 4a).  $A$  and  $B$  are the proportionality coefficients ( $A \approx 1.3$  and  $B \approx 0.5$ ).

It turns out that the presence of a thin middle layer does not shift the phase angle much as compared to the homogeneous case as long as the middle layer is thin compared to the total sample thickness  $2H$  (Suo and Hutchinson, 1989). The importance of both tests is that they provide the interfacial toughness at almost zero mode mixity angle.

Another test which uses a sandwich structure is the Brazil disk test. The Brazil disk test is schematically shown in Figure 4b. In this sample, a thin film is bonded between two pieces of a disk of radius  $R$ . The crack of the length  $2a$  is present in the interface. A load  $P$  is applied at a certain compression angle  $\alpha$  to the crack axis and mode mixity is varied by changing  $\alpha$ . Pure mode I conditions are achieved when  $\alpha = 0^\circ$  and pure mode II when  $\alpha \approx 25^\circ$  (O'Dowd et al., 1992).

Atkinson and co-workers (1982) presented explicit formulae for  $K_I$  and  $K_{II}$  valid for any crack orientation in the homogeneous Brazil disk,

$$K_I = \frac{PN_I}{RB} \sqrt{\frac{a}{b}} \quad (16)$$

$$K_{II} = \frac{PN_{II}}{RB} \sqrt{\frac{a}{b}}$$

where  $a$  is half the crack length,  $b$  is the disk thickness, and  $N_I$  and  $N_{II}$  are non-dimensional functions of the relative crack size,  $(a/R)$ .

O'Dowd and coworkers (1992) provided a stress intensity solution for a bimaterial Brazil disk as follows,

$$K = \frac{YP}{2R} \sqrt{2a} (2a)^{\frac{\alpha}{2}} e^{i\alpha} \quad (17)$$

where  $Y$  is a dimensionless geometric factor,  $\alpha$  is the bimaterial real constant as in equation (11). The dependence of  $\alpha$  and  $Y$  on the compression angle  $\theta$  is not known. Since the crack has two tips, stress intensity factors at each tip will also be different, so  $\alpha$  and  $Y$  must be provided for each crack tip. Brazil disk mechanics for orthotropic materials, as well as an FEM model, are discussed by Huang and co-workers (1996). Mechanics for a Brazil-nut-sandwich specimen (Figure 4b) and different types of failure are discussed by Wang and Suo (1990). The advantage of the test is the ability to change the phase angle by rotating the sample relative to the axis of the applied load.

The last type of the sandwich samples considered here is the four-point bent test (Figure 4c). So far this is the most popular adhesion test for the microelectronics industry. Two elastic substrates with thin films on them are bonded together with another material (typically Cu or epoxy). The upper substrate has a notch in it, and a crack propagates through the substrate and kinks into the interface of interest upon loading. At this point the strain energy release rate reaches steady state, which corresponds to the load plateau in the load-displacement curve. The strain energy release rate can be calculated from the steady state fracture plateau load  $P$  (Charalambides et al., 1989),

$$G = \frac{21 \frac{b}{h} \frac{L}{h} P^2 L^2}{16 E b^2 h^3} \quad (18)$$

where the geometrical parameters  $L$ ,  $b$  and  $h$  are shown in Figure 4c. After passing the lower support line, the crack does not grow stably anymore, and numerical analysis is required to assess  $G$  (Hofinger et al., 1998). The phase angle for the test at steady state crack growth is approximately  $43^\circ$  (Dauskardt et al., 1998). Limitations of the test in terms of the  $K$ -dominant region are discussed in work by Becker and co-workers (1997).

Note that sandwich specimen test analyses do not account for the residual stress in thin films. The ideal test should simulate the practical situation as closely as possible, while also being able to extract the value of practical adhesion. The method must explicitly account for the contribution of the residual stress to the decohesion process. If the test structure has experienced only low temperatures during fabrication, using high homologous temperature ( $T/T_m$ ) processing steps in specimen preparation, such as diffusion bonding, is not desirable, since it can markedly alter interface adhesion properties.

### 8.13.3.2 Bulge and blister tests

The bulge test is analogous to uniaxial tension for bulk materials and has been developed for measuring mechanical properties of thin films. In the bulge test a freestanding thin film "window" is pressurized on one side, causing it to deflect (Figure

5). A stress-strain curve can then be constructed from measured pressure,  $P$ , and film deflection  $\Delta$ .

The pressure-deflection curve is a function of sample geometry, the film's mechanical properties, and residual stress. A spherical cap model was initially used for stress and strain determination in the bulge test (Vlassak and Nix, 1992),

$$\Delta = \frac{Pr^2}{4\sigma h} \text{ and } \Delta = \frac{1}{3r^2\sigma^2} + A \quad (19)$$

where  $\Delta$  is the total bulge height,  $h$  is the film thickness,  $r$  is the bulge radius, and  $A$  is the term which accounts for initial stress in the film. For slack films,  $A=2\Delta_0/3r^2$  with  $\Delta_0$  the height due to the slack in the film. For taut films,  $A=\sigma_0/E'$  with  $\sigma_0$  the initial tensile stress in the film and  $E'$  the biaxial modulus of the tested film.

The relation between pressure  $P$  and deflection  $\Delta$  may be expressed, based on the cap model,

$$P = \frac{c_1\sigma_0 h}{ar^2} + \frac{c_1 E h}{r^4(1-\nu)} \Delta^3 \quad (20)$$

where  $c_1$  and  $c_2$  are geometric parameters of the bulge form. Vlassak, and Nix, (1992) showed the validity of equation (20) for square and rectangular membranes using an energy minimization technique.

The spherical cap model assumes an equi-biaxial state of stress and strain in the bulged film, which is an approximation since the film is clamped and there is no circumferential strain at the edge. There is also an uncertainty in measuring the initial bulge height at the start of pressurization. Finite element analysis has been conducted to overcome such problems (Vlassak and Nix, 1992; Small et al., 1992; Small and Nix, 1992; Paviot et al., 1995) for measurement of biaxial modulus and Poisson's ratio. Mechanics for the blister test is also given in (Hutchinson and Suo, 1992). A disadvantage of this method lay in its difficult specimen preparation. If the film is too thin ( $< 2 \mu\text{m}$ ), it may wrinkle due to the residual stress relief when made freestanding (Small and Nix, 1992).

The blister test is similar to the bulge test with the only difference being that the pressure is increased until the film starts to debond from the substrate, forming a blister. The crack extension force (strain energy release rate) for the blister test is (Hohlfelder et al., 1997),

$$G = P \Delta \frac{k_v}{\Delta} \frac{\Delta^4 + 5\Delta^2}{\Delta^4 + 4\Delta^2} \quad (21)$$

where the coefficient  $k_v$  accounts for the shape of the blister and  $\Delta = [(c_2 E_f')/(c_1 \sigma_0)](\Delta/r)^2$ . The constant  $k_v$  is approximately equal to 1.62 for a circular window and 1.94 for a square window.

Blister tests are often invalid in the case of thin ductile films due to film yielding before decohesion. In order to prevent film yielding, a hard elastic superlayer may be

deposited on top of the film of interest, similar to the superlayer indentation technique. The superlayer can be deposited directly on the freestanding film without causing it to wrinkle. Another problem with the blister test is that a crack often does not propagate uniformly along the perimeter of the blister, making it difficult to interpret the results. A transition between blister bending and stretching is discussed by Wan et al., (1998). For a homogeneous system the phase angle of loading in the blister test ranges from -40 to -90°. A comprehensive analysis of mode mixity in the blister test is presented by Jensen (1998).

### 8.13.3.3 Superlayer test

A test based upon internally developed stresses was proposed by Bagchi and coworkers (1994). Here, residual tensile stresses in a thin film line drive its delamination from a thick substrate. The nondimensional steady state strain energy release rate,  $G_{ss}$ , for a narrow line after crack initiation is,

$$G_{ss}E_f/\sigma_f^2h_f = 1/2 \quad (22)$$

where  $E_f$  is the Young's modulus of the film,  $h_f$  is the film thickness, and  $\sigma_f$  is the residual stress in the film. The corresponding phase angle in this case is about 52° (Bagchi et al., 1994). For the wide line (line width is greater than its thickness) the residual stress is biaxial and the strain energy release rate is,

$$G_{ss}E_f/\sigma_f^2h_f = 1 - \nu_f \quad (23)$$

where  $\nu_f$  is Poisson's ratio of the film. For a typical film thickness of one micron and a residual stress of 100 MPa, the stress-induced energy release rate is on the order of 0.1 J/m<sup>2</sup>. As most interfaces in microelectronic devices have higher debond energies, decohesion is difficult if not impossible under these conditions.  $G_{ss}$  needs to be increased without substantially changing the phase angle. One of the ways to increase strain energy by depositing a thick overlayer (superlayer) on top of the tested structure. For Cu interconnects, Cr was found to be the optimal superlayer (Bagchi et al., 1994; Bagchi and Evans, 1996). The superlayer increases the film total thickness and elevates the total residual stress without changing the tested interface. It is deposited at ambient temperatures (by electron beam evaporation) and does not react with the tested Cu film. More importantly, it has high residual tensile stresses upon deposition. Figure 6 illustrates the test schematically. In the first step, a thin carbon release layer is thermally evaporated and patterned using the bilayer photolithography technique. This layer acts like a precrack for the test structure. Its width is at least twice the Cu film thickness to avoid edge effects on the energy release rate. In the second step, the film of interest (Cu) and the superlayer (Cr) are deposited and patterned to form strips perpendicular to the carbon lines. In order to produce a range of strain energy release rates the superlayer thickness is varied. The metal bilayer structure is cut by wet-etching or ion-milling during the third step. If the strain energy release rate exceeds the adhesion energy, the strips decohere. If

the films stay attached, the adhesion energy was not exceeded and a thicker superlayer should be used.

The debond energy  $G$  is determined by the critical superlayer thickness (Bagchi et al., 1994),

$$G = \sum_i \frac{\epsilon_i^2 h_i}{E_i'} \sum_i \frac{1}{E_i' h_i} P^2 + \frac{12 M_i^2}{h_i^3}$$

$$P = k \frac{E_1 h_1^3 + E_2 h_2^3}{6(h_1 + h_2)}$$

$$k = \frac{6(h_1 + h_2)(\epsilon_1 \epsilon_2)}{h_1^2 + E_2 h_2^3 / E_1 h_1^3 + E_1 h_1^3 / E_2 h_2^3 + h_2^2 + 3(h_1 + h_2)^2}$$

$$M_i = E_i' k$$
(24)

where  $i=1,2$  refers to the two materials in the bilayer,  $h_1$  and  $h_2$ ,  $E_i'$  are the biaxial elastic moduli,  $E_i' = E_i / (1 - \nu_i)$ , the load  $P$  is associated with the residual tension stress,  $\epsilon_i$ , in each layer,  $k$  is the curvature of the debonded layer,  $\epsilon$  are misfit strains:  $\epsilon = \epsilon_i / E_i'$ ,  $M_i$  are the bending moments along the centerline of each layer due to the load  $P$ . (Figure 7)

When stressed superlayers are applied over a large surface area of a film, they will often trigger uniform width, telephone cord, and circular blisters. The blisters provide the data from which interfacial fracture energies can be obtained using solutions for film systems where residual stresses dominate fracture behavior. These solutions were originally derived for single layer film-on-substrate systems (Marshall and Evans, 1984; Evans and Hutchinson, 1984; Hutchinson and Suo, 1992). The work of Bagchi et al. (1994) and Bagchi and Evans (1996) and more recently by Kriesse et al. (1999a) extended these solutions to multilayer systems by treating the multilayer film as a single layer film of the same total thickness with a transformed moment of inertia,  $I_T$ .

The uniform width blister is modeled as a wide, clamped Euler column of width  $2b$  for a blister to form between the multilayer film and substrate under these conditions, the compressive residual stress,  $\sigma_r$ , must exceed the stress for interfacial delamination,  $\sigma_b$ , as follows (Kriesse et al., 1999a; Hutchinson and Suo, 1992),

$$\sigma_b = \frac{\sigma_r}{B h b^2} \left( \frac{E_{\text{film}}}{\epsilon \epsilon_{\text{film}}} I_T \right)$$
(25)

In this expression,  $\nu_{\text{film}}$ , is Poisson's ratio of the film,  $b$  is the blister half-width,  $h$  is the total film and superlayer thickness, and  $B$  is the unit width, which cancels when multiplied by the transformed moment of inertia (Kreise et al., 1999a). The residual stress can then be determined from the blister height and the stress for delamination as follows (Hutchinson and Suo, 1992),

$$\sigma_r = \sigma_b \frac{3\nu^2}{4h^2} + 1 \quad (26)$$

where  $\nu$  is the buckle height and  $\sigma_r$  is given by Kreise et al. (1999),

$$\sigma_r = \sigma_{\text{film}} \frac{h_{\text{film}}}{h} + \sigma_{\text{superlayer}} \frac{h_{\text{superlayer}}}{h} \quad (27)$$

The residual stress and stress for delamination are then used to determine the strain energy release rate for interfacial fracture along the straight side wall portions of the blisters from

$$G(\nu) = \frac{\nu^2 \sigma_b^2 h}{2E} (\sigma_r \sigma_b) (\sigma_r + 3\sigma_b) \quad (28)$$

where  $E$  and  $\nu$  are the thickness-weighted elastic modulus and Poisson's ratio values for the multilayer films. Under steady state conditions the width of the blister remains fixed creating the straight-sided blister configuration with growth occurring along the more or less circular end of the blister. Under these conditions, the steady state fracture energy is given by (Hutchinson and Suo, 1992),

$$G_{ss} = \frac{\nu^2 \sigma_b^2 h}{2E} \left( \frac{\sigma_b^2}{\sigma_r} \right) \quad (29)$$

Figure 8 shows typical  $G(\nu)$  and  $G_{ss}$  fracture locations.

#### 8.13.3.4 Indentation tests

Nanoindentation is normally used for measuring thin film mechanical properties such as the elastic modulus and hardness (described in section 8.13.4 in detail) and used for modeling film fracture behavior. In the case of a brittle, weakly bonded film, indentation tests can be used to delaminate the film from the substrate. From the

delamination, interfacial fracture strengths can be determined (Marshall and Evans, 1984, Rosenfeld et al, 1990, de Boer and Gerberich, 1996a, Vlassak et al, 1997, Drory and Hutchinson, 1996). Basically, the cone (plane stress) and the wedge (plane strain) are the two most popular indenter geometries for measuring brittle thin film adhesion by indentation. Marshall and Evans (1984) provide the analysis for the conical indentation-induced thin film delamination. The strain energy release rate is,

$$\frac{GE_f}{(1-\nu_f)} = \frac{1}{2} h \sigma_I^2 (1 + \nu_f) + (1 - \nu_f) h \sigma_r^2 - (1 - \nu_f) h (\sigma_I - \sigma_b)^2 \quad (30)$$

where  $E_f$  and  $\nu_f$  are the thin film's Young's modulus and Poisson ratio respectively,  $h$  is the total film thickness,  $\sigma_r$  is the residual stress in the film. Here, a sharp diamond tip is indented into the tested thin film, and deforms a volume of  $2V_I$  (Figure 9a) Indentation causes nucleation and propagation of an interfacial crack. If the indenter is driven deep enough, so that the crack reaches its critical buckling length, the film double buckles (Figure 9b) during indentation. If the crack length did not reach its critical buckling length on each side of the indenter, single buckling might occur upon tip removal (Figure 9c). When the tip is removed, the film under indenter is no longer under constraint, so it may form a single buckle even in the initial double-buckling case.

The indentation stress,  $\sigma_I$  can be calculated by using the indenter tip geometry,

$$\sigma_I = \frac{E_f V_I}{2a^2 h (1 - \nu_f)} \quad (31)$$

The indentation volume,  $V_I$  can be calculated from the plastic indentation depth using the tip geometry, and the crack length,  $a$ , can be directly measured by using microscopy or profilometry techniques. If the crack is driven far enough by the indenter (Figure 9b or c), the film can buckle, giving rise to the last term in equation (30) through the Euler buckling stress,

$$\sigma_b = \frac{\pi^2 h^2 E_f}{12a^2 (1 - \nu_f)} \quad (32)$$

In this equation,  $\pi$  is a constant that depends on the boundary condition ( $\pi^2 = 14.68$  for single buckling, and  $\pi^2 = 42.67$  for annular double buckling). The term  $\pi$  is equal to one if the film is not buckled, otherwise it represents the slope of the buckling load versus the edge displacement on buckling as follows,

$$\pi = 1 + \frac{1}{1 + 0.902(1 - \nu_f)} \quad (33)$$

Note that in the case of non-buckling fracture ( $\pi = 1$ ), delamination is only driven by the indentation stress, and the residual stress does not come into play.



A microwedge wedge indentation test (MWIT) has been proposed by de Boer and Gerberich (1996a) for thin metal lines. Here, a diamond wedge is indented perpendicular to the line to cause its debonding. An approach, similar to Marshall and Evans (1984) is employed, where the plastic volume is assumed to transform into the film elastic displacement at the crack tip,

$$G = \frac{E_f V_0^2}{2b^2 h a^2} \quad (34)$$

where  $V_0$  is the half of the total indentation volume,  $a$  is the crack length,  $b$  is the line width, and  $E_f'$  is the plane strain elastic modulus of the film:  $E_f' = E_f / (1 - \nu_f^2)$ . The test accounts for the line buckling, and appropriate solutions are given by de Boer and Gerberich (1996a).

A similar wedge indentation test has been applied by Vlassak et al. (1997) to measure adhesion of hard films on ductile substrates. It is based on the model for the plane strain wedge indentation into a brittle continuous film on a ductile substrate:

$$G = \frac{\sigma_{xx}^2 h}{2E_f} \quad (35)$$

where  $\sigma_{xx}$  is the stress in the film, perpendicular to the wedge line:

$$\sigma_{xx} = \sigma_r + \sigma_f \frac{E_f}{E_f'} \frac{W^2 \tan \theta}{a^2} \quad (36)$$

Here,  $\sigma_r$  is the residual stress in the film,  $W$  is the half width of the wedge indentation,  $\theta$  is the inclination of the face of the wedge to the surface of the film, and  $a$  is the crack length.

The advantage of the wedge indenter geometry is the weaker  $1/a^2$  dependence in equation (34) and (36) compared to  $1/a^4$  for the axisymmetric case (Rosenfeld et al., 1990) which leads to less experimental scatter. The problem with the wedge indentation is the alignment. Usually, wedges are not perfectly symmetric, and it is also extremely difficult to align the wedge perpendicular to the plane of the thin film. Misalignment causes asymmetric crack growth on both sides of the wedge. This effect has been observed on both the micro and macro scales (de Boer and Gerberich, 1996a; Volinsky et al., 1999). A new revision of the wedge indentation test is provided by Begley et al. (2000).

A relatively new idea of a cross-sectional indentation for thin film delamination has been proposed by Sanchez et al (1999). An indentation is made into the substrate cross-section, close to the film interface, which causes the film to debond. The energy release rate can be calculated by knowing the maximum film deflection,  $u_0$ :

$$G = \frac{Eh^3u_0^2}{12(a-b)^2}(1-\alpha)^4(2F + \alpha F\alpha) \quad (37)$$

where  $a$  and  $b$  are the delamination and contact radii respectively,  $\alpha=a/b$ , and  $F$  is defined as:

$$F(\alpha) = \frac{2 \ln \alpha + \frac{1+\alpha}{1-\alpha} \ln^2 \alpha}{\left[(1+\alpha) \ln \alpha + 2(1-\alpha)\right]^2} \quad (38)$$

and  $F' = dF/d\alpha$ . This test is particularly useful, since the film is not indented directly, and the crack initiates in the brittle substrate, which limits the amount of plastic deformation.

Unfortunately, indentation tests on thin films of interest cannot often be used directly in the case of ductile films on brittle substrates. A ductile strongly adhered film would form a plastic pile-up around the indenter rather than delaminate from the substrate. Even if the film debonds from the substrate, delaminations are not reproducible, and plastic pile-up has to be taken into account. Such problems have been solved with the introduction of the superlayer indentation technique.

#### **8.13.3.5 Superlayer indentation test**

Kriese and co-workers (1999a,b) have combined the idea of the superlayer test with the indentation test. Deposition of a hard film, capable of storing significant amounts of elastic energy over the film of interest, can result in multilayer debonding (Bagchi and Evans 1996) producing large delamination radii (Figure 7). It also acts like a capping layer, preventing plastic flow of the underlying film in the vertical direction, and adding normal stresses at the interfacial crack tip (He et al, 1996). Presence of the superlayer provides an additional driving force for de-adhesion as shown in Figure 7. For the superlayer indentation test a sharp indenter also provides additional stress for crack initiation/propagation at the interface.

A modified Marshall and Evans (1984) analysis was used, and the laminate theory was employed in order to calculate the necessary terms in equation (30) for the bilayer (Kriese and coworkers, 1999a,b). In the case of a highly compressed superlayer, the indentation stress is being added to the residual stress, so multiple superlayer depositions are avoided. Blanket films can be tested in the as-deposited, as-processed conditions; no pattern transfer is necessary. When an indenter penetrates through a bilayer, it causes film debonding and blister formation, which can be seen afterwards in an optical microscope with Nomarski contrast (Figure 10).

Properties of the films such as elastic modulus, Poisson's ratio, as well as the tip angle and radius, are needed for an adhesion assessment. Generally speaking, there are two measurements that are necessary for strain energy release rate calculations. From the standpoint of blister formation, both blister diameter and indentation depth are required. Blister diameter is measured in the optical microscope with Nomarski contrast. Using the Oliver-Pharr (1992) method, inelastic indentation depth,  $\Delta_{pl}$ , is calculated from:

$$P = A(\Delta \sigma_{pl})^m \quad (39)$$

where  $P$  and  $\Delta$  are the load and displacement from the 65% of the unloading slope of the load-displacement curve respectively,  $A$  and  $m$  are fitting parameters. The indentation volume,  $V_I$ , is calculated from the inelastic depth by using the tip geometry. The indentation stress can be calculated from equation (31), assuming the conservation of volume.

The solution for the buckling stress in the bilayer is also provided by Kriese and co-workers (1999a,b). The advantage of the superlayer indentation test is that it provides interfacial toughness measurements over a wide range of phase angles. Prior to buckling the phase angle is equal to the real angular function,  $\phi$ , and at the onset of buckling a rapid decrease occurs.

#### 8.13.3.6 Scratch tests

In a typical scratch test a stylus or a diamond tip is drawn across the film surface. The test could be treated as a combination of two operations: normal indentation and horizontal tip motion. A vertical increasing load is applied to the tip during scratching until the coating detaches from the substrate. The minimum critical load  $P_{cr}$  at which delamination occurs is used as a measure of the practical work of adhesion (Benjamin et al., 1960; Burnett and Rickersby, 1987),

$$P_{cr} = \frac{r^2}{2} \frac{2EW_{A,P}}{h} \quad (40)$$

where  $r$  is the contact radius and  $h$  is the film thickness. This analysis is applicable only when the tensile stress normal to the film surface drives delamination.

Venkataraman, et al. (1992, 1993a) developed a model for estimating the energy per unit area  $G_o$  stored in the film from the scratch elastic stress distribution, which was modified later to account for residual stresses in the film (Moody et al., 1998),

$$G_o = \frac{\sigma_r^2 h}{2E} + \frac{\sigma_{ij}^2 h}{2\mu} + \frac{\sigma_{ij}^2 h}{2E} \quad (41)$$

where the first term comes from the contribution of the residual stress  $\sigma_r$ ,  $\sigma_{ij}$  and  $\sigma_{ij}$  are the average elastic shear and normal stresses in the delaminated film,  $h$  is the film thickness,  $\mu$  is the film shear modulus.  $\sigma_{ij}$  and  $\sigma_{ij}$  can be determined from the scratch trace geometry observed in SEM.

For a symmetric scratch trace, the strain energy release rate can be found using a circular blister analysis (Moody et al 1998):

$$G_o = \frac{(1 - \nu^2)h\sigma^2}{E} \left(1 - \frac{\sigma_b}{\sigma}\right) \frac{\sigma_b}{\sigma} \quad (42)$$

where  $\sigma_b$  is the Euler buckling stress, defined by equation (32) for a circular blister with  $\nu = \nu$  and  $\sigma$  is defined by equation (33) (Hutchinson and Suo, 1992).

M. de Boer, et al. (1996b, 1997) adjusted the original scratch test for fine line structures. A schematic of the new test, the precracked line scratch test (PLST), is shown in Figure 11. A thin metal line on a substrate is pushed with the asymmetric diamond wedge from one end. The thin line has a processed precrack in the form of a carbon layer, which makes it a real fracture mechanics specimen. It is similar to the superlayer test of Bagchi and Evans (1994, 1996). The precrack portion of the line is deformed elastically in the beginning of the test until the crack propagates. When the crack reaches its critical buckling length at a certain critical load,  $P_{cr}$ , the film buckles. At the point of buckling the strain energy release rate can be calculated as:

$$G = \frac{\sigma^2 h}{2E_f} = \frac{(P_{cr} - P_{fric})^2}{2b^2 h E_f} \quad (43)$$

Here  $\sigma$  is the stress in the cracked portion of the line,  $b$  is the line width,  $P_{cr}$  and  $P_{fric}$  are the critical buckling load and the friction load respectively, which are measured experimentally.

The test is applicable to the hard lines, capable of bearing a load to the crack tip without plastically deforming; it was originally carried out on W thin lines on oxidized silicon wafers. The phase angle just prior to buckling is  $52.7^\circ$ , and decreases rapidly after buckling due to the increased normal stress component. Post-buckling solutions for the strain energy release rate are provided in (de Boer and Gerberich, 1996a; Volinsky et al., 1999).

The mechanics for the PLST has been modeled using the macroscopic setup of a polycarbonate line bonded to steel with cyanoacrylate (Volinsky et al., 1999). This allowed a construction of the strain energy release curve throughout the whole test, before and after line buckling (Figure 12). Prior to line buckling, an R-curve behavior is observed, as the strain energy release rate increases with the crack length. At the point of buckling there is unstable crack growth, as the strain energy release rate,  $G$ , exceeds interfacial fracture toughness,  $\Gamma(\theta)$  (Figure 13). This situation is analogous to circular blister buckling (Hutchinson and Suo, 1992). At a certain level of stress,  $\sigma_{buckle}$ , and a certain crack length,  $a_1$ , the line starts to buckle, at which point the interfacial fracture toughness drops under the influence of a decreasing phase angle of loading. The crack arrests at  $a_2$  when the interfacial fracture toughness exceeds the strain energy release rate. At this point fracture is dominated by the mode I stress component, and continues to grow stably until the total line decoheres (Volinsky et al., 1999).

The PLST allows measuring the interfacial fracture toughness over a wide range of phase angles of loading. For this test to work, the material must transfer the stress down to the crack tip without plastically deforming. As a consequence, this test may not work with ductile metals such as Cu, Al and Au. The problem may be solved by using a

stiff hard superlayer on top of the film of interest, just like in the superlayer indentation test.

### 8.13.4 NANOINDENTATION-MECHANICAL PROPERTIES

For analysis of most adhesion test data, the knowledge of the thin film mechanical properties is required. In the previous section almost every expression for the strain energy release rate has the thin film elastic modulus. The modulus can be measured by the microbeam cantilever deflection technique (Weihs et al., 1988, Baker and Nix, 1994), but the easiest way is by means of nanoindentation (Oliver and Pharr, 1992), since no special sample preparation is required and the same technique can be used for measuring film adhesion.

#### 8.13.4.1 Elastic Properties

##### 8.13.4.1.1 Load-vs-displacement curves

To begin with, the elastic modulus of a material can be determined using nanoindentation. The method first developed by Loubet et al., (1984) and refined by other researchers (Doerner and Nix, 1986; Oliver and Pharr 1992), uses the geometry shown in Figure 14. In this test, a diamond indenter is driven into a sample while continuously measuring load and displacement. From analysis of the unloading data, stiffness and elastic modulus can be determined. The “unloading” slope analysis assumes that upon the initial unloading the sample behaves in an elastic manner similar to a flat punch of the same contact radius in contact with the sample. This allows the use of Sneddon’s models (Sneddon, 1965) of flat punches in contact with surfaces under elastic loading. In this case, the remote load-displacement relationship can be used to relate the stiffness,  $S$ , from the unloading curve to the area of contact,  $A$ , and the reduced elastic modulus,  $E^*$ ,

$$E^* = S \frac{\sqrt{\pi}}{2} \frac{1}{\sqrt{A}} \quad (44)$$

where

$$\frac{1}{E^*} = \frac{1 - \nu_1^2}{E_1} + \frac{1 - \nu_2^2}{E_2} \quad (45)$$

In these equations,  $E_1$  and  $\nu_1$  are the modulus and Poisson’s ratio of the sample and  $E_2$  and  $\nu_2$  are the modulus and Poisson’s ratio of the indenter.

The important parameter in equation (44) is the stiffness and therefore it’s inverse, compliance. Compliance is the result of many contributing factors. The sample contributes a compliance as does the loading system. Assuming compliance of the sample-tip interaction is a function of the area of contact while compliance from the test frame is constant, it is possible to relate the measured compliance to the contact area of the indenter with the sample as follows,

$$C = C_{\text{frame}} + \frac{\sqrt{A}}{2E} \frac{1}{\sqrt{A}} \quad (46)$$

In this equation, the slope of the line correlates directly to the reduced elastic modulus and the offset to the frame compliance. Indentations into standard samples with known elastic constants can allow one to empirically determine the relationship between the area of the tip and the penetration depth.

Several assumptions are implied in this model. First, the sample must not “pile up” around the indenter tip. Many metallic materials (particularly with low work hardening coefficients) do indeed pile up around indenter tips during a test (Samuels and Mulhearn, 1957, Bahr and Gerberich, 1996b), resulting in possible inaccuracies in the determination of depth of contact. Secondly, the tip itself must have a large included angle. Sharper angles will cause larger out of plane deformations, and this will impact the analysis (Pharr, 1998).

#### 8.13.4.1.2 Continuous stiffness

A newer, powerful technique for nanoindentation, coined "continuous stiffness", allows the contact stiffness to be measured continuously during the course of a test enabling the modulus and hardness to be calculated as a function of depth. The technique imposes a sinusoidal forcing function (see Figure 15) at about 45 Hz., and uses this signal to calculate the contact stiffness from,

$$\left| \frac{P_{OS}}{h(\omega)} \right| = \sqrt{\{(S^{\omega} + C_f)^{\omega} + K_S \omega m \omega^2\}^2 + \omega^2 D^2} \quad (47)$$

or from the phase difference between the displacement and force signals from:

$$\tan(\phi) = \frac{\omega D}{(S^{\omega} + C_f)^{\omega} + K_S \omega m \omega^2} \quad (48)$$

where  $C_f$  is the compliance of the load frame,  $K_S$  is the stiffness of the column support springs,  $D$  is the damping coefficient,  $P_{OS}$  is the magnitude of the force oscillation,  $h(\omega)$  is the magnitude of the resulting displacement oscillation,  $\omega$  is the frequency of oscillation,  $\phi$  is the phase angle between the force and displacement signals, and  $m$  is the mass (Oliver and Pharr, 1992). Material properties can then be calculated at each of these “initial” unloading sequences. A dynamic model for this continuous stiffness setup is shown in Figure 16. Continuous stiffness is particularly useful for indentation of thin film structures since material properties can be determined for both the film and substrate in one easy test (see Figure 17 for an example of the hardness measured for a 200 nm thick Au film on sapphire and a 200 nm Au film on 6 nm of Cu on sapphire, from (Woodcock, 2002). The film thickness can also be determined by careful analysis of the changes in the modulus and hardness curves as a function of depth.

### 8.13.4.1.3 Thin film-substrate effects

King developed a model (King, 1987) which relates the measured stiffness to the expected stiffness of the substrate to determine the film properties. Based on the measured or calculated areas, the substrate stiffness,  $S_o$ , is determined. The modulus of the film is then given by

$$E_f = (1 - \nu_f^2) \frac{1 - e^{-c\sqrt{A}/t}}{\frac{1 - \nu_o^2}{E_o} + \frac{1 - \nu_s^2}{E_s} e^{-c\sqrt{A}/t} + \frac{1 - \nu_f^2}{E_f}} \quad (49)$$

where the subscript f refers to film properties, t is the film thickness, a is the contact area parameter given by  $\sqrt{A}$ , S is the sample stiffness from a given indentation (after correcting for the frame compliance by inverting the measured stiffness, subtracting the frame compliance from the measured compliance, and inverting that result to obtain the stiffness), and c is an empirically determined parameter related to the ratio a/t and the geometry of the indenter tip. The parameter c was calculated by King to be between 0.3 and 2. This is only one of many available substrate corrections possible (see for instance Saha and Nix, 2001), but most follow the basic assumption that the substrate can influence the elastic modulus which is calculated by nanoindentation.

### 8.13.4.2 Plastic Properties

While the elastic properties are needed for indentation induced fracture testing, the plastic properties of the films will also play a significant role, as plasticity in the film will limit the amount of stored elastic strain energy which can be present to drive a fracture. The original method of hardness testing was indeed to measure plastic, not elastic, properties. Traditional hardness tests have been used for decades to measure the resistance of a material to deformation. In the late 18th and early 19th century several attempts were made to rank the deformation of materials by scratching one material with another. If the scratching material marked the tested material, the scratching material was considered "harder" than the scratched material. While this was useful for comparative purposes (and is still referred to as the Mohs hardness scale), there remained the problem of quantifying hardness. In the late 19th century work by Hertz (Hertz, 1896; Auerbach, 1893) brought about early examples of static indentation testing. In these cases, the samples (either balls or flat plates) were probed with a ball of a given material, and the deformation was measured by considering the contact area between the ball and sample.

It was not until the early 1900's (Brinell, 1903) that a standard method of evaluating hardness was presented, based on applying a fixed load to a hard spherical indenter tip into a flat plate. After 15 to 30 seconds, the load was removed and the diameter of the impression was measured using optical microscopy. The Brinell hardness number (BHN) is defined as

$$BHN = \frac{2P}{\pi D^2 \sqrt{1 - \frac{d^2}{D^2}}} \quad (50)$$

where P is the applied load, D the diameter of the indenter ball, and d is the chordal diameter of the residual impression. Note that this method evaluates the load applied to the *surface* area of the residual impression. However, the Brinell test has been shown to be affected by both the applied load and diameter of the ball used for the indenter.

#### 8.13.4.2.1 Yield strength

The idea that hardness should be a materials property, and not dependent on test method, led to the observations that the parameter which remains constant for large indentations appears to be the mean pressure, defined as the load divided by the *projected* contact area of the surface. Meyer (cited by Hoyt, 1924) suggested that the hardness should therefore be defined as,

$$H = \frac{4P}{\pi d^2} \quad (51)$$

This type of hardness measurement is alternately referred to as the mean pressure of an indentation, and noted as either  $p_0$  or H in the literature. Depending on the shape of the indenter and the friction between the indenter and material, the relationship for mean pressure and yield strength can vary. However, the basic relationship proposed (Tabor, 1951) is

$$\sigma_y \approx \frac{1}{3} p_0 \quad (52)$$

This has been shown experimentally by Tabor and others to be an adequate relationship for materials which are elastic - perfectly plastic. For materials which work harden, the effective strain around the indenter should be considered. As described by Meyers, and quantified by Tabor, the effective strain,  $\epsilon$  (in %) around an indenter tip is approximately

$$\epsilon = d/D * 20 \quad (53)$$

For a spherical indenter, where d is the diameter of the impression and D the diameter of the ball making the indentation. The development of the Vickers (or Diamond Pyramid Hardness) indentation test followed the basic method of the Brinell test, but replaced the steel ball with a diamond pyramid ground to an included angle between faces of  $136^\circ$ . It is interesting to note that the angle chosen was based on the Brinell test. It had become common to make indentations with the Brinell method to residual indent diameters corresponding to 0.25 to 0.5 of the ball diameter. The average



of these are 0.375, and if a pyramid is formed around a spherical cap such that the ratio of the chordal diameter to ball diameter is 0.375, the angle must be 136°. After applying a load, the indent is imaged, and the diagonals of the indentation are measured. The Vickers hardness is then defined as,

$$DPH = \frac{2P \sin \frac{136^\circ}{2}}{d^2} \quad (54)$$

where DPH is the Diamond Pyramid Hardness number, P is the load applied in grams, and now d is the length of the diagonals in mm (usually the average of the two diagonals). This is analogous to the Brinell test, in that the DPH is the ratio of the load to the *surface* area of the indentation. The main advantages of this method is that there is a continuous scale between very soft and very hard materials, and that the DPH is constant over a wide range of loads until very low loads (less than 50 - 100 g) are reached.

Using the same method by which the angles for the Vickers test were decided it is possible to come up with an effective strain around an indenter tip. For example, the "effective" strain which a Vickers or Berkovich tip produces is approximately 8%. So for materials which work harden, the tip geometry can be used to probe different effective strains, making it possible to begin to extract "indentation stress strain curves".

The nanoindentation method of extracting hardness is analogous to the Meyer's hardness; by measuring the applied load and the projected area of contact under load, a mean pressure very similar to the Meyer's hardness is determined.

#### 8.13.4.2.2 Bulk materials

The experiments of Atkins and Tabor (1965) demonstrated that the hardness as a function of cone angle changes with the amount of work hardening strain present in the sample. Materials, which were work hardened prior to indentation (i.e. have relatively elastic-perfectly plastic stress strain behavior), exhibited either constant hardness or increases in hardness over the range of indenters used in the present study. Annealed materials tended to exhibit a decrease in hardness as the cone angle was increased. Increasingly sharp indenter tips will lead to observed increases in hardness, this is a measurement and not a materials effect.

As the field of nanoindentation continues to grow, the technique is being used for a wide variety of testing situations spanning multiple disciplines. One common trend, however, is the push to smaller and sharper tips for sampling near surface properties and small volumes. Unfortunately, several problems can arise with the use of these sharper tips. It has been shown (Hay and Pharr, 1998) that sharp tips are difficult to calibrate correctly, especially at very shallow depths. This problem manifests itself as a disparity in the calculated hardness and modulus due to length scale issues in the tip geometry that are not accounted for in traditional indentation mechanics.

One large-scale limitation of indentation techniques is that primarily blunt angle tips are used (such as the Berkovich or Vickers geometry). This leads to problems in achieving lateral resolutions better than 50 nm, as a 10 nm deep indentation has a contact

radius of approximately 50 nm. For probing nanostructured features, it is also necessary to position the tip in relationship to the surface using non-optical imaging techniques. A common method in this case is to couple the indentation equipment with scanning probe microscopy (SPM), where the surface can be imaged prior to indentation. In SPM, tips 60° or sharper are used to improve the lateral resolution of the image, and are commercially available. Many researchers now using SPM techniques to perform nanoindentation are utilizing the same tip to both indent and image (Tian et al., 2000). This creates a controversy between either using a tip that is robust and developed for indentation and one that is fragile and deforms with an additional “cutting” mode rather than the traditional indentation deformation mechanics. However, with the advent of nanostructured materials, researchers are being forced to choose either high lateral resolution or an indentation approach based in traditional methodologies. With the use of sharp tips at shallow depths, traditional measures of hardness appear to be unable to fully define the plastic deformation around these small indents. If the measured hardness values cannot be fully trusted, perhaps revisiting an early parameter  $c/a$ , where  $c$  is the radius of the plastic zone and  $a$  is the contact radius of the indentation, will be more useful than continuing to use hardness even if the tip is well calibrated.

#### 8.13.4.2.3 Indentation size effects

The ratio of the plastic zone size to the contact radius,  $c/a$ , will measure the extent of plastic deformation. According to Johnson's conical spherical cavity model of an elastic - plastic material (Johnson, 1970), the plastic zone is determined by

$$\frac{c}{a} = \frac{E^* \tan \phi}{6 \sigma_y (1 + \frac{1}{2} \frac{c}{a})} + \frac{2}{3} \frac{1 + \frac{1}{2} \frac{c}{a}}{1 + \frac{1}{2} \frac{c}{a}} \quad (55)$$

where  $\phi$  is the angle between the face of the cone and the indented surface,  $90^\circ - \phi$ , and  $E^*$  is again the reduced modulus of the indenter and substrate. When the ratio  $E^* \tan \phi / \sigma_y$  is greater than 40, Johnson suggests that the analysis of elastic-plastic indentation is not valid, and that the rigid-plastic case has been reached. Once the fully plastic state has been reached, the ratio  $c/a$  becomes about 2.33 (Johnson, 1985).

Another model of the plastic zone size based upon Johnson's analysis has been developed (Kramer et al., 1999) whereupon the plastic zone boundary,  $c$ , is determined by,

$$c = \sqrt{\frac{3P}{2 \sigma_y}} \quad (56)$$

where  $P$  is the load, and  $\sigma_y$  is the yield strength of the material. Assuming the fully plastic state, where  $p_0 \approx 3 \sigma_y$ , the ratio  $c/a$  can be determined by,

$$\sigma_y = \frac{1}{3} p_o = \frac{P}{3a^2} \quad (57)$$

Substituting equation (57) into (56) gives,

$$\frac{c}{a} = \frac{3}{\sqrt{2}} \approx 2.12 \quad (58)$$

These measurements of plastic zone diameters can be made on the surface of the sample using scanning probe techniques, as shown in Figure 18. This phenomena has been demonstrated for several bulk materials (Bahr and Gerberich, 1996b) and does hold to very small depths and with sharper indenter tip angles (Kramer et al., 1999; Woodcock and Bahr, 2000). Indentations into single crystals of Fe-3%Si generate significant pile up lobes corresponding to the crystallographic nature of the indentation. For the purposes of this discussion only, the size of the lobes is considered for measurements of  $c$ . It is therefore expected that the ratio  $c/a$  will be greater than in the bulk polycrystalline case where slip is fully developed to the shape of the indenter and a variety of slip systems are activated. All the indentations in this study were imaged to assure self-similarity, and therefore the effective included angle of the indenter is assumed constant for all indentations in the following data. Obviously, the assumption that the deformed region on the surface corresponds to the deformed region underneath the indenter tip must be made to utilize this analysis technique.

Indentations were made with three tips, a standard Berkovich geometry tip, a "cube corner" tip which has a 90° angle between the edge and face of a three sided pyramid, and a 90° cone which has a 1 μm root radius. For the Berkovich tip the indentations show an indentation size effect, the material appears to be harder at smaller sampled volumes. However, sharper tips show a slightly different behavior at the smallest depths sampled.

A mechanistic solution to the problem of the indentation size effect lies in the formulation of strain gradient plasticity models (Fleck and Hutchinson, 1993) for microindentations, and for nanoindentations (Nix and Gao, 1998). The Nix-Gao model depends on the idea of geometrically necessary dislocations, which are formed to accommodate the permanent deformation around the indenter. The hardness at any indentation depth could then be calculated by:

$$\frac{H}{H_0} = \sqrt{1 + \frac{h^*}{h}} \quad (59)$$

where  $H_0$  is the hardness at infinite indentation depth,  $h^*$  is a constant depending on material length scale and indenter geometry, and  $h$  is the contact depth of the indentation test. This accounts for hardness due to both geometrically necessary dislocations and statistically stored dislocations, but also makes the assumption that the hardness is related to the yield strength by a factor of three. A fit to the Nix and Gao model for the data using the Berkovich tip is shown in Figure 19. Using this method, the hardness at "infinite" depth is 1.6 GPa, and a yield strength of 533 MPa. However, for sharper tips

the trends do not hold in the same way, as shown in Figure 20 for a cube corner tip (Woodcock and Bahr, 2000).

When Johnson's cavity model (equation 55) is solved for yield strength, and formulated in a similar manner as a function of contact depth, a similar value of yield strength at infinite depth can be reached. When this ratio is examined, as shown in Figure 21, both tips exhibit an identical size effect behavior, and extracting the yield strength from equation (55) gives a yield strength of either 133 MPa (Berkovich) or 600 MPa (cube corner), bracketing the value using the strain gradient model of Nix and Gao (1998).

#### 8.13.4.2.4 Thin films

Since there is a contribution of plastic energy dissipation to the fracture process, the maximum amount of this energy would be controlled by the film yield stress. In the case of a thin film, the yield stress is typically much higher than for a bulk material (Kramer et al., 1999). This is partly explained by the Hall-Petch type relationship between the film yield stress,  $\sigma_y$ , and its grain size,  $d$ :

$$\sigma_y = \sigma_i + kd^{-n} \quad (60)$$

where  $\sigma_i$  is some intrinsic stress, independent of the grain size  $d$ , and  $n$  is typically between 0.5 and 1. Since the grain size of a thin film scales with the film thickness,  $h$ , the latter can be used instead of the grain size as the scaling parameter (Wei and Hutchinson, 1997)

$$\sigma_y = \sigma_i (1 + \sigma_i h^{-0.5}) \quad (61)$$

where  $\sigma_i$  is a constant. For a metal film the yield stress can be approximated as one-third of the hardness measured by indentation (Tabor, 1951). However, it has been found that for very thin films where penetration depths are small, that the yield strength is often higher than that given by equation (61). This has been attributed to either a substrate or indentation size effect (Kramer et al., 1999). To avoid this, a technique also used is to determine the yield strength by back calculating it from the observed elastic-plastic boundary described in equation (56). Such yield stress data for sputter deposited Cu films can be found in (Tymiak et al., 2000). While the algorithm used by Wei and Hutchinson gives values about 10% higher than “observed,” the uncertainty in the elastic-plastic boundary is such that equation (61) easily applies to both sets of data. In a similar way, we have extracted data from aluminum (Vinci et al., 1995) and gold (Venkataraman and Bravaman, 1992; Evans et al., 1999) films to arrive at similar values of the yield stress.

In all cases, having the ability to measure the properties of the film of interest for interfacial fracture testing is a critical component of accurately determining the toughness of the interface. Both elastic and plastic properties can be measured either prior to or post adhesion testing in many cases. These measurements, and the ability to determine relative effects of parameters such as plastic flow and yielding, will greatly impact the separation of thermodynamic work of adhesion and the practical work of adhesion which includes other dissipative properties such as the motion of dislocations.

### 8.13.5 THIN FILM FRACTURE

In this section, property and fracture data are gathered from a number of sources for films in surface, embedded and multilayer thin film systems. The data include as-deposited and diffusion bonded films and were obtained using a variety of test techniques with the emphasis on data obtained using nanoindentation test techniques. All of these data were collected for films mostly below several microns in thickness. The data are given in Table 5.1 (Volinsky et al., 2002) and grouped into ceramic and metallic film systems with emphasis on nitride films and copper, gold, and aluminum films due to their commercial significance. Presentation of the data for these systems includes a brief discussion of applications that motivated studies to date and a detailed discussion of the techniques used to determine fracture energies. Discussion of the results is designed to show how nanomechanical testing fits into the scope of test techniques available.

#### 8.13.5.1 *Ceramic and Refractory Metal Films*

Ceramic and refractory films are used in many applications where unique properties are needed to insure performance and reliability (Mittal, 1976). Of particular interest are thin tantalum nitride films. They are used extensively as thin film resistors in microelectronics applications because of their excellent long-term stability and low temperature coefficients of expansion (Adams and Kramer, 1976; Au et al., 1990). However, they are sputter deposited, which produces films with high structural defect contents and high residual stresses that can alter both the physical and mechanical properties of the films (Klockholm, 1971; Sun et al., 1975). Tantalum nitride films have also emerged as promising diffusion layers for copper interconnects while providing good adhesion between the copper lines and silicon dioxide substrates (Lane et al., 2000). In this application, the adhesive strength must withstand the high residual stresses associated with thermal expansion mismatch and film growth processes as well as the high back stresses developed during electromigration processes in copper lines.

##### 8.13.5.1.1 *Tantalum nitride*

The potential for high compressive residual stresses inherent in sputter deposited tantalum nitride films to trigger film failure motivated a study of resistance to interfacial fracture for this film system. This study employed nanoindentation (Doerner and Nix, 1986; Wu et al., 1988; Oliver and Pharr, 1992; Venkataraman et al., 1993b) and continuous nanoscratch testing (Wu, 1991; Venkataraman et al., 1992; Venkataraman et al., 1993b; Venkataraman et al., 1993c). Use of these test techniques maintained the as-deposited free surface configuration of production monitors without additional sample preparation. The indentation fracture tests were easy to perform with strain energy release rates determined from mechanics-based analyses (Marshall and Evans, 1984; Evans and Hutchinson, 1984; Hutchinson and Suo, 1992). However, the force that can be applied was limited in magnitude and extent. The continuous nanoscratch tests applied a much greater force over a larger area in comparison with indentation tests but lacked a rigorous derivation of stress distributions and strain energy release rates (Wu, 1991;

Venkataraman et al., 1992; Venkataraman et al., 1993b; Venkataraman et al., 1993c). Nevertheless, good approximations for strain energy release rates were obtained using blister and buckling solutions for systems where residual stresses dominate fracture behavior (Marshall and Evans, 1984; Evans and Hutchinson, 1984; Hutchinson and Suo, 1992).

The indentation fracture tests were conducted using a conical diamond indenter with a nominal 1  $\mu\text{m}$  tip radius and a 90° included angle. The indenter was driven into the films at a loading rate of 500  $\mu\text{N/s}$  until a portion of the film spalled from the substrate. Figure 22 shows a load-displacement curve where the displacement excursion defines the onset of fracture. In all cases, fracture occurred by reverse or double buckle formation during indentation with the material under the indenter pinned to the substrate. There were no observations of buckling or fracture when tests were stopped prior to the displacement excursion. Furthermore, loading beyond the point of rapid excursion did not lead to additional crack growth. These observations clearly show that interfacial crack growth and film fracture occurred rapidly after crack nucleation.

It could not be determined if crack advance was driven to completion from the stored energy at the onset of crack nucleation or if additional crack growth occurs as the indenter drove into the film and substrate. Nevertheless, it was evident that not all displaced material was forced into the film contributing to film stress. Since the tests were run at ever increasing maximum load, atomic force microscopy was used to characterize the evolution of the indentation process and showed that two fifths of the displaced material was thrust up around the indenter prior to film failure (Moody et al., 1998; Venkataraman et al., 1994). Assuming that 60 percent of the displaced material was compressed into the film, the average strain energy release rate ranged from 9.8  $\text{J/m}^2$  at the first indication of fracture to 13.2  $\text{J/m}^2$  at the end of the fracture. A phase angle of loading equal to -56.5° for the upper limit was obtained by back-calculating an effective loading parameter,  $(\sigma_c/\sigma_f)^*$  from the measured fracture energy,  $\Gamma$ , and using solutions for unpinned circular blisters (Marshall and Evans, 1984; Hutchinson and Suo, 1992).  $\sigma_c$  is the delamination stress for a circular blister. This gave an average mode I value of 7.2  $\text{J/m}^2$ .

The nanoscratch tests were conducted using a conical diamond indenter with a nominal 1  $\mu\text{m}$  tip radius and a 90° included angle that was simultaneously driven into the films at a loading rate of 500  $\mu\text{N/s}$  and across the films at a rate of 0.5  $\mu\text{m/s}$  to force film failure. Failure in the as-deposited films occurred by the formation of large spalls as shown in Figure 23a. The fractures occurred consistently at loads near 100 mN and were accompanied by a sharp increase in indenter depth and tangential load as shown in Figure 23b. The normal loads were much lower than required for indentation fracture. The fractured substrate surfaces were distinctly interfacial in character with no evidence of tantalum nitride within the limits of energy dispersive spectroscopy. Circular blister solutions gave an average strain energy release rate of 15.5  $\text{J/m}^2$ , a phase angle of loading equal to -60.1°, and a corresponding mode I value of 8.2  $\text{J/m}^2$ .

In two tests the initial spalls triggered uniform width buckles that ran back along much of the scratch track lengths as shown in Figure 24. These uniform-width buckles provided a third approach to determine strain energy release rates for interfacial fracture of these films. Using uniform blister width solutions gave an average interfacial fracture

energy of  $17.5 \text{ J/m}^2$ , a phase angle of loading of  $-53.2^\circ$ , and a mode I fracture energy of  $9.9 \text{ J/m}^2$  were calculated. The values from each of the three tests are in very good agreement. In all cases, the values are significantly higher than van der Waals forces and forces for chemical bonding. However, they are consistent with fracture of an amorphous oxide that forms on the surface of alumina substrates during backsputter cleaning procedures (Moody et al., 1998).

When an interlayer of aluminum was added to the system, three types of failure were initiated (Bahr et al., 1997). Figure 25 shows three load depth curves into 500 nm of  $\text{Ta}_2\text{N}$  on 28 nm of Al on a sapphire substrate. An optical micrograph taken after the sample was removed from the indenter is shown in Figure 26. While delamination and spalling occurred for indents A and B, indent C exhibited a delaminated region with no evidence of spalling. Acoustic emission (AE) was used to monitor elastic waves which propagated from the film delamination event (Bahr and Gerberich, 1998). The AE voltage signals from curves A, B, and C are shown in Figure 27. For comparative purposes, the signal from curve C has been multiplied by a factor of 10. It is clear that a failure did occur during unloading on curve C. The delamination alone gave an AE signal that was significantly smaller than the spalling events. This is due to the fact that when a film buckles, a fraction of stored strain energy is released, which is the driving force for crack advance. However, a buckled film still contains a significant amount of strain energy. When a film spalls, all of the energy which was stored in the film prior to buckling is released. This leads to the larger AE signals observed for the delaminations that spalled. In addition to the buckle driven indentations, nanoscratches were made on the Al interlayer samples. These scratches generated 1-D blisters. Strain energy release rates were calculated for all three tests with the results given in Table 5.2. The similarity between values for all three tests suggests the following: the calculation methods are self-consistent and the amount of aluminum at the interface doesn't impact the toughness in this case.

The interface that failed was identified using atomic force microscopy and Auger Electron Spectroscopy to be the aluminum-sapphire interface. As shown in Figure 28, a profile of the edge of a spalled double buckle region shows that the crack propagated along one plane, kinked up through approximately 150 nm of material, continued to propagate for a distance of approximately  $1 \mu\text{m}$ , and then kinked up through the remaining  $0.5 \mu\text{m}$  of material. This strongly suggests that the crack propagated along the aluminum-sapphire interface, and only kinked into the aluminum for a distance. It should be noted that much of the delamination edge did not show any evidence of aluminum, and only in the largest spallations were there failures such as the one shown here. The low values for interfacial toughness of aluminum-on-sapphire in this case were likely due to carbon contamination of the aluminum-sapphire interface.

#### **8.13.5.1.2 Silicon nitride**

Silicon nitride on silicon oxide is another hard film on brittle substrate system used in microelectronics where adhesion of the interface controls reliability. Recent work by Sanchez et al. (1999) have developed and applied cross-sectional nanoindentation in the study of interfacial fracture in this system. It is a quick test capable of producing controlled thin film delaminations and it provides direct observation of the interfacial

crack path in cross-section. The film system they studied was fabricated by chemical vapor depositing a 1  $\mu\text{m}$  thick layer silicon oxide onto a silicon substrate followed by chemical vapor deposition of a 1  $\mu\text{m}$  thick layer silicon nitride. Indentations are then made normal to the wafer cross-section using a diamond three-sided Berkovich indenter with one indenter side parallel to the interface of interest as shown in Figure 29. Delamination produced an excursion in the load-vs.-displacement curve clearly demarcating conditions for fracture. The tests gave fracture energies that ranged from 1.2 to 1.8 J/m<sup>2</sup>. The same film structure tested using the four-point bend technique gave a value of 1.65 J/m<sup>2</sup> in good agreement with cross-sectional indentation.

#### **8.13.5.1.2 Tungsten**

Sputtered tungsten is a hard film on rigid substrate also used in the microelectronics industry as a popular alternative to aluminum metallization (de Boer et al., 1997). However, it can exhibit poor adhesion especially when subjected to high tensile stresses from chemical vapor deposition which limits use. Several indentation-based tests have been developed to measure interfacial fracture energies of tungsten films.

The microwedge indentation technique was developed by de Boer and Gerberich (1996a,b) to determine the fracture energy of tungsten thin film fine lines on oxidized silicon substrates. Because tungsten is classically isotropic, Young's modulus is independent of grain texture. The thermally grown amorphous silicon oxide on the silicon substrate is elastically isotropic as well. The tests are easily conducted on a nanoindenter and the analysis is based on linear elastic fracture mechanics. The test samples were fabricated by rf-sputtering 800 nm of tungsten onto thermally oxidized silicon wafers coated in photoresist to create 5, 10, and 15  $\mu\text{m}$  wide lines. A sharp 20  $\mu\text{m}$  wide diamond microwedge with an included angle of 90° was used to indent the lines perpendicular to the line direction and trigger double-buckling and crack extension along the length of the lines. Using only unspalled buckles, the interfacial fracture energies were shown to range from 16 to 20 J/m<sup>2</sup>. This is somewhat higher than the fracture toughness the authors estimated for the tungsten-silicon oxide interface of 5 J/m<sup>2</sup> and can be attributed to cracking of the substrate during indentation testing.

To overcome these test method difficulties, de Boer and Gerberich (1996 a,b) developed a fracture mechanics based Precracked Line Scratch Test. It differs from conventional scratch tests because the crack tip is well removed from the indenter tip. In addition the tangential load is measured directly, the normal to tangential load ratio is near unity, and substrate cracking does not occur under the indenter. Tungsten line samples 10 and 15  $\mu\text{m}$  wide and 500 and 1500 nm thick were fabricated as in earlier work but with a thin carbon film over a portion of the substrate to act as a precrack. In these tests a 20  $\mu\text{m}$  wide diamond microwedge with an included angle of 30° was used to push against the 'precracked' ends of the fine lines with a displacement controlled IBM microindenter until the films buckled. When the precracks were short and the lines long, the cracks kinked into the interface. When the precracks were long, the cracks grew along the interface until they kinked into the film and the film spalled. These conditions provided lower and upper bounding interfacial fracture energies between 3.5 and 16 J/m<sup>2</sup>. When the precrack and line lengths were short, the cracks remained along the interface



giving an interfacial fracture energy of 7 J/m<sup>2</sup>.

More recently, Kriese et al. (1999b) used indentation fracture techniques to study interfacial fracture of thin tungsten films on silicon oxide substrates. The films were sputter deposited to a thickness of 530 nm. Wafer curvature showed that the films were deposited with tensile residual stresses ranging from 510 to 615 MPa. Onto these films, superlayers of tungsten or chromium were sputter deposited giving residual stresses that ranged from a 1.3 GPa residual tensile stress for a 500 nm thick chromium overlayer to a -1.1 GPa residual compressive stress for a 355 nm thick tungsten superlayer.

Nanoindentation with a 1  $\mu$ m root radius conical diamond tip was used to nucleate fracture. In all cases fracture occurred along the tungsten-silicon oxide interface with blisters forming a circular morphology. These are shown in Figure 30. The film with the compressive overlayer exhibited a smooth blister profile with no evidence of radial cracking. The films with tensile overlayers exhibited radial cracking that increased in severity with increasing tensile stress. Interfacial fracture energies were then determined using solutions for pinned circular blisters. The highest value was 15 J/m<sup>2</sup> for the sample with the compressive overlayer. The values decreased to 4.0 J/m<sup>2</sup> as the severity of radial cracking increased. These values are in very good agreement with values of 5 to 15 J/m<sup>2</sup> from previous work using different measurement techniques.

### **8.13.5.2 Ductile Metal Films**

#### **8.13.5.2.1 Copper films**

Semiconductor applications have seen a dramatic increase in importance with the emergence of copper as the next generation interconnect metallization material for ultra-large-scale integration (USLI) fabrication. As a result, Cu/dielectric adhesion is one of the main reliability issues. Unfortunately, copper exhibits poor adhesion to most dielectric substrates (Russell et al., 1995; Bagchi and Evans, 1996; Kriese et al., 1997; Chang, 1989; Chae et al., 1994; LaFontaine, 1990). Several methods have been developed to address this problem with annealing, alloying, and the interposing of a metallic interlayer to act as an adhesion promoter the most common (Russell, 1995). In particular, much attention has focused on the use of titanium and chromium as interlayers or alloying additions (Russell et al., 1995; LaFontaine, 1990). While the exact mechanisms by which these metals increase adhesion have yet to be fully explored, the empirical characteristics have been addressed in these studies. The following discussion shows how nanomechanical testing is being used to measure copper film adhesion, first in assessing adhesion of copper on SiO<sub>2</sub>/Si and then with the use of titanium and chromium adhesion layers.

Kriese and co-workers (1998a) looked at the use of stressed overlayers (superlayers) in measuring adhesion of thin copper films on oxide substrates. The films were sputter deposited onto silicon oxide substrates and divided into two groups. One group was left in the as-deposited condition while a tungsten overlayer was deposited on the other. Nanoindentation was then conducted on both groups of samples using a 90° conical indenter with a spherical tip radius of 1  $\mu$ m, driven at a rate of 600 mN/s.

The as-deposited copper films and the copper films with stressed overlayers delaminated forming large circular blisters during indentation testing as shown in Figure

31. However, there were differences. All indentation tests on copper with stressed overlayers produced a delamination while more than one-third of the copper-only tests formed the "ring" morphology, shown in the bottom row of Figure 31a, due to film pileup. The delaminations in the copper with stressed overlayer films were also significantly larger than in the copper only films.

Indentation load-displacement curves typically contained significant slope-changes or excursions indicative of delamination and fracture (Figure 32). These changes are much more pronounced for the copper with stressed overlayer films, as the tungsten exhibits prominent through-film cracking. Solutions for pinned circular blisters were then used to determine interfacial fracture energies. These energies were independent of film system and fell predominately within the same range of adhesion energies, namely 0.2 to 2 J/m<sup>2</sup>. The copper with stressed overlayers did have less variation and an upper limit of 1 J/m<sup>2</sup>. This compares favorably with recent measurements by Bagchi et al. (1994) and Bagchi and Evans (1996) of 0.4 to 0.8 J/m<sup>2</sup> for vacuum evaporated copper films and with measurements by Oh et al. (1988) who report a range of 1 to 10 J/m<sup>2</sup> for a copper/glass system using a double cantilever beam macroscopic specimen (Charalambides et al., 1989).

Kriese and co-workers (1998a) note that an especially encouraging aspect of their work is that the use of a stressed overlayer promotes delamination with indentation, allowing calculation of adhesion energy. With regard to the copper films, the result was dramatic, in that occurrence of delamination was far more consistent with a stressed overlayer. In addition, use of stressed overlayers decreased experimental error and appeared to give a more reliable estimate of the adhesion energy. What is especially interesting is that the films exhibit the same range of interfacial toughness if one ignores the higher copper-only values where film thickness leads to significant crack tip plasticity. This then supports the idea that the tungsten overlayer does not fundamentally change the mechanisms associated with the delamination of as- sputtered copper films, and further, that these mechanisms are independent of film thickness.

#### ***8.13.5.2.1.1 Annealing effects***

Annealing is commonly used to promote adhesion and performance of thin films with its effects often ascribed to its influence on the diffusion of segregants and changes in the nature of the interface. It also affects plasticity in the process zone by changing yield properties. Kriese et al. (1998a) studied the effects of annealing on copper film adhesion using sputter deposited films that ranged in thickness from 200 to 1000 nm. The films were divided into two groups with one group left in the as-deposited condition while the other group was annealed at 600°C for 2 hours in an argon atmosphere. A stressed overlayer was then deposited on all samples and followed by nanoindentation using a conical indenter with a spherical tip to trigger delamination. The results are shown in Figure 33 as a function of film thickness and annealed state. The trend lines are smooth fits to the data, and do not represent any specific modeling prediction. While in several cases there is overlap, it is clear that both thickness and annealing increase adhesion with the effect of annealing being more pronounced at greater thickness.

#### **8.13.5.2.1.2 Interlayer effects**

Kriese et al. (1998a) then addressed the effects of metallic interlayers on copper film adhesion. They deposited three sets of copper films to thicknesses of 420 to 450 nm and 1100 to 1170 nm. The as-deposited residual tensile stress in all films ranged from 195 to 275 MPa. The magnitude and sign of stress is comparable to the thermal mismatch stress induced as the wafer cools from deposition to room temperature. Films of each thickness were deposited onto bare SiO<sub>2</sub>/Si wafers while two other sets of films were deposited with 7-10 nm of titanium and chromium interlayers, respectively, prior to deposition of the copper. All copper films were then deposited simultaneously on the substrates followed by deposition of a 590 to 680 nm thick tungsten superlayer. The residual stresses in the tungsten superlayers were compressive, and ranged from 95 to 345 MPa, with no clear trends of any sort.

Figure 34 clearly shows a strong effect of the interlayer on load-displacement curves for 95 mN load indents into 1100 nm thick films. This effect is indicative of the effect interlayers, and more specifically increases in adhesion, have on film properties. The corresponding fracture energies are shown in Figure 35 as a function of interlayer composition and film thickness. There appears to be no appreciable effect of thickness in the absence of an interlayer. However, the two sets of films had been prepared at different operating parameters of the sputtering chamber, and are expected to have different microstructures and hence different adhesion. The notable result in Figure 35 is the strong increase in adhesion energy for films with Ti and Cr interlayers. The presence of an interlayer increases adhesion energy from 1.3 to 7.5 times depending on the composition of the interlayer and thickness of copper film. Moreover, the effect of the interlayer becomes more pronounced at greater thickness. These quantitative trends corroborate the semi-quantitative results previously reported (Russell et al., 1995; LaFontaine et al., 1990). The increase in adhesion with increasing thickness has been reported by Evans and Dalgleish (1991) and Venkataraman et al. (1996).

#### **8.13.5.2.1.3 Film thickness effects**

Recent work by Volinsky et al. (2000) systematically studied the effect of film thickness over two orders of magnitude on a single Cu/SiO<sub>2</sub> system. Copper films of eight thicknesses between 40 nm and 3  $\mu$ m were sputter deposited on top of oxidized Si wafers with and without a 10 nm thick Ti adhesion-promoting layer. All films were passivated with a 1  $\mu$ m thick layer of W for adhesion measurements. Nanoindentation using a 1  $\mu$ m radius conical diamond indenter was used to nucleate fracture. This study showed that a 40 to 3000 nm variation in thickness increased measured fracture energies from approximately 0.6 to 100 J/m<sup>2</sup> (Figure 36). Also shown is an upper bound from a previous study (Volinsky et al., 1999) and a dislocation free zone model (Zielinski et al., 1992; Volinsky et al., 2002b). Fracture energies for films less than 100 nm thick exhibited a nearly uniform lower limiting value of 0.8 J/m<sup>2</sup>. The value corresponds to the thermodynamic work of adhesion of Cu to SiO<sub>2</sub> measured by the contact angle technique (Furuya et al., 1995). This means that for films less than 100 nm thick there is almost no plastic deformation at the crack tip (Volinsky et al., 1999; Tymiak et al., 2000). For

thicker films there is a definite contribution of crack tip plastic deformation ( $U_f$ ) to the practical work of adhesion ( $W_p$ ), which scales with the film thickness. In that same series of studies, the interfacial fracture energies could be increased by about a factor of three using a 10 nm thick innerlayer of titanium (Tymiak et al., 2000; Gerberich et al., 2000; Volinsky et al., 1999). However, in these films fracture occurred along the Ti/Cu interface with fracture energies substantially greater than for the copper only film fractures. In a similar type of study using four-point bend tests, Lane et al. (2000) also demonstrated an increase in toughness as thickness increased from 30 to 10,500 nm. Here a thin innerlayer of TaN/Ta was utilized to improve adhesion so that the lower limit for the thinner films gave values of about 5 J/m<sup>2</sup>.

#### ***8.13.5.2.1.4 Temperature effects***

The effect of test temperature on fracture energy was recently addressed by Volinsky et al. (2000b) in a study of copper films. Copper films were sputter deposited onto oxidized silicon substrates to thicknesses of 80 and 500 nm. A tungsten overlayer was then deposited to uniformly stress the films. A range of test temperatures from 80 to 130°C was utilized to evaluate temperature effects on fracture energy. For this purpose, a resistance heating stage from Digital Instruments (Volinsky, 2000b; Gerberich et al., 2000) was used in conjunction with the Nanoindenter II. With a sample glued to a puck using thermoepony, this assembly was then clamped onto the top of the microheater with the thermocouple sample clamp. The heating element is thermally isolated from the surrounding atmosphere as the sample is the only surface that conducts heat into the atmosphere. Since the loads used were relatively high (up to 600 mN), operation of the Nanoindenter II was not disturbed with the presence of a heater. Indentation testing with a 1  $\mu$ m radius conical diamond indenter was used to nucleate fracture in all samples as a function of test temperature. Tests were also run at room temperature prior to and after conducting temperature indentation experiments to ensure that there were no annealing effects on sample behavior. In the case of the dense tungsten superlayer, passivated copper did not form an oxide during elevated temperature testing. As is shown in Figure 37, fracture resistance increased by a factor of four for the thinner film while for the thicker film it increased by more than an order of magnitude. This brittle-to-ductile transition in a normally low adhesion interface of Cu/SiO<sub>2</sub> with the same Cu thickness and the same bond strength eliminated variables other than the yield strength as possible sources of increased toughening.

#### ***8.13.5.2.2 Gold films***

Adhesion is a critical factor in controlling the performance and reliability of gold-chromium hybrid microcircuits (Mattox, 1973; Mittal, 1976). Though superceded by other designs and materials, there are circuits of this type still in use. These circuits consist of an alumina substrate, a thin chromium layer for adherence, and a gold layer for conductance to connect components on the microcircuit (Rairden et al., 1971; Thomas and Haas, 1972; Munitz and Korem, 1976). A gold-coated copper lead is thermomechanically bonded onto a gold pad layer to complete the connection. During post deposition annealing, lead-frame bonding and service at elevated temperature,

diffusion and segregation of chromium and copper changes the composition and structure of the films and interfaces (Rairden et al., 1971; Thomas and Haas, 1972; Munitz and Korem, 1976; George et al., 1990; Munitz and Korem, 1980). Although chromium and copper diffusion and segregation are critical issues in long-term durability of devices with these films, the effects of these processes on film adhesion are not well defined (Moody et al., 1998; Kriese et al., 1998a; Kriese et al., 1999a).

Until recently, gold films have been almost exclusively studied as diffusion bonded sandwich layers between sapphire slabs (Jensen et al., 1990; Reimanis et al., 1990; Reimanis et al., 1991; Evans and Dalgleish, 1992; Mao and Evans, 1997). Lipkin et al. (1998) and Turner and Evans (1996) used double-cleavage-drilled compression test samples similar to the Brazil disk test loaded along the crack line. While tests did not address fracture and adhesion with a methodical study of thickness variations data shows a two order of magnitude decrease in toughness ( $1.4\text{--}150\text{ J/m}^2$ ) over a two order of magnitude decrease in thickness.

Recent work has begun addressing adhesion of submicron thick gold films (Moody et al., 2000). These films were sputter deposited onto sapphire substrates at thicknesses down to 10 nm. The weak gold to substrate bonds and soft films necessitated testing these films in as-deposited configurations using stressed overlayers which apply a uniform stress to the ductile films while constraining out-of-plane plasticity (Bagchi et al., 1994; Bagchi and Evans, 1996; He et al., 1996). The deposition of these overlayers triggered formation of classic telephone cord blisters in all sputter deposited gold films as shown in Figure 38. There is a point between each turn in the blister where the blister becomes uniform in shape. The morphology of the blister at this point provides the data from which interfacial fracture energies were obtained using solutions for film systems where residual stresses dominate fracture behavior.

Fracture energies were determined using mechanics-based models (Hutchinson and Suo, 1992; Marshall and Evans, 1984; Evans and Hutchinson, 1984) modified for bilayer films (Bagchi et al., 1994; Bagchi and Evans, 1996; Kriese et al., 1999a,b). Corresponding mode I contributions were then determined using empirical relationships based on calculated phase angles of loading (Hutchinson and Suo, 1992; Thouless et al., 1992). Figure 39 shows that the measured values decreased to a lower limiting value at thicknesses less than 100 nm with corresponding mode I values of  $0.5\text{ J/m}^2$ . These values are similar to the true works of adhesion for gold on aluminum oxide (Reimanis et al., 1990). The full range of measured values from all studies are given in Figure 40 and clearly show the marked effect film thickness has on interfacial fracture energies.

#### **8.13.5.2.2.1 Gold-chromium bilayer films**

Poor adhesion of gold to all oxide substrates has led to the use of adhesion layers. One of the first metals used for this purpose was chromium. However, chromium diffusion and depletion raised significant concerns for long term performance of gold film devices. This has been addressed in recent studies of chromium diffusion effects on adhesion for hybrid microcircuit applications (Moody et al., 2000; Moody et al., 2003). The samples were prepared by sputter deposition of a 6 nm thick chromium adhesion layer onto sapphire substrates followed by sputter deposition of 200 nm of gold film. One group of films was left in the as-deposited condition. A second group was heated at

400°C for 2 hours in air at which point chromium had begun to come off the sapphire interface in many regions. The third group was then heated at 400°C for 8 hours in air after which all the chromium had migrated off the interface. Stressed overlayers were then deposited to uniformly stress the films. Unlike the gold on sapphire films, the stresses were not sufficient to trigger delamination and buckling which necessitated the use of nanoindentation to trigger film failure.

The mode I fracture energies are plotted in Figure 41 as a function of blister size. The fracture energies for the gold-chromium films on sapphire are two times greater than for pure gold clearly demonstrating the better adhesion properties of chromium interlayers. All energies are significantly higher than for gold on sapphire. The fracture energies increase for samples where the chromium interlayer is reduced in size but is consistent with the effects of annealing on film adhesion observed in other systems. Complete depletion of the chromium adhesive layer led to a marked increase in fracture energies. In addition, the fracture path changed from along the film-substrate interface to mixed mode of fracture along the overlayer-gold film interface, in the gold film, and along the gold substrate interface. Diffusion has replaced the thin hard chromium adhesive layer with a solid solution of gold and chromium in the lattice and enhanced concentrations of chromium along the gold grain boundaries.

Figure 42 presents the fracture energies as a function of blister diameter normalized with respect to indentation diameter at the point of the last excursion. Plotting data in this manner shows that the large increase in fracture energy at the small blister sizes results from crack tip plastic zone interactions with the plastic zone created under the indenter (Volinsky et al., 1999, 2002). It also reveals two trends in behavior that depend on the fracture path. When fracture occurs cleanly along the substrate interface, there is much less interaction between crack tip and indenter plastic zones than when fracture occurs through the gold film and along the overlayer-gold film interface. This parallels the relationship between fracture energies and failure modes Volinsky et al. (2002b) observed in low-k dielectric films and supports the conclusion that plastic zone interactions have a strong effect on measured fracture energies even for relatively large blisters. At very large blister sizes, the lower limit represents values where crack tip-indenter interactions no longer have a significant effect on measured fracture energies.

Table 3 shows that as-deposited film indentation fracture energies are slightly higher than values obtained from telephone blisters on the same film. This is consistent with the observation that the portion of the as-deposited film, which did not exhibit telephone cord blistering is more strongly adhered to the substrate. Fracture energies measured in the partially annealed film were similar, as expected for a continuous chromium interlayer. When fully annealed, the average fracture energy increased dramatically. This increase can be attributed to a change in fracture path from along the substrate interface to a mixed mode of fractures along the overlayer-gold interface, within the gold, and in isolated instances along the substrate interface.

Following indentation testing, nanoscratch tests were used to force fracture occur along the substrate interface in the fully annealed samples. Under these conditions, the fracture energies in fully annealed samples equaled values measured in partially annealed films, even though the film systems had markedly different compositions and structures. The partially annealed films had a continuous chromium adhesive layer between the gold and sapphire substrate whereas diffusion had reduced the fully annealed films to a solid

solution of gold and chromium. There were no reactions between film and substrate at these temperatures or in samples held at high temperatures for much longer times (Moody et al., 1999; Moody et al., 2003; Zhao et al., 1986). As a result, the increase in fracture resistance following annealing appears attributable to the effects of interfacial structure on deformation and fracture. These results clearly show that chromium in solution is as effective in promoting adhesion as continuous chromium adhesive layers. The impact on hybrid microcircuits service life is dramatic as the film adhesion and device performance do not degrade as long as chromium remains in solution along the substrate interface.

#### **8.13.5.2.2.2 Gold-copper bilayer films**

The effect of copper migration on film durability in hybrid microcircuits has recently been studied using laboratory samples and accelerated aging (Moody et al., 2002). Steady state copper migration was simulated using a Au<sub>2</sub>W/oCu target to sputter deposit a 200 nm thick gold alloy film. Long term effects, where segregation leads to a continuous copper layer at the gold substrate interface, were simulated by sputter depositing a 6 nm thick layer of copper onto a sapphire substrate followed by a 200 nm thick layer of gold. An 840 nm thick tungsten overlayer was then sputter deposited onto these films. This layer triggered extensive blistering in the Au-Cu film while additional stresses from nanoindentation were required to trigger delamination and buckling in the Au<sub>2</sub>W/oCu film. In all cases, fracture occurred along the film-substrate interfaces with no evidence of gold or copper left on the sapphire substrates. The blisters are shown in Figure 43.

The uniform width blister analysis was used to determine fracture energies from the telephone cord blisters in the Au-Cu film and the circular blister analysis was used to determine fracture energies from indentation-induced blisters in the Au<sub>2</sub>W/oCu alloy. The measured fracture energies are given in Table 5.3 along with material properties. The data in Table 5.2 suggests that the higher fracture energy measured for the Au<sub>2</sub>W/oCu films on sapphire was due to solid solution hardening effects on deformation. These results are consistent with the conclusions of Volinsky and coworkers (1999) that deformation makes a significant contribution to measured fracture energies in 200-nm-thick films.

#### **8.13.5.2.3 Aluminum films**

Most aluminum thin film adhesion data (Xu et al., 1999; Dauskardt et al., 1998; Schneider et al., 1998; Bahr et al., 1997; Gerberich et al., 2000) have been generated using either superlayer indentation (Kriese et al., 1999a,b) or the four-point bend UCSB test (Charalambides et al., 1989; Hofinger et al. 1998; Dauskardt et al., 1998; Becker et al., 1997). In all cases, the substrates were either silicon with SiO<sub>2</sub> between the silicon and deposition layer(s) or sapphire. For the superlayer indentation tests, either W or Ta<sub>2</sub>N superlayers approximately 1  $\mu$ m thick were used incorporating a residual stress on the order of 1 GPa compression or 100 MPa tension. Within the data scatter, a small effect of residual stress was found on the resulting adhesion measurements. Three types of interfaces were evaluated, a direct deposit of aluminum, one with 40 nm of carbon as an

interlayer, and one with 40 nm of copper as an interlayer (Gerberich et al., 2000). The latter two were known to provide lower adhesion. For 500 nm thick films these provided fracture energy values of 8.0, 0.65 and 0.6 J/m<sup>2</sup>. These results are consistent with values determined by Schneider et al. (1998) using the same type of test but with a Ta superlayer and 500 nm of aluminum on Al<sub>2</sub>O<sub>3</sub>. Here, with and without carbon as a contaminant, the toughness was 5.6 and 1.05 J/m<sup>2</sup>. Another consistent result, was found by Dauskardt et al. (1998) on Al-Cu depositions with a 120 nm thick TiN/Ti/TiN innerlayer. For a 500 nm film their interpolated value would be 8.5 J/m<sup>2</sup>. In another study using a thinner 70 nm TiN/Ti/TiN innerlayer, Xu et al. (1999) found the TiN/SiO<sub>2</sub> interface failure energy to be on the order of 1.9 J/m<sup>2</sup> in the absence of humidity effects. Irrespective of whether the substrate is SiO<sub>2</sub>/Si or Al<sub>2</sub>O<sub>3</sub>, or the presence of a strong interlayer, there is a consistent increase in fracture resistance from about 4 to 12 J/m<sup>2</sup> with an order of magnitude increase in thickness from 200 to 2000 nm. It appears then that for strong interfaces, the measured strain energy release rate is dominated by the aluminum thickness in Al/X<sub>i</sub>/SiO<sub>2</sub> or Al/X<sub>i</sub>/Al<sub>2</sub>O<sub>3</sub> systems as long as all X<sub>i</sub> innerlayers are reasonably thin. Note that this would apply equally to Al or Al-Cu films.

### 8.13.6 SUMMARY

In general, it is clear that nanomechanical test techniques are useful for quantifying the adhesion of thin films. It is equally clear that each technique requires further work, both experimentally and theoretically. The primary technique, nanoindentation, is the simplest to conduct and is quite robust, and the use of a stiff superlayer appears especially promising. However, it does have experimental difficulties associated with assessment of indentation-induced stress and the occurrence of non-interfacial phenomena such as spallation and radial cracking. The scratch technique is also simple to conduct, but lacks theoretical rigor. Finally, the line-scratch technique seems promising, but is more difficult in terms of sample preparation, both to manufacture the lines and insert a precrack.

Nanoindentation based methods of film adhesion suffer from many of the problems of film adhesion measurements, namely that separating the thermodynamic work of adhesion from a practical work of adhesion (which includes additional effects such as plastic deformation in films, post-cracking interactions between the film and substrate, and cracking in either the film or substrate) is challenging. Several thin film or interfacial adhesion tests have been reviewed with emphasis toward ductile, thin metallic films. In addition, single and multilayer films on silicon or alumina substrates are reviewed to show how variations in thickness, chemistry and temperature affect adhesion. Major roles are shown for thickness, test temperature and interface chemistry as to how they affect yield strength and the thermodynamic work of adhesion. For copper, gold, and aluminum any one of these variables are shown to change the practical work of adhesion by an order of magnitude or more. For thin films, fracture energies asymptotically approach the thermodynamic work of adhesion with decreasing film thickness while for thick samples plastic energy dissipation controls fracture energy. It is shown that resistance-based models need yield strength, a failure criterion and at least one length scale for predictive quality.

Realistically, the implementation of these nanoindentation based adhesion tests is



likely to continue in the near future, given the relative simplicity of performing the test. This is very similar to the developments in nanoindentation, which has become a dominant method of measuring the mechanical properties of thin films, in spite of the difficulties in analyzing the deformation relationships between films and substrates. The ease of sample fabrication, the ability to perform tests on films under the same processing conditions as the actual devices (no additional processing steps are needed) and the well documented testing methods make nanoindentation more common than methods such as micromachined tensile testing or bulge testing. There are competing adhesion testing methods, such as four point bending, and cantilevered beams, but in most cases these involve additional processing steps beyond that of film deposition, and can be challenging to test unique substrates or small samples. It is likely, therefore, that continued research into the mechanics of buckling and fracture in thin films induced by nanoindentation will be required. In general, nanomechanical test techniques are useful for quantifying the adhesion of thin films.

Clear trends of increasing practical works of adhesion with increasing thickness, annealing and the presence of titanium and chromium interlayers were exhibited. This corroborated previous semi-quantitative studies of similar films. While non-negligible variance was exhibited in the calculated adhesions, the magnitudes and trends of the measured adhesion energy are comparable between many studies. Further, by measuring the adhesion in terms of the energy dissipation required for delamination, not only can the incremental effects of process optimization be assessed, but the relationships between film microstructure and material micromechanisms can be investigated and modeled. Increases in testing temperature were demonstrated to increase the practical work of adhesion of metal films. Even larger increases in fracture resistance may be obtained by increasing ductile film thicknesses.

Several comments are in order regarding the effects of residual stresses in these thin films. As pointed out at the end of the superlayer test discussion, the residual stress is taken into account for buckled films. For the four-point bend test, it is considered that the residual stress is a second order effect on the driving force side of the equation. Such an effect might be a change in the local curvature and hence the mode mixity. On the other hand, a residual stress clearly could change the yield criterion and plastic zone size at a crack tip affecting the resistance size of the equation.

Probably the most important issue to consider when utilizing nanoindentation based adhesion testing is that these tests are almost always under a mixed mode loading condition. The use of superlayers, which is required for some films to delaminate, often adds to the shear components of loading. Therefore, plasticity in the films (related directly to the hardness of the films) will often be exasperated when the shear component of loading is increased. Mismatches in the elastic moduli of the films will also impact this value. This change in phase angle will undoubtedly lead to difficulty, in some cases, for determining the work of adhesion for a true mode I condition. However, by judicious selection of combinations of the stresses and thicknesses of stressed superlayers, it should be possible to probe a selection of phase angles, which should aid in determining the mode I fracture criteria. In general, minimizing the interactions between the tip doing the indentation and the position at which the interfacial crack arrests will lead to increasing accurate values of film adhesion.

In conclusion, nanoindentation testing to determine the interfacial fracture toughness of thin film – substrate systems has been shown to be a valid testing method to relatively easily probe the effects of interfacial chemistry, film thickness, yield strength, and testing temperature on film adhesion. While work is still needed to fully develop the effects of mixed mode loading and develop experimental methods of accessing various loading conditions, indentation and scratching will continue to play a very significant role in the assessment and study of interfacial fracture.

## ACKNOWLEDGMENTS

The authors gratefully acknowledge the technical assistance, review, and helpful comments of Megan Cordill, Washington State University. We thank John Jungk and William Mook, University of Minnesota, and James Lucas, Michigan State University, for their reviews and helpful comments. NRM and DFB also acknowledge the support of the U.S. DOE through Contract DE-AC04-94AL85000.

## REFERENCES

- J. R. Adams, D. K. Kramer, A study of the oxidation of tantalum nitride by ellipsometry and auger electron spectroscopy, *Surface Science* , 1976, **56**, 482-487.
- A.R. Akisanya, N.A. Fleck, The edge cracking and decohesion of thin films, *Int. J. Sol. Struc.*, 1994, **31**, 3175-3199.
- M. G. Allen, S. D. Senturia, Analysis of critical debonding pressures of stressed thin films in the blister test, *J. Adhesion*, 1988, **25**, 303-315.
- M. G. Allen, S. D. Senturia, Application of the island blister test for thin film adhesion measurement, *J. Adhesion*, 1989, **29**, 219-231.
- A.G. Atkins and D. Tabor, Plastic indentation in metals with cones, *J. Mech. Phys. Solids*, 1965, **13**, 149-164.
- C. Atkinson, R. Smelser, J. Sanchez, Combined mode fracture via the cracked Brazilian disk test, *Int. J. Fract.*, 1982, **18**, 279-291.
- C. L. Au, W. A. Anderson, D. A. Schmitz, J. C. Flassayer, F. M. Collins, Stability of tantalum nitride thin film resistors, *J. Mater. Res*, 1990, **5**, 1224-1232.
- F. Auerbach, "Smithsonian Report for 1891," Government Printing Office, Washington, 1893, pp. 207-236.
- A. Bagchi, G. E. Lucas, Z. Suo, A. G. Evans, A new procedure for measuring the decohesion energy for thin ductile films on substrates, *J. Mater. Res.*, 1994, **9**, 1734-1741.

- A. Bagchi, A. Evans, Thin film decohesion and its measurement, in "Mechanical Behavior of Diamond and Other Forms of Carbon," eds. M. D. Drory, M. S. Donley, D. Bogoy, J. E. Field, Materials Research Society, Pittsburgh, PA, 1995, vol. 383, pp. 183-197.
- A. Bagchi, A. G. Evans, Measurements of the debond energy for thin metallization lines on dielectrics, *Thin Solid Films*, 1996, **286**, 203-212.
- D. F. Bahr, W. W. Gerberich, Effect of in- and out-plane stresses during indentation of diamond films on metal substrates, in "Thin Films-Stresses and Mechanical Properties VI," eds. W. W. Gerberich, H. Gao, J.-E. Sundgren, and S. P. Baker, Materials research Society, Pittsburgh, 1996a, vol. 436, pp. 85-90.
- D.F. Bahr and W.W. Gerberich, Plastic zone and pileup around large indentations. *Metall. Mater. Trans.*, 1996b, **27A**, 3793-3800.
- D.F. Bahr, J.W. Hoehn, N.R. Moody, and W.W. Gerberich, Adhesion and acoustic emission analysis of failures in nitride films with a metal interlayer, *Acta Mater.*, 1997, **45**, 5163-5175.
- D. F. Bahr, W. W. Gerberich, Relationships between acoustic emission signals and physical phenomena during indentation, *J. Mater. Res.*, 1998, **13**, 1065-1074.
- S.P. Baker, W.D. Nix, Mechanical properties of compositionally modulated Au-Ni thin films: nanoindentation and microcantilever deflection experiments, *J. Mater. Res.* 1994, **9**, 3131-3144.
- T. L. Becker Jr., J. M. McNaney, R. M. Cannon, R. O. Ritchie, Limitations of the use of mixed mode delaminating beam specimen: effects of the size of the region of K-dominance, *Mechanics of Materials*, 1997, **25**, 291-308.
- M.R. Begley, D.R. Mumm, A.G. Evans and J.W. Hutchinson, Analysis of a wedge impression test for measuring the interface toughness between films/coatings and ductile substrates, *Acta Mater.*, 2000, **48**, 3211-3220.
- P. Benjamin, C. Weaver, Measurement of adhesion on thin films, *Proc. Roy. Soc. London*, 1960, **A 254**, 163-176.
- J.A. Brinell, Brinell's method of determining hardness and their properties of iron and steel, "II. Cong. Int. Methodes d'Essai, Paris," translated to English by A. Wahlberg, *J. Iron Steel Inst.*, 1901, **59**, 243-298.
- P. Burnett, D. Rickersby, The relationship between hardness and scratch adhesion, *Thin Solid Films*, 1987, **154**, 403-416.

- R. M. Cannon, B. J. Dalgleish, R. K. Dauskardt, T. S. Oh, R. O. Ritchie, Cyclic fatigue-crack propagation along ceramic/metal interfaces, *Acta Metall. Mater.*, **39**, 1991, 2145-2156.
- H. C. Cao, A. G. Evans, An experimental study of the fracture resistance of bimaterial interfaces, *Mechanics of Materials*, 1989, **7**, 295-304.
- P. G. Charalambides, J. Lund, A. G. Evans, and R. M. McMeeking, A test specimen for determining the fracture resistance of bimaterial interfaces, *J. Appl. Mech.*, 1989, **111**, 77-82.
- C.-A. Chang, High temperature interaction studies of C/Cu/SiO<sub>2</sub>/Si and related structures, *J. Appl. Phys.*, 1989, **66**, 1163-1169.
- K.H. Chae, H.G. Jang, I.S. Choi, S.M. Jung, K.S. Kim, S.S. Kim, C.N. Whang, Mechanism of adhesion improvement in ion-beam mixed Cu/CiO<sub>2</sub>, *J. Mater. Sci.*, 1994, **29**, 749 –753.
- S. S. Chiang, D. B. Marshall, A. G. Evans, A simple method for adhesion measurements, in "Surfaces and Interfaces in Ceramic and Ceramic-Metal Systems," eds. J. Parks, A.G. Evans, Plenum Press, New York, 1981, pp. 603-617.
- R. H. Dauskardt, M. Lane, Q. Ma, N.Krishna, Adhesion and debonding of multilayer film structures, *Engng. Fract. Mech.*, 1998, **61**, 141-162.
- M. P. de Boer, W. W. Gerberich, Microwedge indentation of the thin film fine line. I. Mechanics. *Acta Mater.*, 1996a, **44**, 3169-3175.
- M. P. de Boer, W. W. Gerberich, Microwedge indentation of the thin film fine line. II. experiment, *Acta Mater.*, 1996b, **44**, 3177-3187.
- M. P. de Boer, M. Kriese, W. W. Gerberich, Investigation of a new fracture mechanics specimen for thin film adhesion measurement, *J. Mater Res.*, **12**, 1997, 2673-2685.
- M.F. Doerner, W.D. Nix, A method for interpreting the data from depth-sensing indentation instruments, *J. Mater. Res.*, 1986, **1**, 601-609.
- M. F. Doerner, W. D. Nix, Stresses and deformation processes in thin films on substrates, in "CRC Critical Reviews in Solid State and Materials Science," 1988, vol. 14, pp. 225-268.
- M.D. Drory and J.W. Hutchinson, Measurement of the adhesion of a brittle film on a ductile substrate by indentation, *Proc. R. Soc. Lond. A.*, 1996, **452**, 2319-2341.
- J. Dundurs, Edge-bonded dissimilar orthogonal elastic wedges under normal and shear loading, *J. Appl. Mech.*, 1969, **36**, 650-652.

- A. G. Evans, J. W. Hutchinson, On the mechanics of delamination and spalling in compressed films, *Int. J. Solids Structures*, 1984, **20**, 455-466.
- A. G. Evans, M. D. Drory, M. S. Hu, The cracking and decohesion of thin films, *J. Mater. Res.*, 1988, **3**, 1043-1049.
- A. G. Evans, M. Ruhle, Microstructure and fracture resistance of metal/ceramic interfaces, *MRS Bulletin*, 1990, **XV**, 1990, 46-50.
- A. G. Evans, M. Rühle, B. J. Dalgleish, and P. G. Charalambides, The fracture energy of bimaterial interfaces, *Mater. Sci. Eng.*, 1990, **A126**, 53-64.
- A. G. Evans, B. J. Dalgleish, The fracture resistance of metal-ceramic interfaces, *Acta Metall. Mater.*, 1992, **40**, S295-S306.
- A.G. Evans, B.J. Dalgleish, The fracture resistance of metal-ceramic interfaces, *Mater. Sci. Eng.*, 1993, **A162**, 1-13.
- A. G. Evans, J. W. Hutchinson, Overview on thermomechanical integrity of thin films and multilayers, *Acta Metall. Mater.*, 1995, **43**, 2507-30.
- A. G. Evans, J. W. Hutchinson, Y. Wei, Interface adhesion: effects of plasticity and segregation, *Acta Mater.*, 1999, **47**, 4093-4113.
- N. A. Fleck, J. W. Hutchinson, Phenomenological theory for strain gradient effects in plasticity, *J. Mech. Phys. Solids*, 1993, **41**, 1825-1857.
- A. Furuya, N. Hosoi, Y. Ohishita, Evaluation of Cu adhesive energy on barrier metals by means of contact-angle measurement, *J. Appl. Phys.*, 1995, **78**, 5989-5992.
- M. A. George, W. S. Glaunsinger, T. Thundat, S. M. Lindsay, Electrical, spectroscopic, and morphological investigation of chromium diffusion through gold films, *Thin Solid Films*, 1990, **189**, 59-72.
- W. W. Gerberich, A. A. Volinsky, N. I. Tymiak, N. R. Moody, A ductile to brittle transition (DBTT) in adhered thin films, in "Thin Films-Stresses and Mechanical Properties VIII," eds. R. Vinci, O. Kraft, N. Moody, P. Besser, E. Schaffer II, Materials Research Society, Pittsburgh, PA, 2000, vol. 594, pp. 351-364.
- A.A. Griffith, The phenomena of rupture and flow in solids, *Phil. Trans. R. Soc. Lond.*, 1920, **A221**, 163-198.
- J. C. Hay, G. M. Pharr, Experimental investigations of the Sneddon solution and an improved solution for the analysis of nanoindentation data, in "Fundamentals of Nanoindentation and Nanotribology," eds. N. R. Moody, W. W. Gerberich, N. Burnham, S. P. Baker, Research Society, Pittsburgh, PA, 1998, vol. 522, pp. 39-44.

- M. Y. He, M. R. Turner, A. G. Evans, Analysis of the double cleavage drilled compression specimen for interface fracture energy measurements over a range of mode mixities, *Acta Metall. Mater.*, **43**, 1995, 3453-3458.
- M. Y. He, A. G. Evans, and J. W. Hutchinson, Interface cracking phenomena in constrained metal layers, *Acta Mater.*, 1996, **44**, 2963-2971.
- H. Hertz, "Miscellaneous Papers by Heinrich Hertz," ed. D.E. Jones and G.A. Schott, Macmillan, London, 1896, pp. 163-183.
- I. Hofinger, M. Oechsner, H. Bahr, M. Swain, Modified four-point bending specimen for determining the interface fracture energy for thin, brittle layers, *Int. J. Fract.*, 1998, **92**, 213-220.
- R. Hohlfelder, H. Luo, J. Vlassak, C. Chidsey, W. Nix, Measuring interfacial fracture toughness with the blister test, in "Thin Films: Stresses and Mechanical Properties VI," eds. W. W. Gerberich, H. Gao, J-E. Sundgren, S. P. Baker, Materials Research Society, Pittsburgh, PA, 1997, vol. 436, pp. 115-120.
- T. Hong, J.R. Smith, and D.J. Srolovitz, Theory of metal-ceramic adhesion, *Acta Metall Mater.*, 1995, **43**, 2721-2730.
- S.L. Hoyt, The ball indentation hardness test, *Trans. Am. Soc. Steel Treating*, 1924, **6** 396-420.
- H. Huang, W. W. Gerberich, Crack tip dislocation emission arrangements for equilibrium-II. Comparisons to analytic and computer simulation models, *Acta Metall. Mater.*, 1992, **40**, 2873-2882.
- Y. Huang, C. Liu, and G. Stout, Brazilian disk for measuring fracture toughness or orthotropic materials, *Acta Mater.*, 1996, **44**, 1223-1232.
- J. W. Hutchinson, Z. Suo, Mixed mode cracking in layered materials, in "Advances in Applied Mechanics," eds. J. W. Hutchinson, T. Y. Wu, Academic Press Inc., New York, 1992, vol. 29, pp. 63-191.
- J. W. Hutchinson, A. G. Evans, Mechanics of materials: top down approaches to fracture, *Acta Mater.*, **48**, 2000, 125-135.
- H. M. Jensen, The blister test for interface toughness measurement, *Eng. Frac. Mech.*, 1991, **40**, 475-486.
- H. M. Jensen, J.W. Hutchinson, K.-S. Kim, Decohesion of a cut prestressed film on a substrate, *Int. J. Solids Struct.*, 1990, **26**, 1099-1114.

- H. M. Jensen, M. D. Thouless, Effects of residual stresses in the blister test, *Int. J. Solids Struct.*, **30**, 1993, 779-795.
- K.L. Johnson, The correlation of indentation experiments. *J. Mech. Phys. Solids*, 1970, **18**, 115-126.
- K.L. Johnson, "Contact Mechanics," Cambridge Press, Cambridge, 1985.
- M.L. Jokl, V. Vitek, C.J. McMahon, Microscopic theory of brittle fracture in deformable solids: a relation between ideal work to fracture and plastic work, *Acta Metall.*, 1980, **28**, 1479-1488.
- M. F. Kanninen, Augmented double cantilever beam model for studying crack propagation and arrest. *Int. J. Fract.* 1973, **9**, 83-92.
- R. B. King, Elastic analysis of some punch problems for a layered medium, *Int. J. Solids Struct.* 1987, **23**, 1657-1664.
- E. Klokholm, Effects of stress on the physical properties of thin films, *J. Vac. Sci. Technol.* , 1971, **8** , 148-151.
- D. Kramer, H. Huang, M. Kriese, J. Robach, J. Nelson, A. Wright, D. Bahr, W.W. Gerberich, Yield strength predictions from the plastic zone around nanocontacts, *Acta Mater.* , 1999, **47**, 333-343.
- M.D. Kriese, N.R. Moody, W.W. Gerberich, Adhesion assessment of copper films, in "Materials Reliability in Microelectronics VII," eds. J. J. Clement, R. R. Keller, K. S. Krisch, J. E. Sanchez, Jr., Z. Suo, Materials Research Society, Pittsburgh, PA, 1997, vol. 473, pp. 39-50.
- M. D. Kriese, N. R. Moody, W. W. Gerberich, Effects of annealing and interlayers on the adhesion energy of copper thin films to SiO<sub>2</sub>/Si Substrates, *Acta Mater.*, 1998a, **46**, 6623-6630.
- M. Kriese, D. A. Boismer, N. R. Moody, W. W. Gerberich, Nanomechanical fracture-testing of thin films, *Engng Fract. Mech.*, 1998b, **61**, 1-20.
- M. D. Kriese, W. W. Gerberich, N. R. Moody, Indentation of superlayers as a quantitative probe of thin-film interfacial adhesion energy-I. mechanics of interfacial delamination, *Journal of Materials Research*, 1999a, **14**, 3007-3018.
- M. D. Kriese, N. R. Moody, W. W. Gerberich, Quantitative adhesion measures of multilayer films: II. indentation of W/Cu, W/W, Cr/W, *J. Mater. Res.*, 1999b, **14**, 3019-3026.

- W.R. LaFontaine, B. Yost, C.-Y. Li, Effect of residual stress and adhesion on the hardness of copper films deposited on silicon, *J. Mater. Res.*, 1990, **5**, 776-783.
- M. Lane, R. H. Dauskardt, N. Krishna, I. Hashi, Adhesion and reliability of copper interconnects with Ta and TaN barriers, *J. Mater. Res.*, 2000, **15**, 203-211.
- C. Lee, K. Lin, Wetting kinetics and the interfacial interaction behavior between electroless Ni-Cu-P and molten solder, *Jpn. J. Appl. Phys.*, 1994, **33**, 2684-2688.
- K.M. Liechti, Y.S. Chai, Asymmetric shielding in interfacial fracture under in-plane shear, *J. Appl. Mech.*, 1992, **59**, 295-304.
- D.M. Lipkin, G.E. Beltz, A simple elastic cell model of cleavage fracture in the presence of dislocation plasticity, *Acta Mater.*, 1996, **44**, 1287-1292.
- D.M. Lipkin, D.R. Clarke, G.E. Beltz, A strain gradient model of cleavage fracture in plastically deforming materials, *Acta Mater.*, 1996, **44**, 4051-4058.
- D. M. Lipkin, D. R. Clarke, A. G. Evans, Effect of interfacial carbon on adhesion and toughness of gold-sapphire interfaces, *Acta Mater.*, 1998, **46**, 4835-4850.
- J.L. Loubet, J.M. Georges, O. Marchesini, G. Meille, Vickers indentation curves of magnesium oxide (MgO), *J. Tribology*, 1984, **106**, 43-48.
- D. B. Marshall, A. G. Evans, Measurement of adherence of residually stressed thin films by indentation. I. mechanics of interface delamination, *J. Appl. Phys.* 1984, **56**, 2632-2638.
- R. Maboudian, R. T. Howe, Critical review: adhesion in surface micromechanical structures, *J. Vac. Sci. Technol. B*, 1997, **15**, 1-20.
- S. X. Mao, A. G. Evans, The influence of blunting on crack growth at oxide/metal interface, *Acta Mater.*, 1997, **45**, 4263-4270.
- P. Marsh, W. Zielinski, H. Huang, W. W. Gerberich, Crack tip dislocation emission arrangements for equilibrium-III. application to large applied stress intensities, *Acta Metall. Mater.*, 1992, **40**, 2883-2894.
- D. M. Mattox, Thin film metallization of oxides in microelectronics., *Thin Solid Films*, 1973, **18**, 173-186
- J.M. McNaney, R.M. Cannon, R.O. Ritchie, Elastic compliance of four-point bend specimens comprising two linear-elastic materials bonded with a thin layer, *J. of Testing and Evaluation*, 1995, **23**, 95- 101.



- J.M. McNaney, R. Havens, R.O. Ritchie, Elastic compliance of the compact tension specimen comprising two linear-elastic materials bonded with a thin layer. *J. of Testing and Evaluation*, 1997, **25**, 28-35.
- M. Menningen, H. Weiss, Application of fracture mechanics to the adhesion of metal coatings on CFRP, *Surface and Coatings Technology*, 1995, **76-77**, 835-840.
- K. L. Mittal, Adhesion measurements of thin films, *Electrocomponent Science and Technology*, 1976, **3**, 21-42.
- N. R. Moody, R. Q. Hwang, S. Venkataraman, J. E. Angelo, W. W. Gerberich, Adhesion and fracture of tantalum nitride thin films, *Acta Mater.*, 1998, **46** 585-597.
- N. R. Moody, D. P. Adams, A. A. Volinsky, M. D. Kriese, W. W. Gerberich, Annealing effects on interfacial fracture in gold-chromium films in hybrid microcircuits, in "Interfacial Engineering for Optimized Properties II," eds. C. Briant, C. Carter, E. Hall, E., S. Nutt, Materials Research Society, Pittsburgh, PA 2000, vol. 586, 195-205.
- N. R. Moody, N. Yang, D. P. Adams, M. J. Cordill, D. F. Bahr, The effects of copper on the interfacial fracture of gold films, in "Thin Films-Stresses and Mechanical Properties IX," eds. C. S. Ozkan, R. C. Camarata, L. B. Freund, H. Gao, Materials Research Society, Pittsburgh, PA, 2002, vol. 695, L7.5.1-L7.5.6.
- N. R. Moody, D. P. Adams, D. Medlin, A. A. Volinsky, N. Yang, and W. W. Gerberich, Effects of Diffusion on the Interfacial Fracture of Gold-Chromium Microcircuit Films, *Int. J. Fract.*, 2003, to be published.
- A. Munitz, Y. Komem, Structural and resistivity changes in heat-treated chromium-gold films, *Thin Solid Films*, 1976, **37**, 171-179
- A. Munitz and Y. Komem, The increase in the electrical resistance of heat-treated Au/Cr films, *Thin Solid Films*, 1980, **71**, 177-188.
- W. D. Nix, Mechanical properties of thin films, *Metall. Trans. A*, 1989, **20A**, 2217-2245.
- W. D. Nix and H. Gao, Indentation size effects in crystalline materials: a law for strain gradient plasticity, *J. Mech. Phys. Solids*, 1998, **46**, 411-425.
- N. O'Dowd, C. Shih, M. Stout, Test geometries for measuring interfacial fracture toughness, *Int. J. Solids Struct.*, 1992, **29**, 571-589.
- T. S. Oh, J. Rodel, R. M. Cannon, R. O. Ritchie, Ceramic/metal interfacial crack growth: toughening by controlled microcracks and interfacial geometries, *Acta Metall.*, 1988, **36**, 2083-2093.

- M. Ohring, "The Materials Science of Thin Films," Academic Press, New York, 1992. p. 444.
- W. C. Oliver, G. M. Pharr, An improved techniques for determining hardness and elastic modulus using load and displacement sensing indentation experiments, *J. Mater. Res.*, 1992, **7**, 1564-1583.
- V. Paviot, J. Vlassak, W. Nix, Measuring the mechanical properties of thin metal films by means of bulge testing of micromachined windows, in "Thin Films: Stresses and Mechanical Properties V," eds. S. P. Baker, C. A. Ross, P. Townsend, C. A. Volkert, P. Borgesen, Materials Research Society, Pittsburgh, PA, 1995, vol. 356, pp. 579-584.
- G.M. Pharr, Measurement of mechanical properties by ultra-low load indentation, *Mater. Sci. Eng.*, 1998, **A253**, 151-159.
- R.M. Pilliar, J. Nutting, Solid-solid interfacial energy determinations in metal-ceramic systems, *Phil. Mag.*, 1967, **16**, 181-188.
- A. Pocius, "Adhesion and Adhesives Technology. An Introduction." Hanser Publishers, 1997.
- J. R. Rairden, C. A. Neugebauer, and R. A. Sigsbee, Interdiffusion in thin conductor films-chromium/gold, nickel/gold, and chromium silicide/gold, *Metall. Trans.*, 1971, **2**, 719-722.
- I. E. Reimanis, B. J. Dalgleish, M. Brahy, M. Ruhle, A. G. Evans, Effects of plasticity on the crack propagation resistance of a metal/ceramic interface, *Acta Metall. Mater.*, 1990, **38**, 2645-2652.
- I. E. Reimanis, B. J. Dalgleish, A. G. Evans, The fracture resistance of a model metal/ceramic interface, *Acta Metall. Mater.*, 1991, **39**, 3133-3141.
- I. E. Reimanis, The measurement of crack front profiles in the fracture of Au/Al<sub>2</sub>O<sub>3</sub> interfaces, *Acta Mater.*, 1998, **46**, 2479-2484.
- J.R. Rice, Elastic fracture concepts for interfacial cracks, *J. Appl. Mech.*, 1988, **55**, 98-103.
- L. G. Rosenfeld, J. E. Ritter, T. J. Lardner, M. R. Lin, Use of microindentation technique for determining interfacial fracture energy, *J. Appl. Phys.*, 1990, **67**, 3291-3296.
- S.W. Russell, S.A. Rafalski, R.L. Spreitzer, J. Li, M. Moinspour, F. Moghadam, T.L. Alford, Enhanced adhesion of copper to dielectrics via titanium and chromium additions and sacrificial reactions, *Thin Solid Films*, 1995, **262**, 154-167.

- R. Saha and W.D. Nix, Soft films on hard substrates - nanoindentation of tungsten films on sapphire substrates, *Mater. Sci. Eng.*, 2001, **A319-321**, 898-901.
- L.E. Samuels and T.O. Mulhearn, An experimental investigation of the deformed zone associated with indentation hardness impressions, *J. Mech. Phys. Solids*, 1957, **5**, 125-134.
- J. M. Sanchez , S. El-Mansy, B. Sun, T. Scherban, N. Fang, D. Pantuso W. Ford, M. R. Elizalde , J. M. Martinez-Escanola, A. Martin-Meizoso, J. Gil-Sevillano, M. Fuentes, J. Maiz J., Cross-sectional nanoindentation: a new technique for interfacial adhesion characterization, *Acta Mater.* , 1999, **47**, 4405-4413
- J. A. Schneider, S. E. Guthrie, M. D. Kriese, W. M. Clift, N. R. Moody, Effect of carbon on the adhesion of aluminum films to sapphire substrates, in “Fundamentals of Nanoindentation and Nanotribology,” eds. N. R. Moody, W. W. Gerberich, N. Burnham, S. P. Baker, Materials Research Society, Pittsburgh, PA, 1998, vol. 522, pp. 347-352.
- M.K. Small, J. Vlassak, W. Nix, Re-examining the bulge test: methods for improving accuracy and reliability, in “Thin Films: Stresses and Mechanical Properties III,” eds. W. D. Nix, J. C. Bravman, E. Arzt, L. B. Freund, Materials Research Society, Pittsburgh, PA, 1992, vol. 239, pp. 257-262.
- M.K. Small and W.D. Nix, Analysis of the accuracy of the bulge test in determining the mechanical properties of thin films, *J. Mater. Res.*, 1992, **7**, 1553-1563.
- I.N. Sneddon, The relaxation between load and penetration in the axisymmetric Boussinesq problem for a punch of arbitrary profile, *Int. J. Engng. Sci.*, 1965, **3**, 47-57.
- P. A. Steinmann, H. E. Hintermann, A review of the mechanical tests for assessment of thin film adhesion, *J Vac Sci. Tech. A*, 1989, **7**, 2267-2272.
- B. Sun, T. Scherban, D. Pantuso, J. M. Sanchez, R. Elizalde, J. M. Martinez-Esnaola, Cross-sectional nanoindentation: a novel technique to measure thin film adhesion, in “Proceedings of the Tenth International Conference on Fracture,” ICF10, Elsevier Science Ltd., Oxford, UK, 2001, ICF10 0624OR, 1-6.
- R. C. Sun, T. C. Tisone, P. D. Cruzan, The origin of internal stress in low-voltage sputtered tungsten films, *J. Applied Phys.*, 1975, **46**, 112-117
- Z. Suo, J. W. Hutchinson, Sandwich test specimens for measuring interface crack toughness, *Mater. Sci. Engng.*, **A107**, 1989, 135-143.
- Z. Suo and J.W. Hutchinson, Interface crack between two elastic layers, *Int. J. Frac.*, 1990, **43**, 1-18.

- Z. Suo, F. Shih, A. Varias, A theory of cleavage cracking in the presence of plastic flow, *Acta Metall. Mater.*, 1993, **41**, 1551-1557.
- D. Tabor, "Hardness of Metals", Clarendon Press, Oxford, 1951.
- R. E. Thomas, G. A. Haas, Diffusion measurements in thin films utilizing work function changes, *J. Appl. Phys.*, 1972, **43**, 4900-4907.
- M. D. Thouless, J. W. Hutchinson, E. G. Liniger, Plane-strain, buckling driven delamination of thin films: model experiments and mode-II fracture, *Acta Metall. Mater.*, 1992, **40**, 2639-2649.
- B. Tian, T. Schöberl, E. Pink, P. Fratzl, Local mechanical properties of tensile-deformed Al-8.4 at.%Li alloys examined by nanoindentation under an atomic force microscope, *Scripta Mat.*, 2000, **43**, 15-20.
- K. P. Trumble, M. Ruhle, The oxygen activity dependence of spinel interphase formation during Ni/Al<sub>2</sub>O<sub>3</sub> diffusion bonding, in "Metal-Ceramic Interfaces," eds. M. Ruhle, A. G. Evans, M. F. Ashby, J. P. Hirth, Pergamon Press, Oxford, 1990, pp. 144-151.
- M. R. Turner, B. J. Dalgleish, M. Y. He, A. G. Evans, A fracture resistance measurement method for bimaterial interfaces having large debond energy, *Acta Metall. Mater.*, 1995, **43**, 3459-3465.
- M. R. Turner, A. G. Evans, An experimental study of the mechanisms of crack extension along an oxide/metal interface, *Acta Mater.*, 1996, **44**, 863-871.
- V. Tvergaard, J. W. Hutchinson, The relation between crack growth resistance and fracture process parameters in elastic-plastic solids, *J. Mech. Phys. Solids*, 1992, **40**, 1377-1397.
- N.I. Tymiak, A.A. Volinsky, M.D. Kriese, S.A. Downs, W.W. Gerberich, The role of plasticity in bimaterial fracture with ductile interlayers, *Met Mater Trans A*, 2000, **31A**, 863-872.
- S. K. Venkataraman, D. L. Kohstedt, W. W. Gerberich, Microscratch analysis of the work of adhesion for Pt thin films on NiO, *J. Mater. Res.*, 1992, **7**, 1126-1132.
- S. K. Venkataraman, J. C. Nelson, A. J. Hsieh, D. L. Kohstedt, W. W. Gerberich, Continuous microscratch measurements of thin film adhesion strengths, *J. Adhes. Sci. Technol.*, 1993a, **7**, 1279-1292.
- S. K. Venkataraman, D. L. Kohstedt, W. W. Gerberich, Continuous microindentation of passivating surfaces, *J. Mater. Res.*, 1993b, **8**, 685-688.

- S. K. Venkataraman, D. L. Kohlstedt, W. W. Gerberich, Metal-ceramic interfacial fracture resistance using the continuous microscratch technique, *Thin Solid Films*, 1993c, **223**, 269-275.
- S. K. Venkataraman, J. C. Nelson, N. R. Moody, D. L. Kohlstedt, W. W. Gerberich, Micromechanical characterization of tantalum nitride thin films, in "Polycrystalline Thin Films: Structure, Texture, Properties, and Applications," eds. K. Barmak, M. A. Parker, J. A. Floro, R. Sinclair, and D. A. Smith, Materials Research Society, Pittsburgh, PA, 1994, vol. 343, pp. 597-602.
- S. Venkataraman, D.L. Kohlstedt, W.W. Gerberich, Continuous microscratch measurements of the practical and true works of adhesion for metallic systems, *J. Mater. Res.*, 1996, **11**, 3133-3145.
- R.P. Vinci, E.M. Zielinski, J.C. Bravman, Thermal strain and stress in copper thin films, *Thin Solid Films*, 1995, **262**, 142-153.
- J. Vlassak, W. Nix, A new bulge test technique for determining Young's modulus and Poisson's ratio of thin films, *J. Mater. Res.*, 1992, **7**, 3242-3249.
- J.J. Vlassak, M.D. Drory, W.D. Nix, A simple technique for measuring the adhesion of brittle films to ductile substrates with application to diamond-coated titanium, *J. Mater. Res.*, 1997, **12**, 1900-1910.
- A. A. Volinsky, N. I. Tymiak, M. D. Kriese, W. W. Gerberich, J. W. Hutchinson, Quantitative modeling and measurement of copper thin film adhesion, in "Fracture and Ductile vs Brittle Behavior-Theory, Modeling, and Experiment," eds. G. E. Beltz, R. L. Blumberg Selinger, M. P. Marder, K-S. Kim, Materials Research Society, Pittsburgh, PA, 1999, vol. 539, pp. 277-290.
- A. A. Volinsky, "The Role of Geometry and Plasticity in Thin, Ductile Film Adhesion," Ph.D. Thesis, University of Minnesota, 2000.
- A. A. Volinsky, W. M. Clift, N. R. Moody, W. W. Gerberich, Indentation induced debonding of ductile films, in "Interfacial Engineering for Optimized Properties II," (eds.) C. B. Carter, E. L. Hall, C. L. Briant, S. Nutt, Materials Research Society, Pittsburgh, PA, 2000, vol. 586.
- A. A. Volinsky, N. R. Moody, W. W. Gerberich, Interfacial toughness measurements for thin films on substrates. *Acta Mater.*, 2002, **50**, 441-466.
- A. A. Volinsky, et al. Fracture toughness, adhesion, and mechanical properties of low-k dielectric thin films measured by nanoindentation, *Thin Solid Films*, 2002b, accepted for publication.
- K.-T. Wan, Y.-W. Mai, Fracture mechanics of a new blister test with stable crack growth, *Acta Metall. Mater.*, 1995, **43**, 4109-4115.

- J.S. Wang, Z. Suo, Experimental determination of interfacial toughness using Brazil-nut-sandwich, *Acta Metall. Mater.*, 1990, **38**, 1279-1290.
- Y. Wei, J. W. Hutchinson, Nonlinear delamination mechanics for thin films, *J. Mech. Phys. Solids*, 1997, **45**, 1137-1159.
- Y. Wei, J. W. Hutchinson, Interface strength, work of adhesion and plasticity in the peel test, *Int'l. J. Fract.*, 1999, **93**, 315-333.
- T.P. Weihs, S. Hong, J.C. Bravman, W.D. Nix, Mechanical deflection of cantilever microbeams: a new technique for testing the mechanical properties of thin films. *J Mater. Res.*, 1988 **3**, 931-942.
- W.L. Winterbottom, Equilibrium shape of a small particle in contact with a foreign substrate, *Acta Metall.*, 1967, **15**, 303-310
- C.L. Woodcock, D.F. Bahr, Plastic zone evolution around small scale indentations, *Scripta Mater.*, 2000, **43**, 783-788.
- C.L. Woodcock, M.S. Thesis, Washington State University, 2002.
- C.L. Woodcock, D.F. Bahr, N.R. Moody, Plastic zone development around nanoindentations, in "Fundamentals of Nanoindentation and Nanotribology II", eds. S. P. Baker, R. F. Cook, S. G. Corcoran, N. R. Moody, 2001, **649**, pp. Q7.14.1-Q7.14.6.
- T. W. Wu, C. Hwang, J. Lo, P. S. Alexopoulos, Microhardness and microstructure of ion-beam-sputtered, nitrogen-doped NiFe films, *Thin Solid Films*, 1988, **166**, 299-308.
- T. W. Wu, Microscratch and load relaxation tests for ultra-thin films, *J. Mater. Res.*, 1991, **6**, 407-425.
- G. Xu , M-Y. He, D. R. Clarke, The effect of moisture on the fracture energy of TiN/SiO<sub>2</sub> interfaces in multilayer films, *Acta Mater.*, 1999, **47**, 4131-4141.
- X. A. Zhao, E. Kolawa, M.-A. Nicolet, Reaction of thin metalfilms with crystalline and amorphous Al<sub>2</sub>O<sub>3</sub>, *J. Vac. Sci. Technol. A.*, 1986, **4**, 3139-3141.
- W. Zielinski, M. J. Lii, W. W. Gerberich, Crack tip dislocation emission arrangements for equilibrium-I. In situ TEM observations of Fe-2wt%Si, *Acta Metall. Mater.*, 1992, **40**, 2861-2872.

## TABLES

**Table 1** Mechanical properties and measured fracture energies of thin film systems.  
(Source: A.A. Volinsky et al., 2002)

System	$\sigma_{ys}$ (MPa)	E (GPa)	h (nm)	Work of Adhesion $G_0$ (J/m <sup>2</sup> ) $W_d^{theor}$		T (°C)	$\gamma_c^b$ (J/m <sup>2</sup> )
Ta <sup>a</sup> /Al/C/Al <sub>2</sub> O <sub>3</sub>	298	70	500	0.33	–	20	1.05
W <sup>a</sup> /Al–	298-203	70	500–3200	0.25	–	20	0.2–0.65
Cu/C/SiO <sub>2</sub> /Si							
W <sup>a</sup> /Al–	700-203	70	40–3200	0.41	–	20	0.3–27
Cu/Cu/SiO <sub>2</sub> /Si							
Ta <sub>2</sub> N <sup>a</sup> /Al/Al <sub>2</sub> O <sub>3</sub>	190	70	178	–	–	20	7.0
SiO <sub>2</sub> /TiN/Al–	430-196	70	150–400	5.0	–	20	4.9–13
Cu/SiO <sub>2</sub> /Si							
SiO <sub>2</sub> /Al/TiN/Ti/SiO <sub>2</sub>	70	250	–	–	–	20	1.9
Ta <sup>a</sup> /Al–Cu/Al <sub>2</sub> O <sub>3</sub>	298	70	500	–	–	20	5.6
W <sub>a</sub> /Al–Cu/SiO <sub>2</sub> /Si	329-252	70	340–1000	4.3	–	20	7.7–8.2
Au/C/Al <sub>2</sub> O <sub>3</sub>	338	80.8	15,000	0.317	0.3	20	1.7
Au/Al <sub>2</sub> O <sub>3</sub>	338	80.8	15,000	1.27	0.6,0.5	20	80,230
TaN <sup>a</sup> /Au/Al <sub>2</sub> O <sub>3</sub>	517	80.8	200	0.63	0.6,0.5	20	1.4
TaN <sup>a</sup> /Au/Cr/Al <sub>2</sub> O <sub>3</sub>	517	80.8	200	1.35	–	20	2.9
W <sup>a</sup> /Cu/SiO <sub>2</sub> /Si	974-466	120	40–3000	0.90	0.8	20	0.6–100
W <sup>a</sup> /Cu/Ti/SiO <sub>2</sub> /Si	974-466	120	40–3000	3.63	2.2 <sup>c</sup>	20	4–110
SiO <sub>2</sub> /Cu/TaN/Ta/SiO <sub>2</sub> /Si	1060-435	120	30–10,500	5.0	1.8 <sup>c</sup>	20	4.5–80
W/Cu/Cr/SiO <sub>2</sub> /Si	630-509	120	440–1100	5.3	–	20	7–15
W <sup>a</sup> /Cu/SiO <sub>2</sub> /Si	806-540	120	80	0.90	0.8	20–130	1–4.1
W <sup>a</sup> /Cu/SiO <sub>2</sub> /Si	560-300	120	500	0.90	0.8	20–130	14–215
Cr <sup>a</sup> /Cu/SiO <sub>2</sub>	913-528	120	50–800	0.5	0.8	20	0.5–1.0
Nb/Al <sub>2</sub> O <sub>3</sub>	2000 <sup>d</sup>	103	105	0.95	0.8	–	0.95
Nb/Ag/Al <sub>2</sub> O <sub>3</sub>	2000 <sup>d</sup>	103	105	0.78	0.5	–	0.78
W/SiO <sub>2</sub> /Si	1220-1088	360	530–760	1.73	–	20	5.5–9.0
Ta <sub>2</sub> N/Al <sub>2</sub> O <sub>3</sub>	–	–	100–600	0.5	–	20	0.5–0.5
Si <sub>x</sub> N <sub>y</sub> /SiO <sub>2</sub> /Si	–	171	1000	–	–	20	1.5
NbN/304SS	–	468	2800	–	–	–	400

<sup>a</sup> Used as a superlayer on top of the film of interest.

<sup>b</sup> Range refers to the variation with either thickness or temperature.

<sup>c</sup> Actually TiW and TiN as opposed to Ti and TaN used at the interface as a thin adhesive layer.

<sup>d</sup> Yield estimated from nanohardness of 6 GPa by  $H/3$ .

**Table 2** Fracture energy of the interface of 0.5  $\mu\text{m}$   $\text{Ta}_2\text{N}$  on sapphire with different thickness Al interlayers (Al – sapphire interface failure)

System	$\Gamma_{\text{I}}$ Single Buckling ( $\text{J/m}^2$ )	$\Gamma_{\text{I}}$ Double Buckling ( $\text{J/m}^2$ )	$\Gamma_{\text{I}}$ Scratch Initiated Buckle ( $\text{J/m}^2$ )
500 nm $\text{Ta}_2\text{N}$ / 28 nm Al/ $\text{Al}_2\text{O}_3$	8.1	$7.8 \pm 0.14$	8.9
500 nm $\text{Ta}_2\text{N}$ / 154 nm Al/ $\text{Al}_2\text{O}_3$	8.0	$7.5 \pm 0.24$	8

**Table 3** Fracture energy results for as-deposited gold, gold-chromium, and annealed gold-chromium films.

Film	$\Gamma(\square)$ ( $\text{J/m}^2$ )	$\Gamma$	$\Gamma_{\square}$ ( $\text{J/m}^2$ )	Fracture Path
Superlayer				
Au-AD	1.3	-75	0.5	Au- $\text{Al}_2\text{O}_3$
Au-Cr-AD	2.9	-82	0.9	AuCr- $\text{Al}_2\text{O}_3$
Nanoindentation				
Au-Cr-AD	2.6	-63	1.3	AuCr- $\text{Al}_2\text{O}_3$
400°C/2h	2.2	-60	1.2	AuCr- $\text{Al}_2\text{O}_3$
400°C/8h	13.2	-71	5.5	$\text{Ta}_2\text{N}$ - $\text{Al}_2\text{O}_3$ , Au, AuCr- $\text{Al}_2\text{O}_3$
Nanoscratch				
400°C/8h	3.1	-71	1.3	AuCr- $\text{Al}_2\text{O}_3$



## Nomenclature

a	interfacial crack length, delamination radius
A	fracture surface area, indenter contact area, proportionality constant, initial film stress term
b	Burgers vector, blister half-width, line width, contact radius, disk thickness
B	unit width, specimen thickness, proportionality constant
c	dislocation free zone
C	plastic zone size, compliance
C or cr	denotes critical d grain size, diameter of residual Brinell indentation
D	diffusion coefficient, diameter of Brinell indenter, Dampening coefficient
E	Young's modulus
E'	plane strain Young's modulus ( $E/(1-\nu^2)$ )
f	denotes the film
fric	denotes frictional
G	strain energy release rate
h	thin film thickness
H	thin film hardness, half the specimen height
I or ind	denotes indentation
$I_T$	transformed moment of inertia
J	flux
k	Hall-Petch constant, curvature
K	stress intensity at a crack tip ( $K_{I,II,III}$ are used for mode I, II and III)
$K_C$	critical stress intensity of a material
m	mass
M	bending moment
P	load
r	contact radius, bulge radius
R	denotes residual, resistance to crack propagation
s	denotes the substrate
S	stiffness
t	time
T	temperature
$u_0$	max film deflection
U	energy
$V_I$	indentation volume
W	half-width of wedge indentation
$W_A$	thermodynamic work of adhesion
$W_{A,P}$	practical work of adhesion
Y	dimensionless geometric factor
$\square$	buckling constant, Dundurs parameter
$\square$	angle between wedge or cone face and sample surface, Dundurs parameter
$\square$	displacement, buckle or bulge height

$\epsilon$	strain, positive taken as compressive
$\delta$	phase angle between force and displacement signals
$\gamma$	surface energy
$\gamma_i$	interface fracture toughness
$G$	shear modulus, buckling constant
$\nu$	Poisson's ratio
$\theta$	equilibrium contact angle, compression angle
$\sigma_{ys}$	thin film yield strength
$\sigma$	stress ( $\sigma_{I,B,R}$ are indentation, buckling and residual stresses, respectively)
$\tau$	shear stress
$\omega$	frequency of oscillation
$V_a$	activation volume
$\phi$	mode mixity (phase) angle

## List of Figures

Figure 1. Contact angle measurement schematic (Volinsky et al., 2002).

Figure 2. Interfacial fracture toughness as a function of the mode mixity angle (Volinsky et al., 2002).

Figure 3. Phenomenological functions for  $\chi(\chi)$  (Volinsky et al., 2002).

Figure 4. Sandwich specimen tests schematics: (a) modified  $K_{Ic}$  sample; (b) Brazil-nut sample; (c) four-point bend (UCSB) sample (Volinsky et al., 2002).

Figure 5. Schematic of the bulge test (Volinsky et al., 2002).

Figure 6. Schematic of the superlayer tests (Volinsky et al., 2002).

Figure 7. Film decohesion in the superlayer test (Volinsky et al., 2002).

Figure 8. Typical locations where  $\chi(\chi)$  and  $\chi_{ss}$  are measured on telephone cord blisters.

Figure 9 (a) No buckling during indentation; (b) double-buckling during indentation; (c) single-buckling after indenter tip removal (Volinsky et al., 2002).

Figure 10. Optical micrographs of indentation induced blisters with (right) and without (left) a tungsten overlayer (Volinsky et al., 2002).

Figure 11. Schematic of the precracked line scratch test (PLST) (Volinsky et al., 2002).

Figure 12. Strain energy release rate for the precracked line scratch test (PLST) (Volinsky et al., 2002).

Figure 13. Schematic of unstable crack growth during buckling for PLST (Volinsky et al., 2002).

Figure 14. Indentation schematic before, during, and after test illustrating the different depths involved. Note that  $h_{\text{plastic}}$  corresponds to the contact depth referred to above. (Adapted from Oliver and Pharr, 1992)

Figure 15. Graphical representation of a load displacement record using the continuous stiffness technique.

Figure 16. A simplified dynamic model of a nanoindentation system with continuous stiffness capability. (Adapted from Oliver and Pharr, 1992)

Figure 17. Hardness extracted for Au and Au-Cu films on sapphire substrates using the continuous stiffness method (Woodcock, 2002).

Figure 18. Contact AFM image of a 20 mN conical indent. 20 by 20  $\mu\text{m}$  image (Woodcock, 2002).

Figure 19. Hardness as a function of contact depth demonstrating an indentation size effect using a Berkovich indenter tip (Woodcock, 2002).

Figure 20. Hardness vs. contact depth data for both tip geometries. While both tips show an ISE, the sharper tips appear to harden at low loads (Woodcock and Bahr, 2000).

Figure 21. Yield strength extracted from plastic zone size measurements for both cube corner and Berkovich tip geometries. The bulk values extrapolate to bracket the value given by the model of Nix and Gao. (Woodcock and Bahr, 2000).

Figure 22 (a) Indentation fracture of as-deposited film occurred consistently at loads between 250 and 300 mN producing (b) large circular spalls. In all fracture tests, the center point was constrained giving rise to a reverse or double buckle configuration (Moody et al., 1998).

Figure 23. Scratch test fractures in the as-deposited film (a) occurred consistently near 100 mN and were characterized by an abrupt increase in tangential load. (b) The fractures propagated along the film-substrate interfaces producing well-defined spalls ahead of the indenter (Moody et al., 1998).

Figure 24. Two scratches triggered uniform width buckles that propagated back along much of the scratch track length (Moody et al., 1998).

Figure 25. Different types of indentation induced failures in 500 nm thick  $\text{Ta}_2\text{N}$  on sapphire with a 154 nm Al interlayer. Curve A shows delamination and spalling during loading, curve B shows delamination and spalling during unloading, and curve C shows evidence of a stable delamination on unloading (Bahr and Gerberich, 1998).

Figure 26. Optical micrograph of delaminations and spalling events from indentations shown in Figure 25. Note that indent C has only delaminated, and the crack has arrested without spalling (Bahr and Gerberich, 1998).

Figure 27. Acoustic emission signal from curves A, B, and C shown in Figure 25. Signals A and B achieved higher voltages than the range set on the oscilloscope, therefore only a limited voltage range from these was recorded. Signals are offset for clarity (Bahr and Gerberich, 1998).

Figure 28. AFM image and section analysis of edge of spalled region. The fracture path was along the aluminum - sapphire interface. The crack proceeded to kink into the aluminum, travel along the aluminum -  $\text{Ta}_2\text{N}$  interface for 1  $\mu\text{m}$ , and then kink through the nitride film (Bahr and Gerberich, 1998).

Figure 29. Schematic of the cross-sectional indentation test showing (a) indenter orientation and (b) interface fracture (Sun et al., 2001).

Figure 30. Indentation-induced delaminations imaged with optical interference contrast. (A) Sample II-A W/W sample with no radial cracking; (B) sample II-B W/W multilayer with minor radial cracking; and (C) sample II-C Cr/W multilayer with pronounced radial cracking (Kriese et al., 1999a).

Figure 31. Indentation induced copper and tungsten-copper delamination. Tests correspond to 100 mN (top rows), 250 mN (middle rows) and 400 mN (bottom rows). Photos are collages; original indents were 100 to 300 mm apart. Nomarski optical contrast was used to make delamination identifiable. (a) pure Cu. The ring delamination at 400 mN may be double-buckling. (b) W/Cu bilayers (Kriese et al., 1998b).

Figure 32. Characteristic indentation data of Cu and W/Cu. Each sample was loaded to 100, 250, and 400 mN. The copper only film (a) has deviations in loading behavior representing delamination and deformation constraint. The companion copper/tungsten bilayer (b) has abrupt transitions and greater penetration depths (Kriese et al., 1998b).

Figure 33. Indentation fracture measurements on thin copper thin films shows that film thickness and annealing increase measured fracture energies (Kriese et al., 1998b).

Figure 34. Effect of interlayers on indentation behavior of  $\sim 1100$  nm Cu films with  $\sim 650$  nm W superlayers (Kriese et al., 1998a).

Figure 35. Measured adhesion energies of copper thin films (Kriese et al., 1998a).

Figure 36. Film thickness effects on fracture of copper on oxidized silicon substrates with and without a titanium interlayer (Tymiak et al., 2000; Gerberich et al., 2000; Volinsky, 1999).

Figure 37. Test temperature effects on the fracture energies of 80 nm and 500 nm thick copper films on oxidized silicon substrates (Volinsky et al., 2002).

Figure 38. Telephone cord blisters in triggered by sputter deposition of tungsten overlayers in (a) 10 nm and (b) 200 nm thick gold films on sapphire substrates (Moody et al., 2003).

Figure 39. One dimensional,  $\Gamma(\square)$ , and steady state,  $\Gamma_{ss}$ , fracture energies from gold on sapphire showing the independence of fracture energy on film thickness for very thin gold films. The corresponding mode I values are equal to the true works of adhesion for gold on sapphire.

Figure 40. Superposition of fracture energies of gold on sapphire from a number of studies using different test techniques shows the strong effect film thickness has on performance of these films.

Figure 41. (a) Mode I fracture energies for as-deposited and annealed gold on chromium samples as a function of blister diameter. (b) An expanded view of the data shows that as-

deposited and partially annealed film fracture energies are similar. The fracture energies increased when going from as-deposited to annealed samples with very high values and significant scatter observed for samples where annealing depleted the chromium adhesive layer (Moody et al., 2003).

Figure 42. Fracture energies plotted as a function of normalized blister diameter indicates that the large increase in fracture energy at the small blister sizes results from crack tip plastic zone interactions with the plastic zone created by the indenter (Moody et al., 2003).

Figure 43. Deposition of a tungsten overlayer (a) triggered extensive blistering in the Au-Cu film while (b) additional stresses from nanoindentation were required to trigger delamination and buckling (Moody et al., 2002).

## Figures

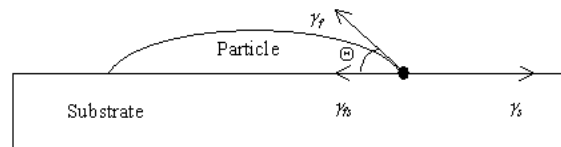


Figure 1. Contact angle measurement schematic (Volinsky et al., 2002).

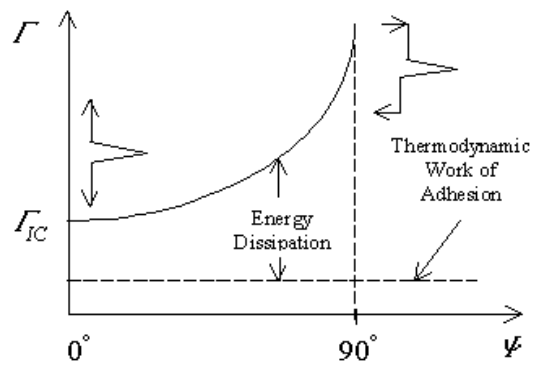


Figure 2. Interfacial fracture toughness as a function of the mode mixity angle (Volinsky et al., 2002).

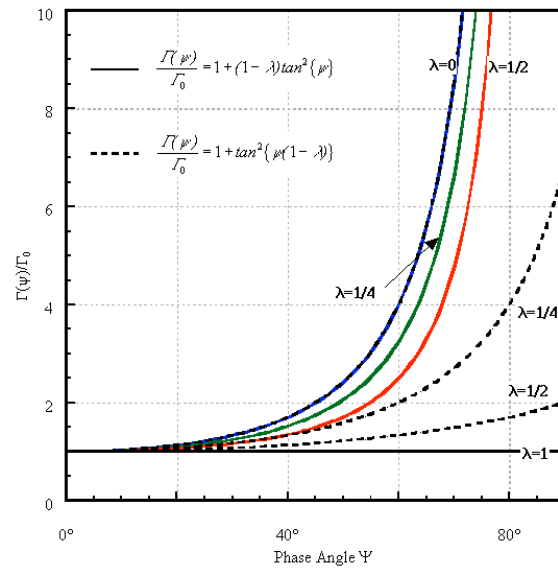


Figure 3. Phenomenological functions for  $\Gamma(\psi)$  (Volinsky et al., 2002).

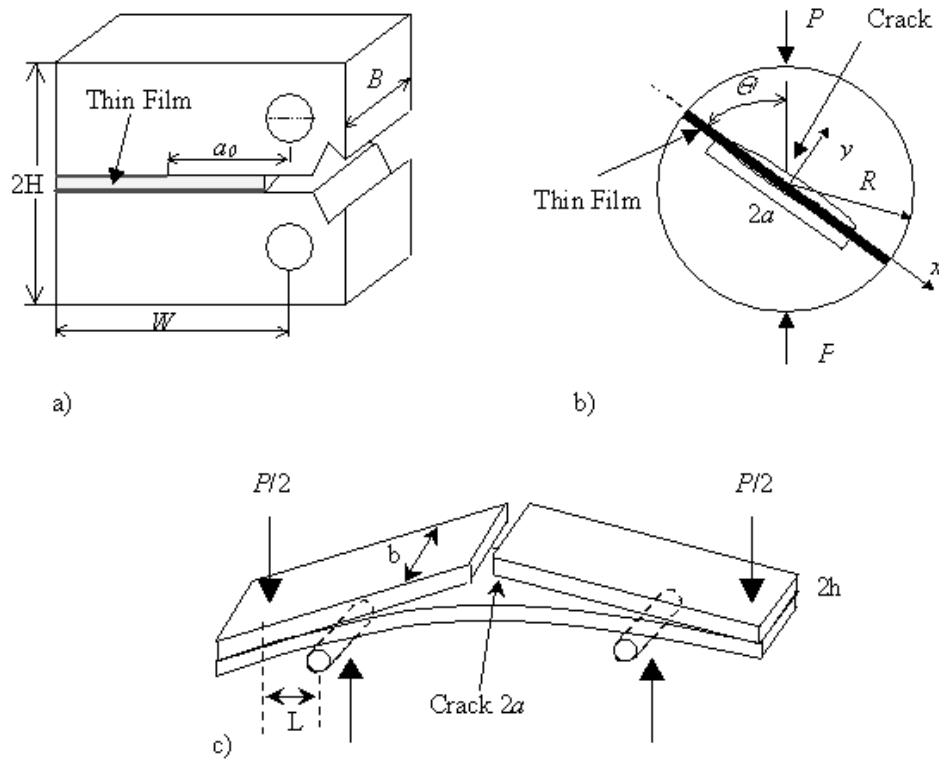


Figure 4. Sandwich specimen tests schematics: (a) modified  $K_{Ic}$  sample; (b) Brazil-nut sample; (c) four-point bend (UCSB) sample (Volinsky et al., 2002).



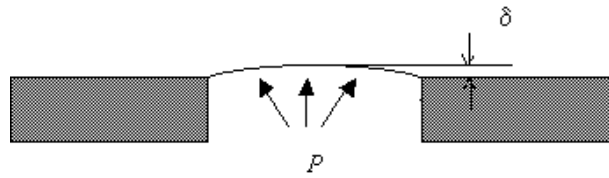


Figure 5. Schematic of the bulge test (Volinsky et al., 2002).

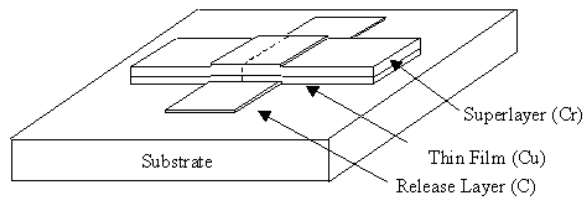


Figure 6. Schematic of the superlayer tests (Volinsky et al., 2002).

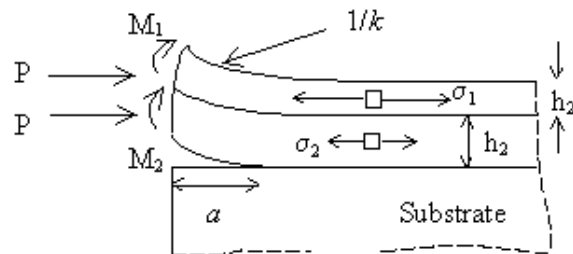


Figure 7. Film decohesion in the superlayer test (Volinsky et al., 2002).

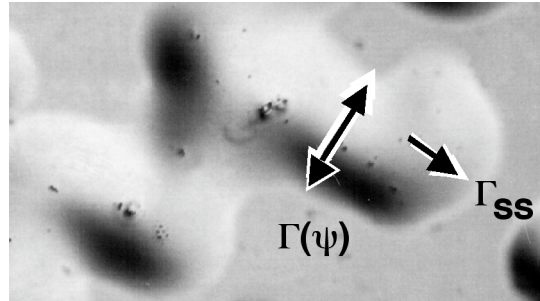


Figure 8. Typical locations where  $\Gamma(\psi)$  and  $\Gamma_{ss}$  are measured on telephone cord blisters.

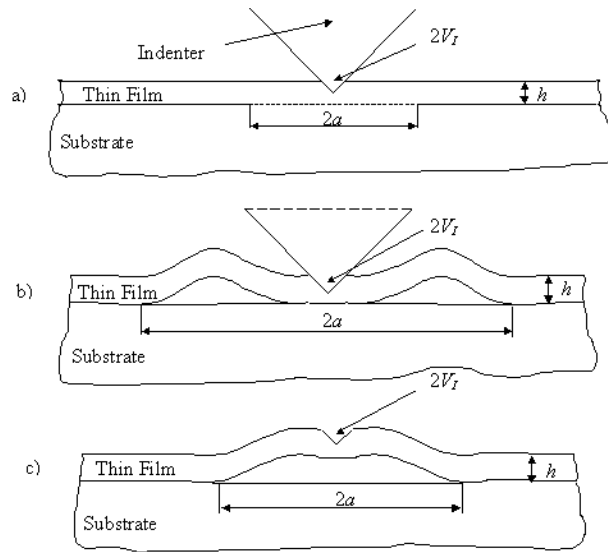


Figure 9 (a) No buckling during indentation; (b) double-buckling during indentation; (c) single-buckling after indenter tip removal (Volinsky et al., 2002).

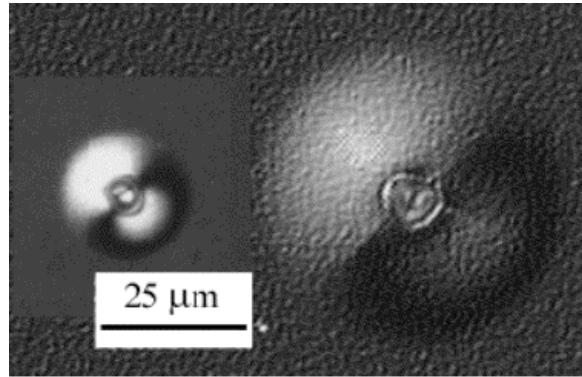


Figure 10. Optical micrographs of indentation induced blisters with (right) and without (left) a tungsten overlayer (Volinsky et al., 2002).

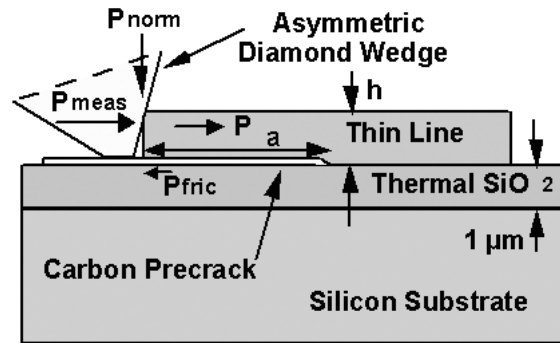


Figure 11. Schematic of the precracked line scratch test (PSLT) (Volinsky et al., 2002).

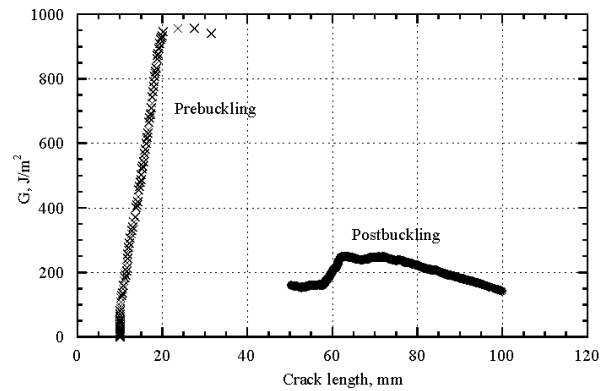


Figure 12. Strain energy release rate for the precracked line scratch test (PLST) (Volinsky et al., 2002).

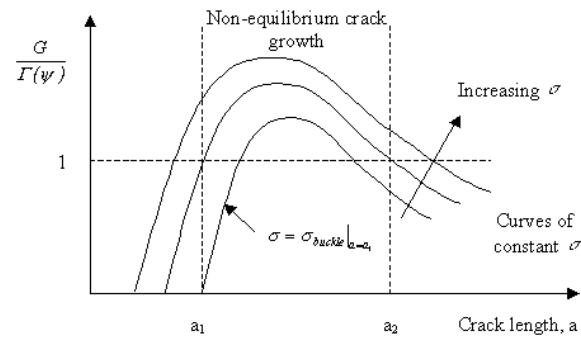


Figure 13. Schematic of unstable crack growth during buckling for PLST (Volinsky et al., 2002).

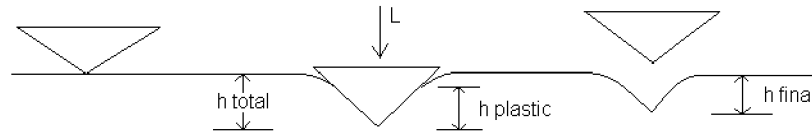


Figure 14. Indentation schematic before, during, and after test illustrating the different depths involved. Note that  $h_{\text{plastic}}$  corresponds to the contact depth referred to above. (Adapted from Oliver and Pharr, 1992)

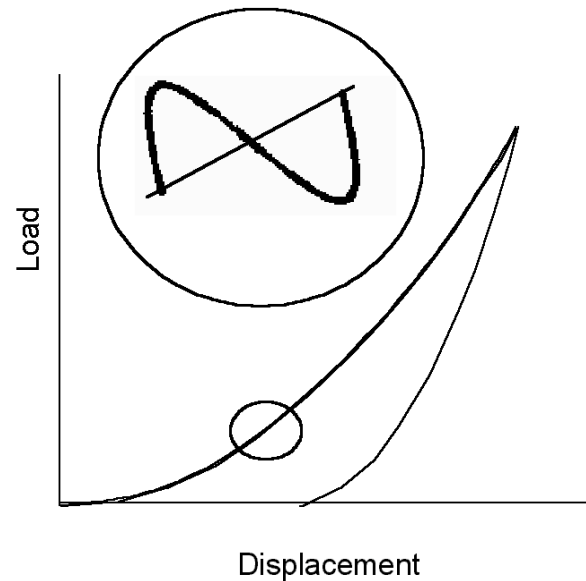


Figure 15. Graphical representation of a load displacement record using the continuous stiffness technique.

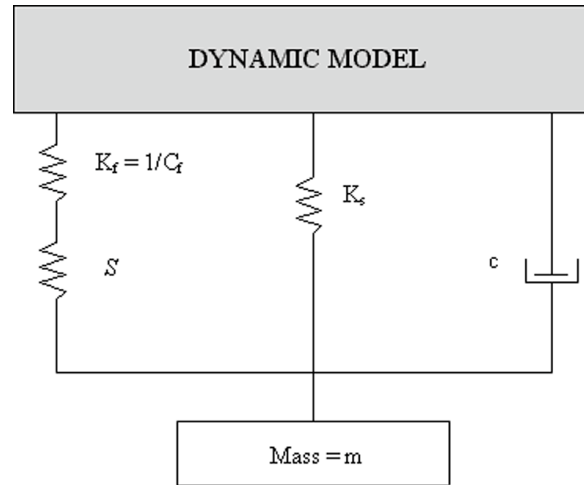


Figure 16. A simplified dynamic model of a nanoindentation system with continuous stiffness capability. (Adapted from Oliver and Pharr, 1992)

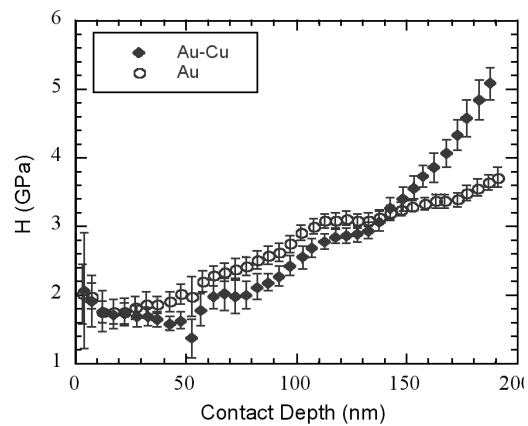


Figure 17. Hardness extracted for Au and Au-Cu films on sapphire substrates using the continuous stiffness method (Woodcock, 2002).

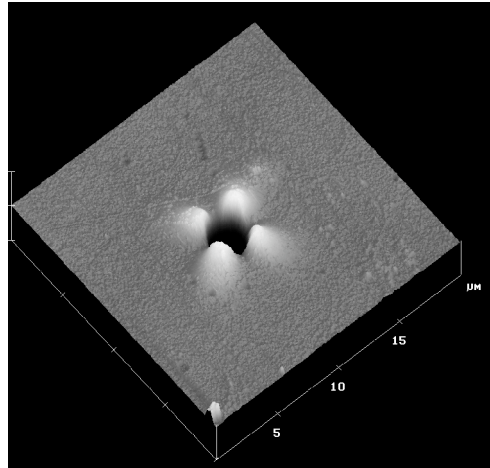


Figure 18. Contact AFM image of a 20 mN conical indent. 20 by 20  $\mu\text{m}$  image (Woodcock, 2002).

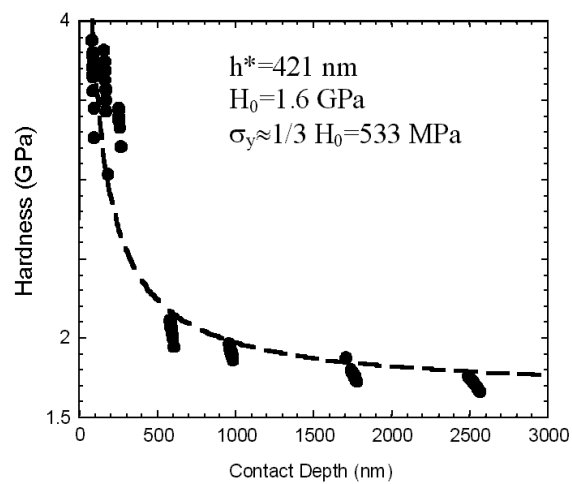


Figure 19. Hardness as a function of contact depth demonstrating an indentation size effect using a Berkovich indenter tip (Woodcock, 2002).

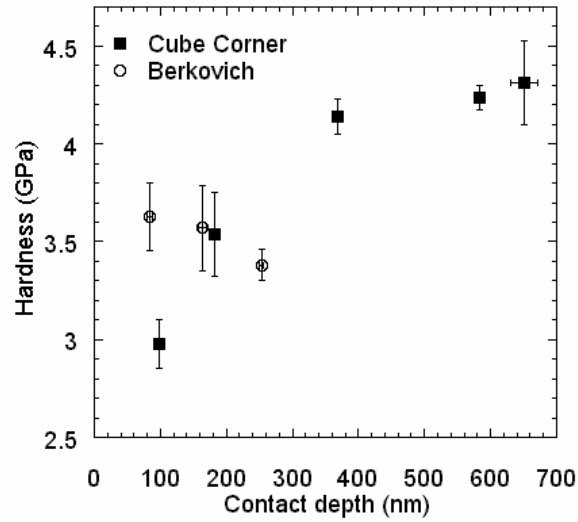


Figure 20. Hardness vs. contact depth data for both tip geometries. While both tips show an ISE, the sharper tips appear to harden at low loads (Woodcock and Bahr, 2000).

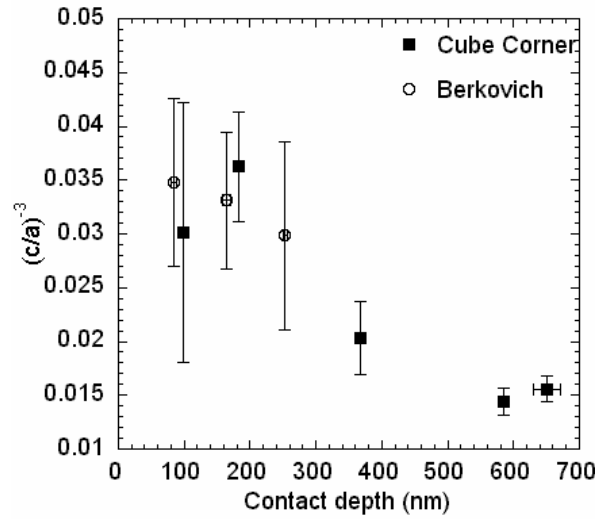
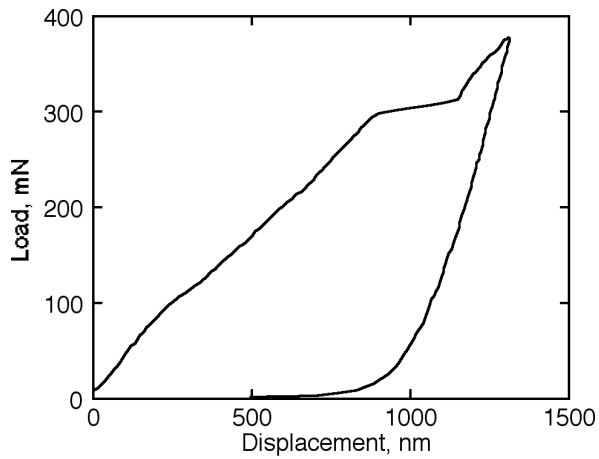
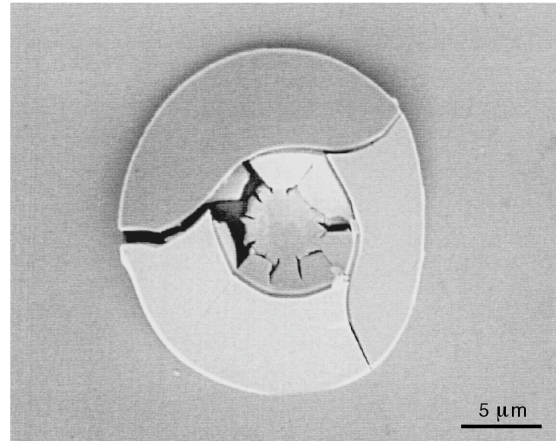


Figure 21. Yield strength extracted from plastic zone size measurements for both cube corner and Berkovich tip geometries. The bulk values extrapolate to bracket the value given by the model of Nix and Gao. (Woodcock and Bahr, 2000).

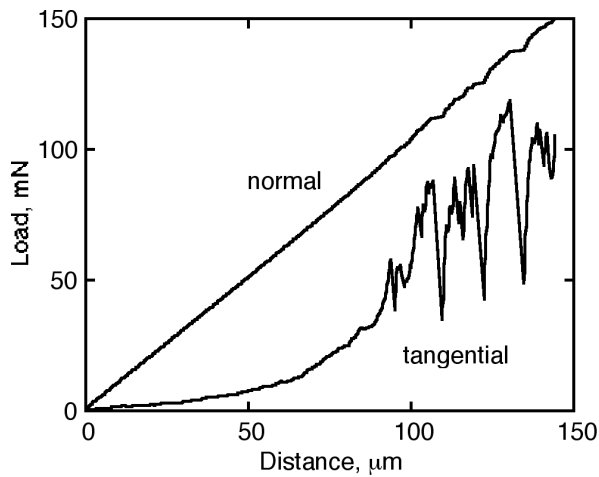


(a)

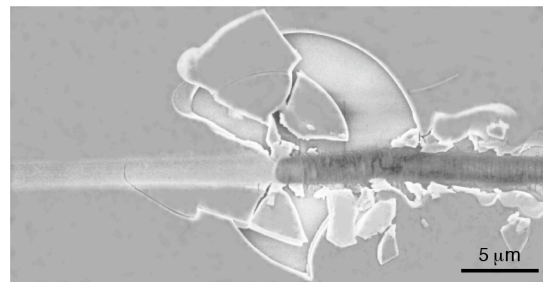
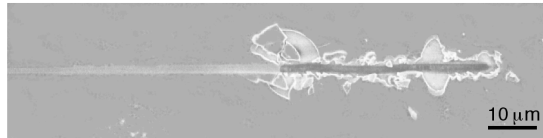


(b)

Figure 22 (a) Indentation fracture of as-deposited film occurred consistently at loads between 250 and 300 mN producing (b) large circular spalls. In all fracture tests, the center point was constrained giving rise to a reverse or double buckle configuration (Moody et al., 1998).



(a)



(b)

Figure 23. Scratch test fractures in the as-deposited film (a) occurred consistently near 100 mN and were characterized by an abrupt increase in tangential load. (b) The fractures propagated along the film-substrate interfaces producing well-defined spalls ahead of the indenter (Moody et al., 1998).



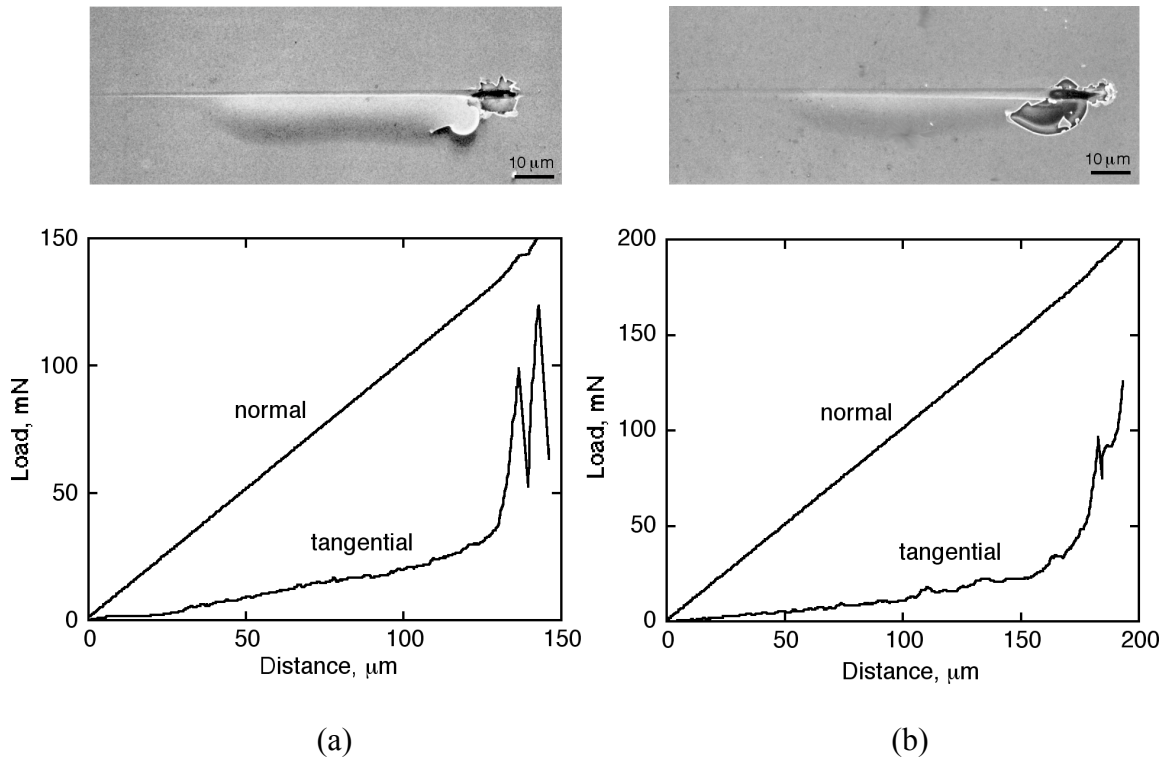


Figure 24. Two scratches triggered uniform width buckles that propagated back along much of the scratch track length (Moody et al., 1998)

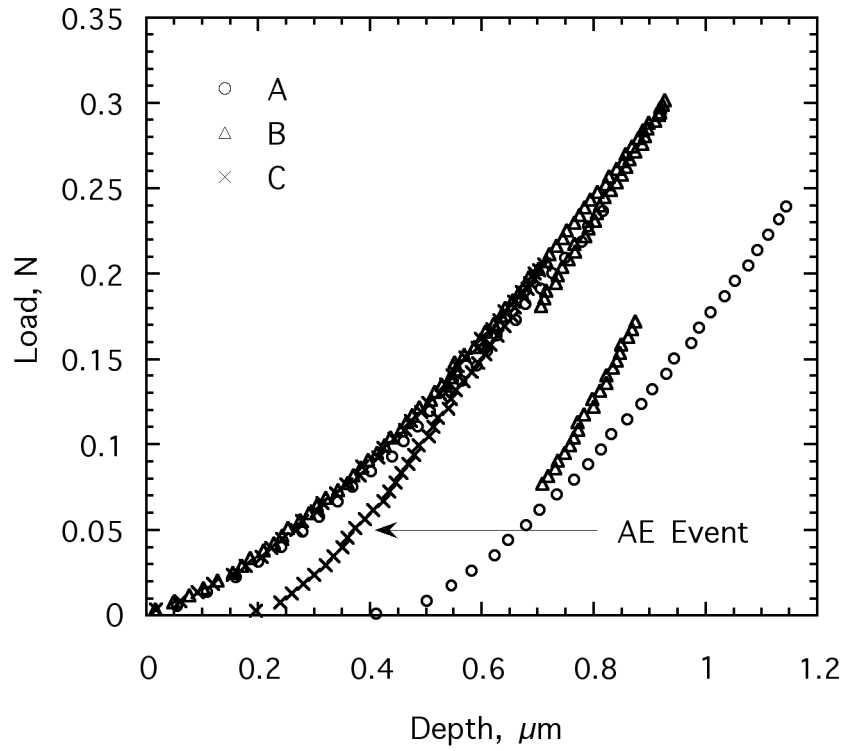


Figure 25. Different types of indentation induced failures in 500 nm thick  $\text{Ta}_2\text{N}$  on sapphire with a 154 nm Al interlayer. Curve A shows delamination and spalling during loading, curve B shows delamination and spalling during unloading, and curve C shows evidence of a stable delamination on unloading (Bahr and Gerberich, 1998).

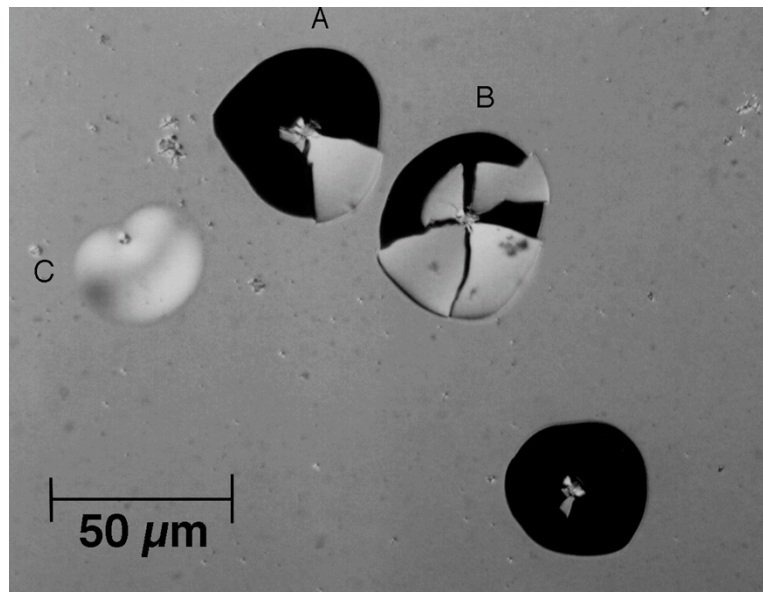


Figure 26. Optical micrograph of delaminations and spalling events from indentations shown in Figure 25. Note that indent C has only delaminated, and the crack has arrested without spalling (Bahr and Gerberich, 1998).

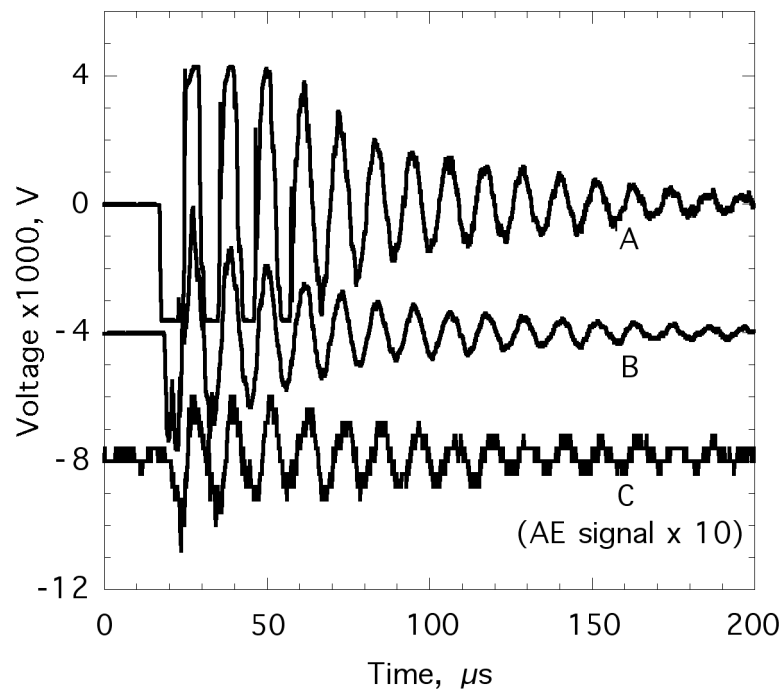


Figure 27. Acoustic emission signal from curves A, B, and C shown in Figure 25. Signals A and B achieved higher voltages than the range set on the oscilloscope, therefore only a limited voltage range from these was recorded. Signals are offset for clarity (Bahr and Gerberich, 1998).

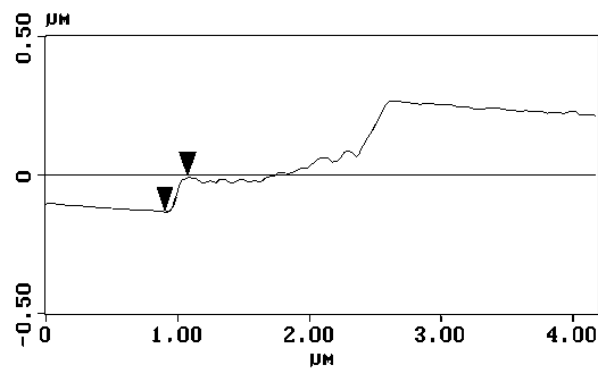
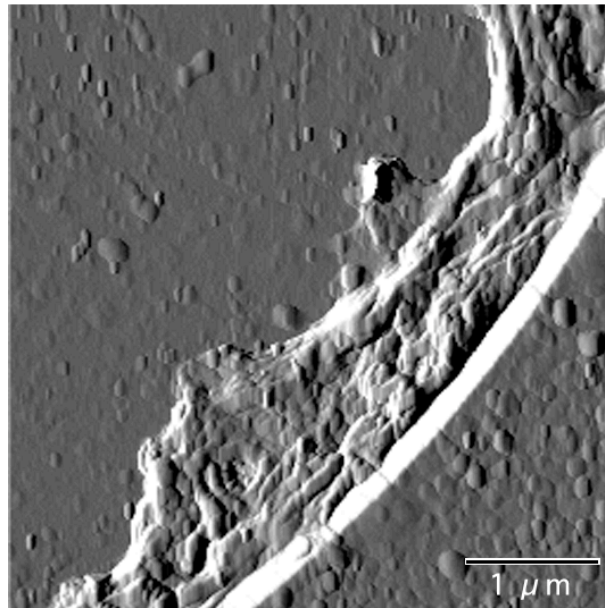
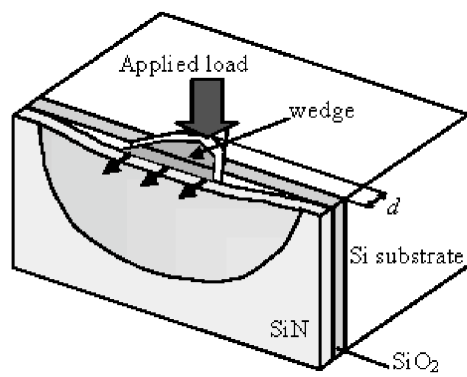
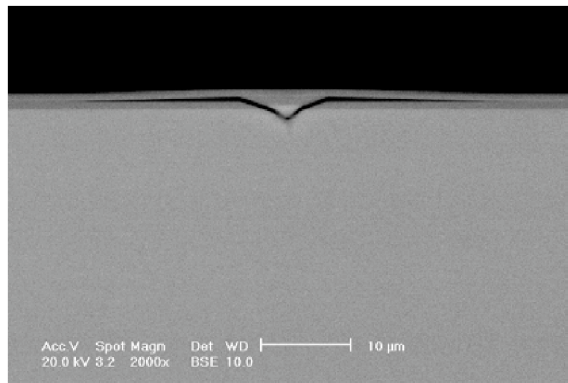


Figure 28. AFM image and section analysis of edge of spalled region. The fracture path was along the aluminum - sapphire interface. The crack proceeded to kink into the aluminum, travel along the aluminum - Ta<sub>2</sub>N interface for 1 μm, and then kink through the nitride film (Bahr and Gerberich, 1998).



(a)



(b)

Figure 29. Schematic of the cross-sectional indentation test showing (a) indenter orientation and (b) interface fracture (Sun et al., 2001).

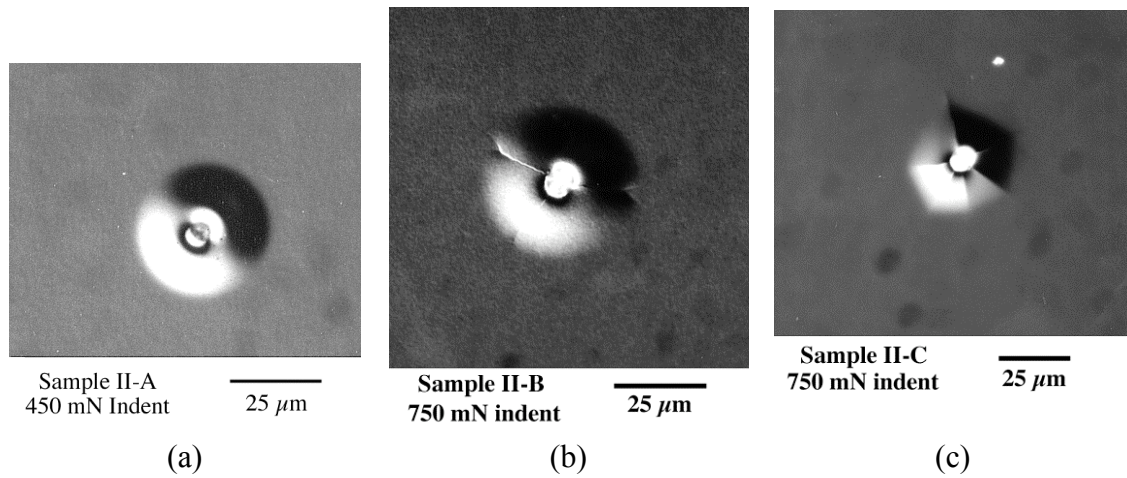


Figure 30. Indentation-induced delaminations imaged with optical interference contrast. (A) Sample II-A W/W sample with no radial cracking; (B) sample II-B W/W multilayer with minor radial cracking; and (C) sample II-C Cr/W multilayer with pronounced radial cracking (Kriese et al., 1999a).

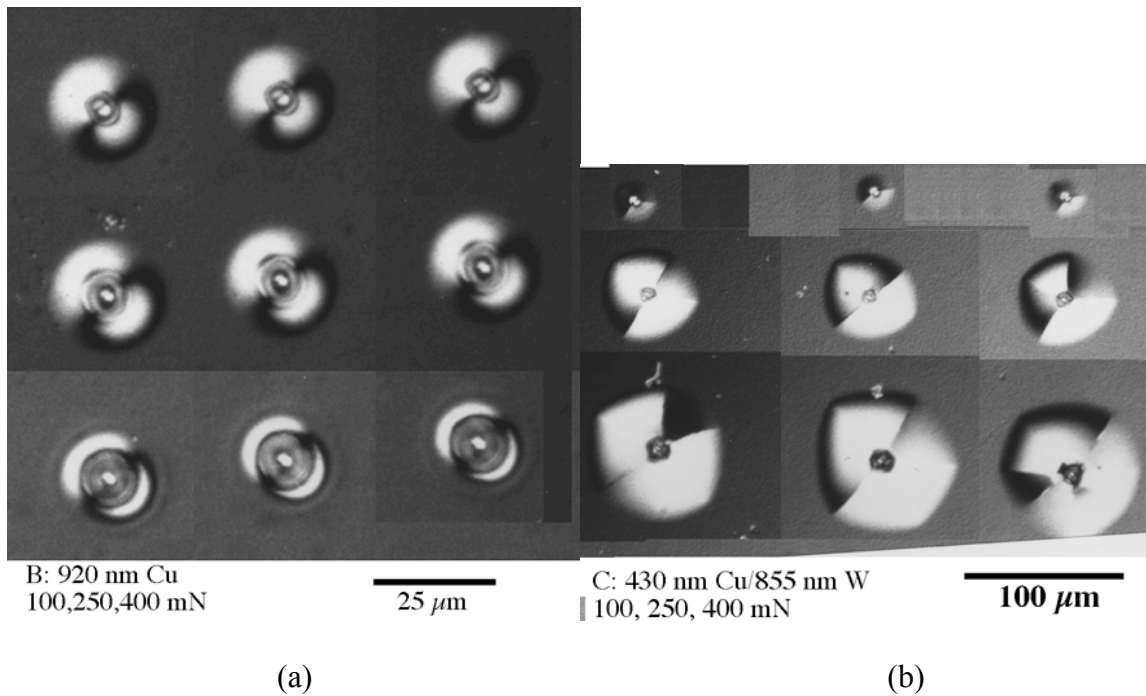


Figure 31. Indentation induced copper and tungsten-copper delamination. Tests correspond to 100 mN (top rows), 250 mN (middle rows) and 400 mN (bottom rows). Photos are collages; original indents were 100 to 300 mm apart. Nomarski optical contrast was used to make delamination identifiable. (a) pure Cu. The ring delamination at 400 mN may be double-buckling. (b) W/Cu bilayers (Kriese et al., 1998b).

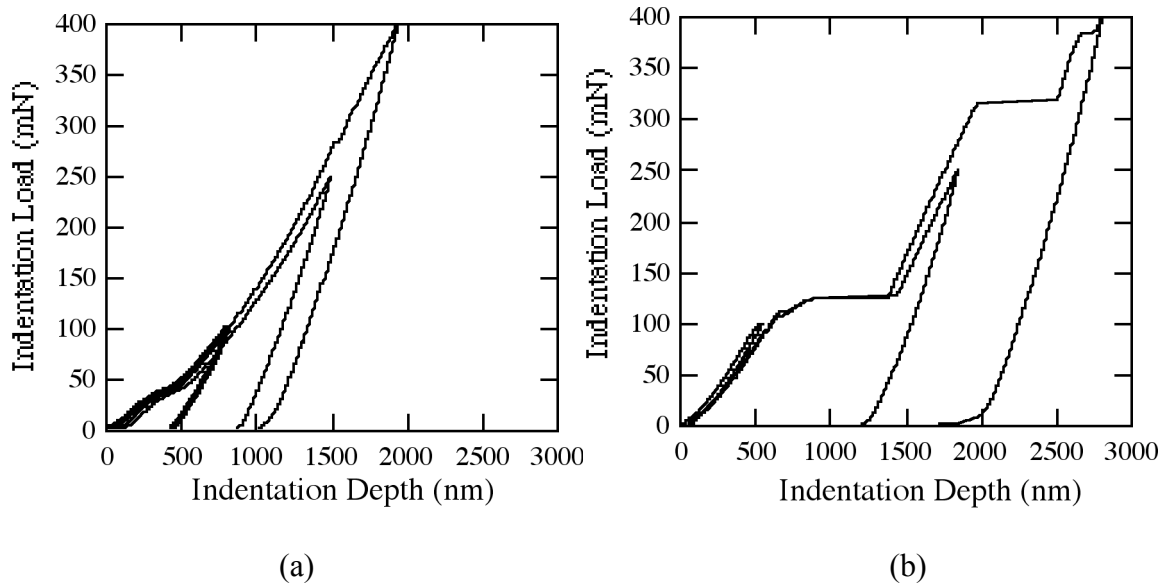


Figure 32. Characteristic indentation data of Cu and W/Cu. Each sample was loaded to 100, 250, and 400 mN. The copper only film (a) has deviations in loading behavior representing delamination and deformation constraint. The companion copper/tungsten bilayer (b) has abrupt transitions and greater penetration depths (Kriese et al., 1998b).

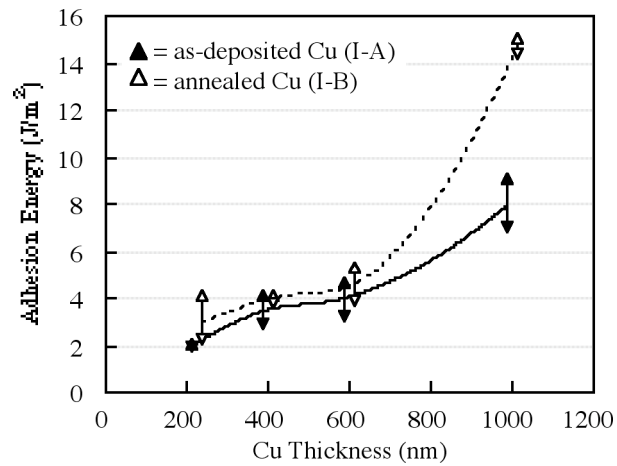


Figure 33. Indentation fracture measurements on thin copper thin films shows that film thickness and annealing increase measured fracture energies (Kriese et al., 1998b).

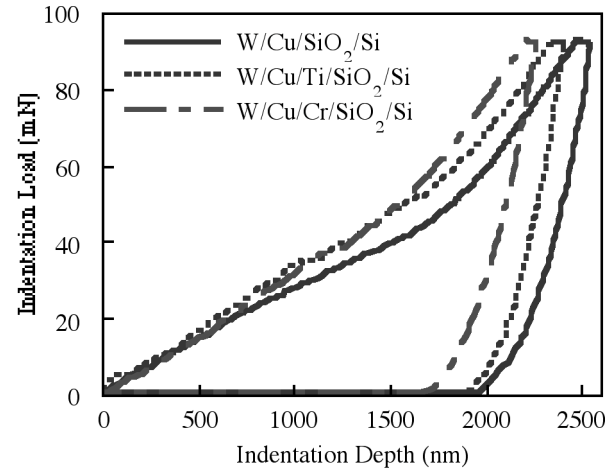


Figure 34. Effect of interlayers on indentation behavior of  $\sim 1100$  nm Cu films with  $\sim 650$  nm W superlayers (Kriese et al., 1998a).

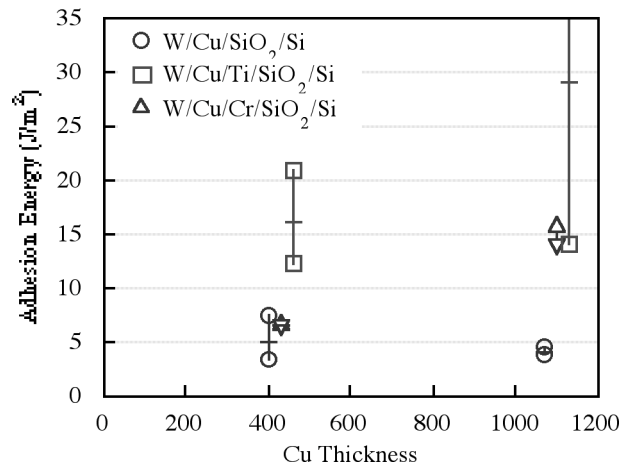


Figure 35. Measured adhesion energies of copper thin films (Kriese et al., 1998a).



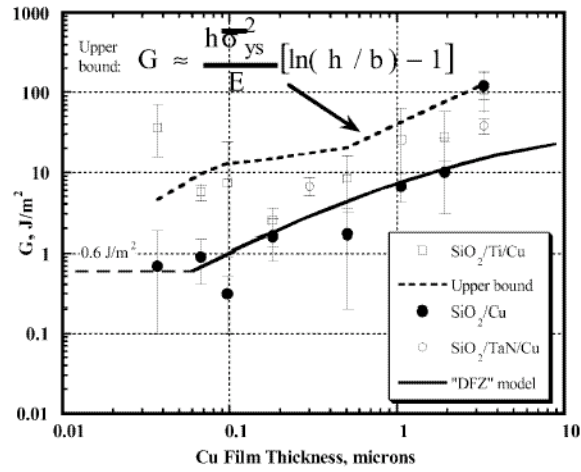


Figure 36. Film thickness effects on fracture of copper on oxidized silicon substrates with and without a titanium interlayer (Tymiak et al., 2000; Gerberich et al., 2000; Volinsky, 1999).

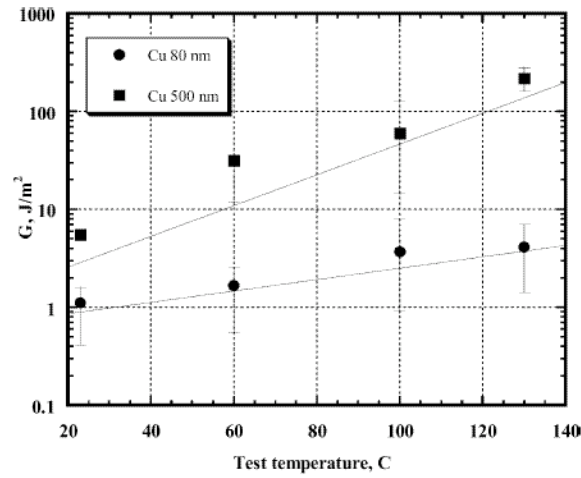
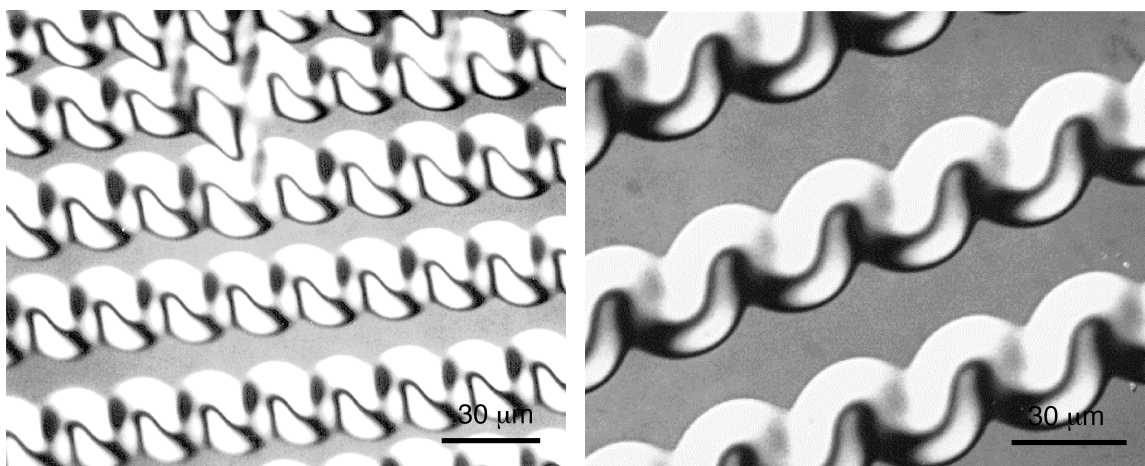


Figure 37. Test temperature effects on the fracture energies of 80 nm and 500 nm thick copper films on oxidized silicon substrates (Volinsky et al., 2002).



(a)

(b)

Figure 38. Telephone cord blisters in triggered by sputter deposition of tungsten overlayers in (a) 10 nm and (b) 200 nm thick gold films on sapphire substrates (Moody et al., 2003).

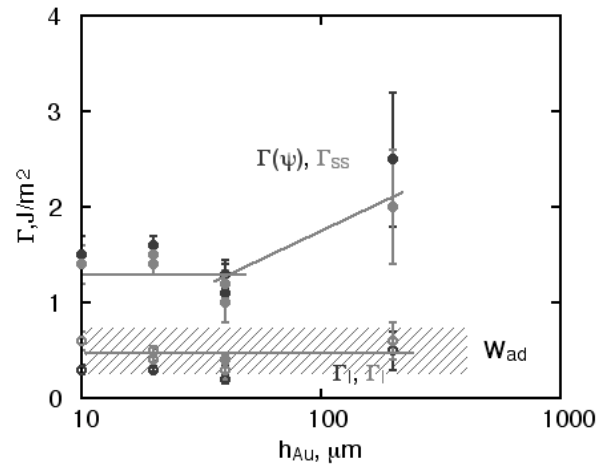


Figure 39. One dimensional,  $\Gamma(\psi)$ , and steady state,  $\Gamma_{ss}$ , fracture energies from gold on sapphire showing the independence of fracture energy on film thickness for very thin gold films. The corresponding mode I values are equal to the true works of adhesion for gold on sapphire.

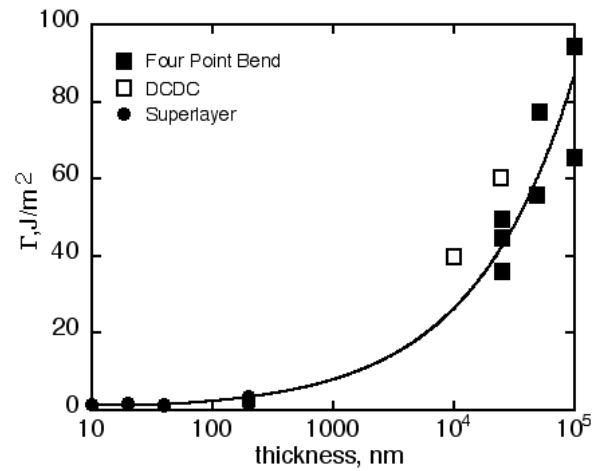


Figure 40. Superposition of fracture energies of gold on sapphire from a number of studies using different test techniques shows the strong effect film thickness has on performance of these films.

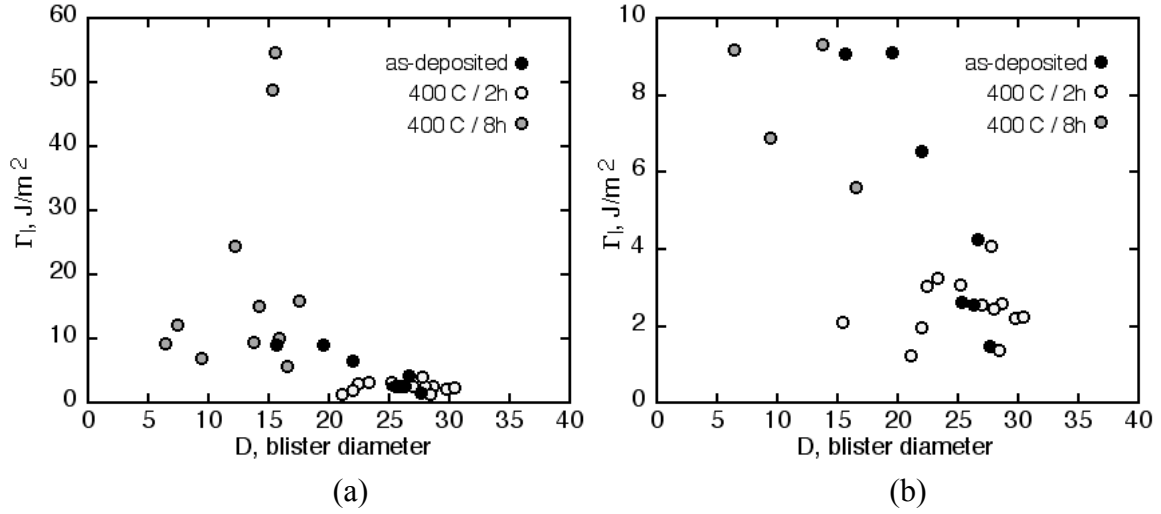


Figure 41. (a) Mode I fracture energies for as-deposited and annealed gold on chromium samples as a function of blister diameter. (b) An expanded view of the data shows that as-deposited and partially annealed film fracture energies are similar. The fracture energies increased when going from as-deposited to annealed samples with very high values and significant scatter observed for samples where annealing depleted the chromium adhesive layer (Moody et al., 2003).

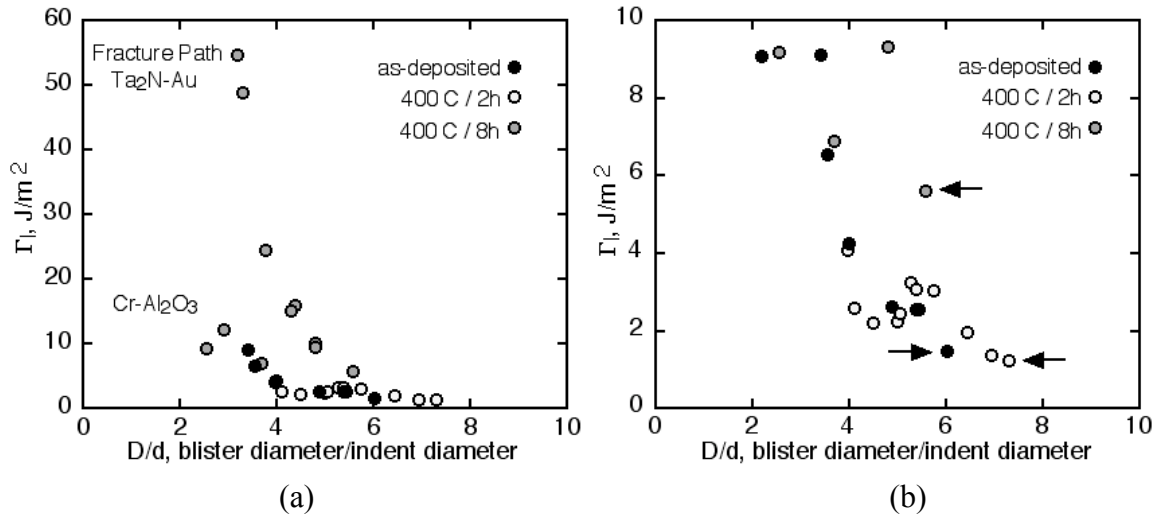


Figure 42. Fracture energies plotted as a function of normalized blister diameter indicates that the large increase in fracture energy at the small blister sizes results from crack tip plastic zone interactions with the plastic zone created by the indenter (Moody et al., 2003).

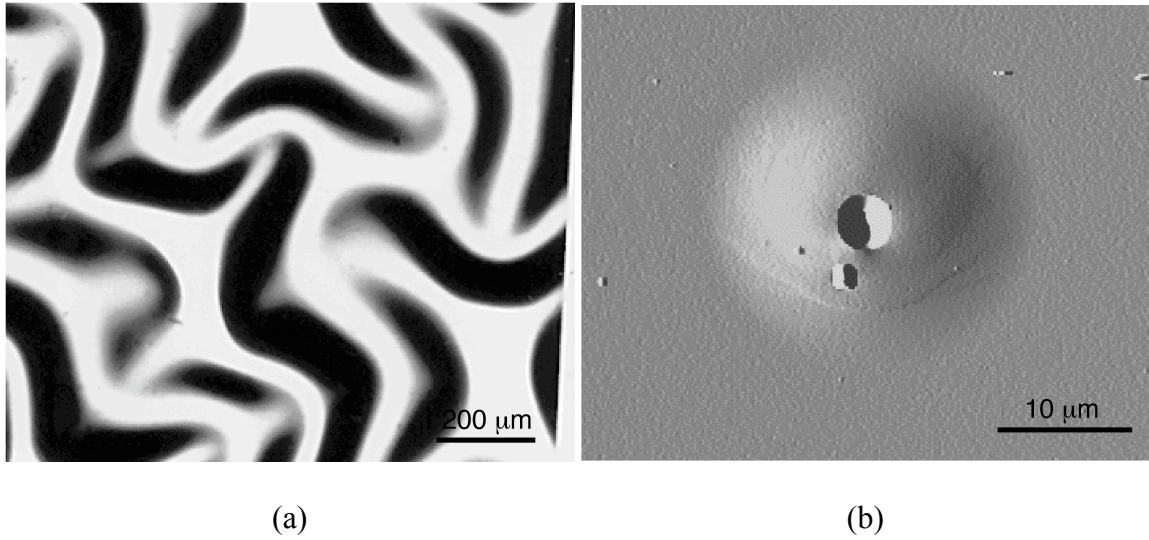


Figure 43. Deposition of a tungsten overlayer (a) triggered extensive blistering in the Au-Cu film while (b) additional stresses from nanoindentation were required to trigger delamination and buckling (Moody et al., 2002).